

NOTE TO USERS

This reproduction is the best copy available.

UMI[®]

**THREE-DIMENSIONAL MODELING OF THE ROTATION
EFFECT ON THE GROWTH OF $\text{Ge}_{1-x}\text{Si}_x$ BY THE
TRAVELING SOLVENT METHOD**

by

Theodore Jason Makriyannis, B.Eng.
Ryerson University, 2004

A thesis

presented to Ryerson University

in partial fulfillment of the requirements for the degree of

Master of Applied Science

in the program of

JAN - 3 2005

Mechanical Engineering

**PROPERTY OF
Ryerson University Library**

Toronto, Ontario, Canada, 2004

Theodore J. Makriyannis 2004 ©

UMI Number: EC52965

INFORMATION TO USERS

The quality of this reproduction is dependent upon the quality of the copy submitted. Broken or indistinct print, colored or poor quality illustrations and photographs, print bleed-through, substandard margins, and improper alignment can adversely affect reproduction.

In the unlikely event that the author did not send a complete manuscript and there are missing pages, these will be noted. Also, if unauthorized copyright material had to be removed, a note will indicate the deletion.

UMI[®]

UMI Microform EC52965

Copyright 2009 by ProQuest LLC.

All rights reserved. This microform edition is protected against unauthorized copying under Title 17, United States Code.

ProQuest LLC
789 E. Eisenhower Parkway
PO Box 1346
Ann Arbor, MI 48106-1346

BORROWER'S PAGE

Ryerson University requires the signatures of all persons using or photocopying this thesis. Please sign below and give the address and date.

This image shows a single sheet of white paper with horizontal blue or grey ruling lines. The lines are evenly spaced and run across the width of the page. There is no handwriting or other markings on the paper.

PROPERTY OF
Ryerson University Library

ABSTRACT

Three-Dimensional Modeling of the Rotation Effect on the Growth of $\text{Ge}_{1-x}\text{Si}_x$ by the Traveling Solvent Method

Master of Applied Science 2004, Theodore J. Makriyannis

School of Graduate Studies, Ryerson University

The traveling solvent method known as TSM is a process used to produce pure and homogeneous crystals. The TSM process has been tested on many alloys producing uniform and uncontaminated crystal products. A three-dimensional numerical simulation for the growth of $\text{Ge}_{1-x}\text{Si}_x$ by the traveling solvent method under axial rotation has been modeled. In this model a mesh sensitivity analysis has been carried out to find an optimum mesh which provides accurate results while saving computational time. The full Navier-Stokes equations together with the energy, mass transport and continuity equations were solved numerically using the finite element technique. The application of crucible rotation to the traveling solvent method is an attempt to control the buoyancy induced convection throughout the melt and to suppress the three-dimensional characteristics of unsteady heat flow. The application of different rotational speeds on the solvent has also been investigated. These different speeds of rotation were shown to have a considerable effect on the buoyancy induced flow. The solute distribution throughout the melt was also affected substantially. Taking these two factors into account plays a crucial role in the crystal growth process. The speed of rotation was found to have a significant effect on the intensity of the convective flow in the melt and an optimal rotational speed was encountered.

ACKNOWLEDGEMENTS

It has been a privilege and an honor to work with Dr. Ziad Saghir of Ryerson University and the author would like to thank Dr. Ziad Saghir for his helpful assistance and guidance throughout the completion of this thesis. The author would also like to express his sincere appreciation to both his parents Apostolis and Maria Makriyannis for their complete support and enthusiasm in the completion of this thesis. The author also acknowledges the support of Dr. Daniel Labrie of Dalhousie University and the assistance and useful suggestions of his colleagues Leily Abidi, Omar Gaber and Rita Kozak.

PROPERTY OF
Ryerson University Library

TABLE OF CONTENTS

	PAGE
Author's Declaration	ii
Borrower's Page	iii
Abstract	iv
Acknowledgements	v
Table of Contents	vi
List of Figures	viii
List of Tables	x
Nomenclature	xi
 CHAPTER 1 - Introduction.....	 1
 Chapter 2 – Theory and Setup	 9
2.0 Traveling solvent method	9
2.1 Model Description	9
2.2 Governing Equations	13
2.2.1 Navier-Stokes Equations	13
2.2.2 Energy Transfer Equation	14
2.2.3 Mass Transport Equation	14
2.2.4 Continuity Equation	15
2.3 Dimensional Analysis	15
2.4 Dimensionless Governing Equations	15
2.4.1 Navier-Stokes Equations	16
2.4.2 Energy transfer Equation	16
2.4.3 Mass Transport Equation	16
2.4.4 Continuity Equation	16
2.5 Model Boundary Conditions and Heater Profile.....	17
2.5.1 Model Dimensions.....	17
2.5.2 Model Boundary Conditions	17
2.5.3 Heater Profile.....	20
2.6 Mesh Sensitivity Analysis.....	23
 CHAPTER 3 – Uniform Heating Results and Discussion	 25
3.0 Introduction.....	25
3.1 Terrestrial Condition.....	26
3.2 Microgravity Condition	41

CHAPTER 4 – Non-Uniform Heating Results and Discussion.....	51
4.0 Introduction	51
4.1 Terrestrial Condition	53
4.2 Microgravity Condition.....	68
 CHAPTER 5 - Conclusion.....	 77
APPENDIX A.....	81
APPENDIX B.....	83
APPENDIX C.....	88
APPENDIX D.....	89
APPENDIX E.....	92
REFERENCES	93

PROPERTY OF
Ryerson University Library

LIST OF FIGURES

FIGURE	DESCRIPTION	PAGE
2.1	TSM Process	11
2.2	Model Description	12
2.3	Ge-Si Phase Diagram	19
2.4	Geometrical Model and Heater Profile	21
2.5	TSM Furnace	22
2.6	Mesh Sensitivity	24
UNIFORM HEATING		
3.1	3-D Profile	25
3.2	Axial Velocity at 0 rpm Terrestrial Condition	29
3.3	Axial Velocity at 2 rpm Terrestrial Condition	30
3.4	Axial Velocity at 5 rpm Terrestrial Condition	31
3.5	Axial Velocity at 7 rpm Terrestrial Condition	32
3.6	Maximum Speed Graph Terrestrial Condition	33
3.7	Silicon Distribution at 0 rpm Terrestrial Condition	36
3.8	Silicon Distribution at 2 rpm Terrestrial Condition	37
3.9	Silicon Distribution at 5 rpm Terrestrial Condition	38
3.10	Silicon Distribution at 7 rpm Terrestrial Condition	39
3.11	Silicon Distribution at 0.03 cm above Growth Interface	40
3.12	Axial Velocity at 0 rpm Microgravity Condition	43
3.13	Axial Velocity at 2 rpm Microgravity Condition	44
3.14	Axial Velocity at 5 rpm Microgravity Condition	45
3.15	Maximum Speed Graph Microgravity Condition	47
3.16	Silicon Distribution at 0 rpm Microgravity Condition	47
3.17	Silicon Distribution at 2 rpm Microgravity Condition	48
3.18	Silicon Distribution at 5 rpm Microgravity Condition	48
3.19	Silicon Distribution at 0.03 cm above Growth Interface	49

NON-UNIFORM HEATING

4.1	Temperature Profile Variation around Model	51
4.2	3-D Profile	52
4.3	Axial Velocity at 0 rpm Terrestrial Condition	56
4.4	Axial Velocity at 2 rpm Terrestrial Condition	57
4.5	Axial Velocity at 5 rpm Terrestrial Condition	58
4.6	Axial Velocity at 7 rpm Terrestrial Condition	59
4.7	Maximum Speed Graph Terrestrial Condition	60
4.8	Silicon Distribution at 0 rpm Terrestrial Condition	63
4.9	Silicon Distribution at 2 rpm Terrestrial Condition	64
4.10	Silicon Distribution at 5 rpm Terrestrial Condition	65
4.11	Silicon Distribution at 7 rpm Terrestrial Condition	66
4.12	Silicon Distribution at 0.03 cm above Growth Interface	67
4.13	Axial Velocity at 0 rpm Microgravity Condition	70
4.14	Axial Velocity at 2 rpm Microgravity Condition	71
4.15	Axial Velocity at 5 rpm Microgravity Condition	72
4.16	Maximum Speed Graph Microgravity Condition	73
4.17	Silicon Distribution at 0 rpm Microgravity Condition	74
4.18	Silicon Distribution at 2 rpm Microgravity Condition	74
4.19	Silicon Distribution at 5 rpm Microgravity Condition	75
4.20	Silicon Distribution at 0.03 cm above Growth Interface	75

PROPERTY OF
Ryerson University Library

LIST OF TABLES

TABLE	DESCRIPTION	PAGE
1	Mesh Sensitivity	24
A.1	Source Material Properties $\text{Ge}_{0.85}\text{Si}_{0.15}$	81
A.2	Solvent Material Properties $\text{Ge}_{0.98}\text{Si}_{0.02}$	81
A.3	Crystal Material Properties Ge	82
C.3	Dimensionless Rotational Values	88

NOMENCLATURE

C :	Dimensionless Concentration = $\frac{c - c_o}{\Delta c}$
c :	Solute Concentration
c_o :	Reference Solute Concentration
c_p :	Specific Heat at Constant Pressure (J/g·K)
Δc :	Change in Concentration
Gr :	Grashof Number = $\frac{\beta_T \Delta T \rho^2 g L^3}{\mu^2}$
g :	Gravity (cm/s ²)
g_o :	Earth Gravity = 981 cm/s ²
L_f :	Latent Heat (cal/g)
N :	Dimensionless Parameter = $\frac{\beta_c \Delta c}{\beta_T \Delta T}$
Nu	Nusselt Number = $\frac{hL}{k}$
P :	Dimensionless Pressure = $\frac{pL}{\mu u_o}$
Pr :	Prandtl Number = $\frac{c_p \mu}{k}$
p :	Pressure (g/cm ³)
Re :	Reynolds Number = $\frac{\rho u_o L}{\mu}$
r :	Radial Direction (cm)
Sc :	Schmidt Number = $\frac{\nu}{\alpha_c}$
T :	Temperature (K)
ΔT :	Change in Temperature (K)
u_o :	Reference Velocity (cm/s) = $\sqrt{g \beta_T \Delta T L}$
U_r :	Dimensionless Radial Velocity = $\frac{u_r}{u_o}$
u_r :	Radial Velocity (cm/s)
U_z :	Dimensionless Axial Velocity = $\frac{u_z}{u_o}$

u_z :	Axial Velocity (cm/s)
U_θ :	Dimensionless Angular Velocity = $\frac{u_\theta}{u_o}$
u_θ :	Angular Velocity (rad/s)
w :	Speed $\sqrt{u_r^2 + u_\theta^2 + u_z^2}$ (cm/s)
z :	Axial Direction (cm)

Greek Symbols

α_c :	Solutal Diffusivity of the Species (cm ² /s)
β_c :	Solutal Expansion Coefficient
β_T :	Thermal Expansion Coefficient
γ :	Angle of tilt applied to gravity (rad)
Θ :	Dimensionless Temperature = $\frac{T - T_m}{\Delta T}$
θ :	Rotation Angle about the z-Axis
k :	Thermal Conductivity (W/cm·K)
μ :	Viscosity (g/cm·s)
ρ :	Density (g/cm ³)
ν :	Kinematic Viscosity = $\frac{\mu}{\rho}$
ω :	Angular Velocity (rad/s)
Ω :	Rotational Speed (rpm)

Subscripts

m :	melt
s :	solid

CHAPTER 1

Introduction

With today's technological demands, the production of purer crystal structures of semiconductor materials is required to increase the performance of all modern electronics. This includes telecommunications to consumer electronics, from gaming consoles to life saving medical equipment. The performance of these semiconductor materials is reliant on the consistent internal arrangement of the atoms within the three-dimensional crystal structure being uniform and uncontaminated. Each crystal structure can be broken down into a single unit cell which is the smallest configuration of arranged atoms that give the material its unique characteristics. When these unit cells are repeated next to each other a crystal lattice is formed. To ensure the highest level of purity, homogeneity and crystalline perfection, these crystals have to be grown under very specific conditions. Today one of the most popular methods of crystal growth encompassing these very specific conditions is crystallization from the melt. Unfortunately, this scheme of crystal growth has complications which arise that do not allow the crystal to be grown in a perfect three-dimensional arrangement of atoms or molecules. These complications have a generalized name called growth defects. These growth defects include vacancies (a missing atom in the crystal lattice), interstitials (an extra atom that has squeezed itself into the crystal lattice), substitutionals (an atom that has replaced an atom of the crystal lattice), dislocations (atoms that are misaligned in the crystal lattice) and grain boundaries (two small grains of crystal having different crystallographic orientations). All these defects lead to the reduction of the grown crystal's quality. Thus the research of crystal growth is intended to closer explain the relation between the resulting crystal quality, the physical properties and the growth parameters.

The influence of gravity on crystal growth is a large factor influencing the growth process as it is the cause of the buoyant force which affects the mechanisms of mass and heat transport throughout the system. With gravity on Earth known as the terrestrial condition, the hotter less dense fluid in the crystal melt rises while cooler denser fluid sinks. This is the convective flow that leads to the irregular

spread of the dopant as well as considerably effecting the perfection of the growing crystal. This is the motivation behind research in microgravity conditions, such as that onboard the International Space Station where there will be no buoyancy induced convection or hydrostatic pressure, which can lead to a better understanding of crystal growth. Currently there are a number of different methods of crystal growth from the melt that are being studied. All these techniques require similar conditions throughout the melt in order to obtain optimum growth conditions. Some of these conditions include having a symmetric heat distribution, a symmetric flow, a smoothed concentration of dopant along the growth interface, and an interface containing the least amount of curvature as possible [1]. The most popular of these techniques are the Bridgman technique, the Czochralski growth technique, the float zone technique and the traveling solvent method (TSM), also known as the traveling heater method (THM).

The Bridgman technique was designed for the purpose of growing metallic crystals. An ampoule contains the melt which is translated through the axial temperature gradient in a furnace. With this technique the whole feed material is molten and a two zone vertical furnace is used for the crystal growth. The upper heater is at a higher temperature keeping the feed material in a liquid state while the lower heater is slightly cooler allowing the crystal to form. This technique allows for the shape of the growing crystal to be controlled by the crucible, but by the crucible having contact with the melt and the crystal, strain is caused which may result in differently aligned crystals known as grain boundaries.

Research has been done on the Bridgman technique by Ouyang *et al.* [2] who modeled a numerical simulation for steady-state Bridgman growth and found that the curvature of the melt interface depends on the variations of thermal conductivities. Martinez-Tomaz *et al.* [3] showed that CdTe has a very long response time in attaining a stationary value of both the growth rate and the axial thermal gradient using the Bridgman technique. Lan *et al.* [4] conducted a three-dimensional analysis of flow and segregation with the application of axial and transversal magnetic fields applied to the Bridgman technique where the transverse magnetic field was found to be more effective in suppressing the convection throughout the system.

In the Czochralski technique, the polycrystalline material is first melted in a heated crucible until the desired initial temperature field is reached. To initiate crystal growth a small crystal seed is dipped into the melt and pulled vertically upward from the melt in a way so that the crystal grows at a constant diameter except for the initial and final stages. The crystal rod and crucible are usually rotated in opposite directions to reduce asymmetries in the temperature gradient and to promote better mixing of the melt. With this technique there is difficulty in predicting reliably the shapes of the three free boundaries between the crystal, the melt and the gas, and the dynamics of the triple point adjacent to all three phases [5].

The Czochralski technique has been studied by Ziao *et al.* [6] who developed a CZ simulation for quick realistic computations on personal computers. The effectiveness of this method was illustrated with a semiconductor compound CZ growth system. This package was lacking the incorporation of a moving crystal/melt interface and transient phenomena. Tanaka *et al.* [7] studied the melt surface temperature in CZ silicon growth. It was found that depending on crucible rotation rates the temperature changed in four observable patterns. Vizman *et al.* [8] modeled a three-dimensional numerical simulation of thermal convection and made comparisons to experimental results. High amplitudes of temperature fluctuations were discovered to exist near the solidification interface. The numerical and experimental results were found to be in close agreement deep inside the melt rather than those close to the solidification interface.

The float zone technique commonly applied in microgravity conditions contains a melt zone between a lower seed material and an upper feed rod. This melt zone is maintained by applying localized heating where the melt zone is translated upwards along the rod so that the crystal is growing on the seed and at the same time melting the feed material. The system is kept crucible free and the melt is held in place by surface tension. With terrestrial conditions, the melt zone height is limited as the liquid will run if the molten zone is too large. This limits the possible diameter of crystals grown under gravity. In microgravity the maximum zone height is given by the circumference of the crystal [9].

Saghir *et al.* [10] conducted a numerical simulation of float zone crystal growth of $\text{Bi}_{12}\text{GeO}_{20}$ under terrestrial and microgravity conditions. Microgravity conditions showed a weaker convection resulting in a much more stable float zone. Campbell *et al.* [11] grew $\text{Ge}_{1-x}\text{Si}_x$ ($x \leq 10\%$) single crystal with the float zone technique. Deviations were observed from regular convex interface morphology as a function of silicon concentration. This only occurred with the combination of free melt surfaces, which indicated that it was due to solutal Marangoni convection which occurs when surface tension is present. Dold *et al.* [12] measured the growth rates of float zone silicon crystals using the heat pulse technique. The heat pulses generated finely spaced periodic time markers which overlay the dopant inhomogeneities caused by the instabilities in the melt. Dopant striations were formed that were not completely parallel to the markers, which showed the influence of concentration variation in the boundary layer.

The traveling solvent method is another very promising technique used to produce pure and homogeneous crystals. The TSM process has been tested on many alloys producing uniform and uncontaminated crystal products. The ampoule in this system contains the seed material at the bottom, the melt in the middle and the feed material on top. This method goes through the melt phase differently than in the Bridgman, Czochralski and float zone techniques. In the Bridgman technique there is no feed rod on top of the melt; in the Czochralski there is a melt between the solution and the seed; and in the float zone technique surface tension holds the melt together. The greatest difference between the TSM method and other melt growth methods is that of the material composition where the top two stages differ in order to successfully apply a lower heater thermal gradient to the system. This allows for two things. Firstly, with the lower heater thermal gradient, the crystal can be grown with less heater thermal stresses. Secondly, rather than melting the feed material, it is softened and the dopant is induced to diffuse into the solution zone giving a much smoother concentration transition. The way in which the TSM method works is, the heated solution zone passes through the polycrystalline feed rod in order to grow the single crystal. This solution zone is heated by radiation usually given off by halogen lamps encompassed in a mirror furnace. This TSM ampoule which contains the crystal, solution zone and the feed rod is then translated through the common focus of the furnace's mirrors at a rate of about 4mm/day. Since the TSM process takes place

at a lower temperature than other conventional methods, contamination from the container is reduced. The reduced operating temperature also leads to a lower ambient pressure within the growth environment, a reduced risk of ampoule fracture, and a reduction in the crystal's defect density.

Matasumoto *et al.* [13] carried out a numerical simulation of InP crystal growth by the traveling solvent method. It was found that in the case of strong buoyancy convection, constitutional super cooling tended to occur near the interface, whereas it did not appear in the case of weak buoyancy convection. Lent *et al.* [14] performed a numerical simulation of TSM growth of ternary semiconductor materials under suppressed gravity conditions. It was found that the position of the thermal profile severely affected the characteristics and stability of the growing crystal. Various levels of applied magnetic field were applied, aligned and misaligned. An upper limit of misalignment was found at which increased alignment would cause the growth interface to lose stability. The convective flow due to small misalignment was found to increase mixing in the horizontal plane and was beneficial for the growth process. Martinez-Tomas *et al.* [15] studied the effects of thermal conditions in the TSM growth of HgTe. The study showed the heat transfer between the furnace and the ampoule for central positions increased the length of the liquid zone. The calculated concentration field showed a uniform concentration core in the liquid zone and a step concentration along the growth interfaces indicating the importance of convection.

The TSM has also been used in conjunction with a rotating magnetic field (RMF) in an attempt to slow buoyancy-induced convection while processing CdTe crystal [16]. The influence of the magnetic field was tested under terrestrial and microgravity conditions. The study showed that under microgravity conditions the application of the RMF can be used to overcome residual buoyancy-induced convection and used to control the uniformity of the solution-zone composition at the growth front without appreciable modification of the growth interface shape [16].

Studies have been done with steady and accelerated crucible rotation added to the crystal growth system. The application of rotation to the system is an attempt to further control the convective flow throughout the melt. With rotation, it has been

found that convection and dopant segregation can be affected considerably and the effect is similar to that of an axial magnetic field [17]. Ampoule rotation decreases the intensity of convection and stretches the flow axially. When convection is weak, flow can be suppressed almost completely by ampoule rotation and the dopant becomes diffusion-controlled. Lan *et al.* [17] studied the effects of ampoule rotation on the flow and dopant segregation in the vertical Bridgman crystal growth.

Okano *et al.* [18] applied THM to the numerical modeling of a simulation for the growth of GaSb from a Ga-solution. The effects of crucible temperature, rotation and material on the crystal interface shape were studied. It was found that with increasing crucible temperature, the interface curvature became larger. The application of rotation was successful in suppressing the natural convection in the solution and in obtaining an interface with less curvature. With lower crucible temperatures, the interface shape was slightly convex toward the crystal and the effect of crucible rotation was not significant.

Lan *et al.* [19] found that the use of steady ampoule rotation is effective in suppressing 3D characteristics of unsteady heat flow. Ampoule rotation of only 10 rpm suppressed the 3D effects considerably both on symmetry breaking and unsteadiness. It was also shown that, for the asymmetric growth condition due to ampoule tilting or asymmetric heating, ampoule rotation was effective in minimizing the asymmetry. Lan *et al.* [20] also studied the effects of steady ampoule rotation versus accelerated rotation on vertical zone melting crystal growth. It was found that the steady ampoule rotation, at low speeds of 3-5 rpm significantly affected the heat flow and the interface shape. Interface inversion from concave to convex was achieved. With the same rotation speed, it was found that with the accelerated crucible rotation technique (ACRT) showed similar effects but was less effective. ACRT was found to induce severe growth and re-melting that could be responsible for growth striations. Bars *et al.* [21] conducted a two-dimensional numerical study of convection during THM growth of CdTe with accelerated crucible rotation. Their research showed that ACRT is effective in increasing mixing in the solution zone and in obtaining higher growth rate limits.

In this thesis, a three-dimensional numerical simulation for the growth of $\text{Ge}_{1-x}\text{Si}_x$ by the traveling solvent method has been carried out with the application of crucible rotation. The crucible rotation is an attempt to control the buoyancy induced convection throughout the melt and to suppress the three-dimensional characteristics of unsteady heat flow. Speeds of up to 10 rpm have been considered, as references [18-20] have shown that these speeds are more than sufficient to observe a considerable change in flow throughout the solution zone. These rotational speeds have been applied to both the terrestrial and microgravity condition. Since all furnaces have a lagging heater profile, which in some cases, may be so small that it goes unnoticed, the heating element will produce unsymmetrical heating throughout the system. So, in this thesis, the uniform heating and non-uniform heating condition have been studied. It is the intention of this thesis that by applying symmetrical and unsymmetrical heating to the crystal growth system to closer explain experimentally obtained results and to observe if added ampoule rotation can benefit or improve the growing crystal's quality.

CHAPTER 2

Theory and Setup

2.0 Traveling solvent method

The TSM process has three main phases. The first phase is the starting phase where the $\text{Ge}_{0.85}\text{Si}_{0.15}$ polycrystalline feed rod is on top of the un-melted $\text{Ge}_{0.98}\text{Si}_{0.02}$ polycrystalline material which is above the Ge seed crystal. This phase is complete when the heater has heated up and melted the $\text{Ge}_{0.98}\text{Si}_{0.02}$ material and steady state has been achieved throughout the molten zone. When a steady state has been accomplished, the second phase begins where the heater begins to slowly translate up the polycrystalline feed rod allowing the new single crystal to form along the growth interface and allowing the silicon to diffuse through the solvent from the dissolution interface. Since silicon has a higher melting temperature than germanium, it allows for the solvent to be at the molten state without melting the feed material and allowing the silicon to be softened so it can slowly diffuse into the melt. When the heater has traveled the full length of the rod the second phase has been completed. In the third phase, the heater is shut off and the molten zone at the top of the newly formed single crystal is allowed to cool and solidify ending the crystal growth process. This is shown in Figure 2.1.

2.1 Model Description

A three-dimensional numerical simulation for the growth of $\text{Ge}_{0.98}\text{Si}_{0.02}$ by the traveling solvent method under axial rotation has been modeled. The model is shown in Figure 2.2. The system is described by a fixed cylindrical coordinate system (r, θ, z) that has its origin at the center base of the model. L is the length of the ampoule, D_{outer} is the outer diameter of the quartz tube and D_{inner} is the diameter of the sample within the quartz. Gravity is acting downward but can be adjusted to simulate crucible tilt by giving a value to γ , and Ω is the angular velocity of the ampoule about the z-axis, where it is zero for no rotation. The source (feed rod) is solid, the solvent (melt, solution zone) is liquid and the substrate (crystal) is solid.

The dissolution interface is the interface which is dissolving and allowing the dopant to segregate through the solvent and the growth interface is the interface which is solidifying, forming the new highly pure crystal. U_h is the speed at which the heater moves up along the side of the sample in the z-direction. Experimentally, this speed has been shown to be in the vicinity of about 4mm/day. The heater zone here is described by a temperature heater thermal profile defined by $T_h(r, \theta, z, t)$. This profile is kept stationary for this simulation as quasi steady state condition is assumed due to the slow heater translational speed. The ampoule pulling speed is set to be the steady melting and growth rates, where this assumption is viable and can reduce computational power [22]. Further simplification is in the assumption that the crystal size and thermal environment are unchanged throughout the simulation. Also, the thermal boundary conditions on the ampoule wall are fixed and remain unchanged during the growth process. This model incorporates all the governing equations of energy transfer, mass transport, momentum and continuity where the use of the commercial computational code FIDAP has been used as the solver. FIDAP is a well known finite element software for the simulation of crystal growth and provides sufficient capabilities for accurate simulations of fluid flow and heat transfer for this process [23-24]. It has been used numerous times by researchers for comparing experimental results to numerical results, being in very close agreement to experimentally obtained data [25-26].

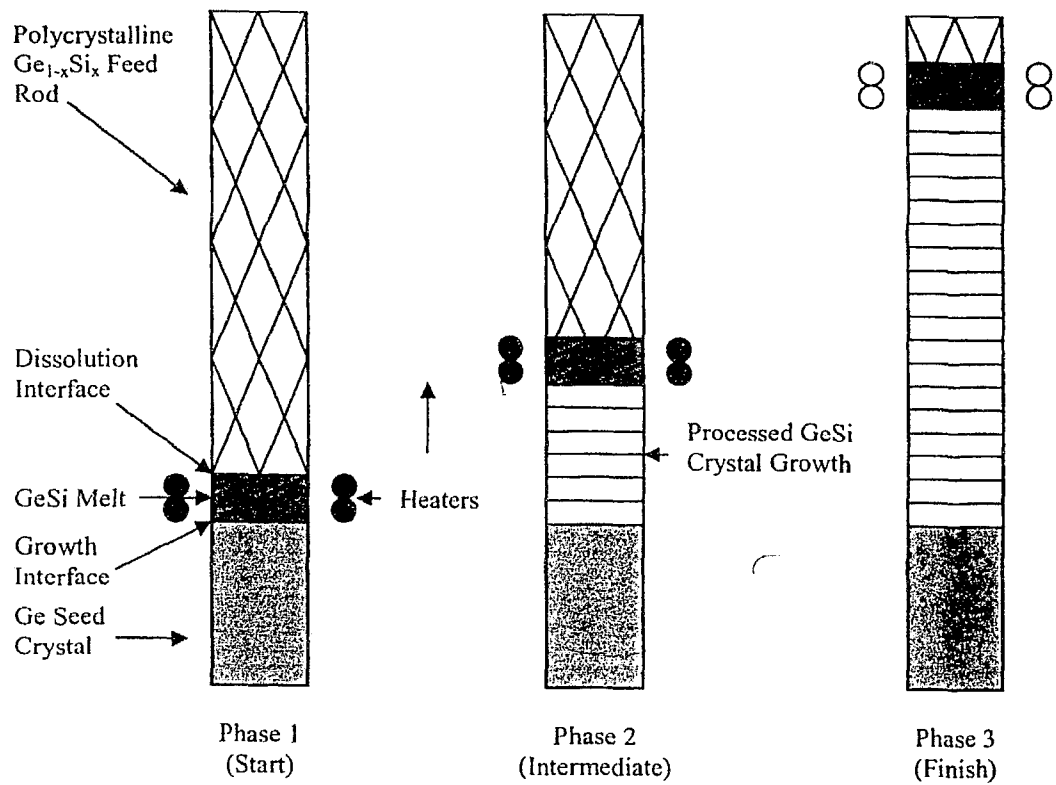


Figure 2.1 TSM process

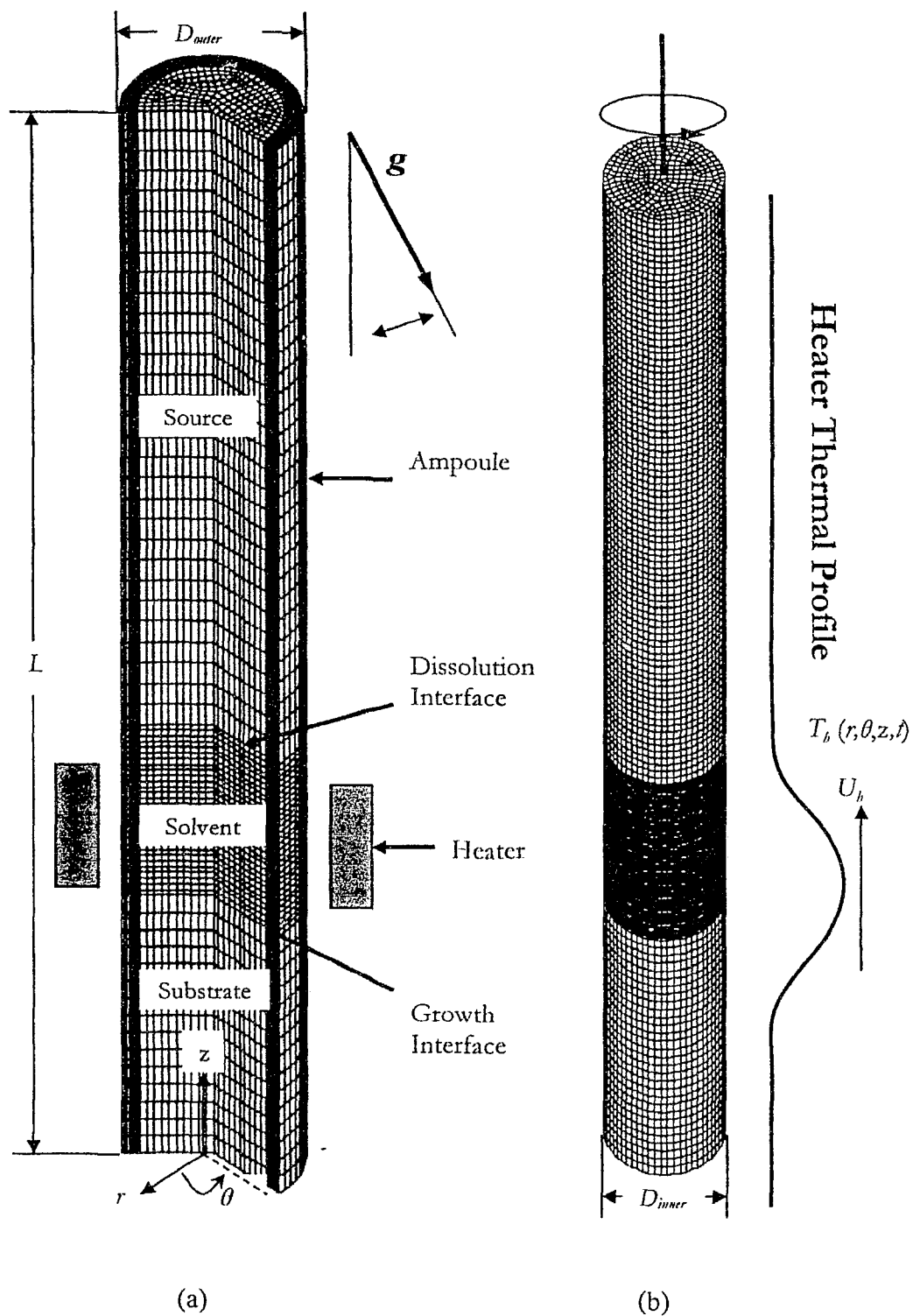


Figure 2.2 Model Description

(a) TSM model with ampoule.

(b) Finite element mesh with applied heater thermal profile.

2.2 Governing Equations

This mathematical simulation incorporates the three-dimensional steady state Navier-Stokes equations combined with the energy transfer, mass transport and continuity equations. The equations used are in cylindrical form for simplification in dealing with a cylindrical flow. The simulation is carried out in non-dimensional form. Using dimensional analysis helps convergence through out the iterative process by providing the software with simpler numbers to be used in the matrices to be solved. Dimensional analysis leaves the system with all the governing equations being dimensionless and optimizes convergence of the system in the solver. Some dimensionless numbers used are the Reynolds number, Prandtl number and Grashof number. The equations that are non-dimensionalized are shown in 2.2.1-2.2.4.

2.2.1 Navier-Stokes Equations

The commonly used Navier-Stokes equations under non-turbulent conditions fully describe the motion of an incompressible fluid and are used to calculate the rate of flow, pressure and positions of any free surface. The following are the Navier-Stokes equations used in this model, where in the r - Component the last 2 terms have been added due to the effect of rotation on the system. They are the centrifugal and coriolis forces respectively. In the z - Component the last term is the coupling term which incorporates buoyancy and uses the boussinesq approximation. The governing equations used neglect the transient terms as steady state has been assumed.

r - Component

$$\rho \left[u_r \frac{\partial u_r}{\partial r} + \frac{u_\theta}{r} \frac{\partial u_r}{\partial \theta} - \frac{u_\theta^2}{r} + u_z \frac{\partial u_r}{\partial z} \right] = -\frac{\partial p}{\partial r} + \mu \left[\frac{1}{r} \frac{\partial}{\partial r} \left(r \frac{\partial u_r}{\partial r} \right) + \frac{1}{r^2} \frac{\partial u_r^2}{\partial \theta^2} + \frac{\partial^2 u_r}{\partial z^2} - \frac{u_r}{r^2} - \frac{2}{r^2} \frac{\partial u_\theta}{\partial \theta} \right] - \rho \omega^2 r - \rho 2\omega u_\theta \quad (1)$$

θ - Component

$$\rho \left[u_r \frac{\partial u_\theta}{\partial r} + \frac{u_\theta}{r} \frac{\partial u_\theta}{\partial \theta} + \frac{u_r u_\theta}{r} + u_z \frac{\partial u_\theta}{\partial z} \right] = -\frac{1}{r} \frac{\partial p}{\partial \theta} + \mu \left[\frac{\partial}{\partial r} \left(\frac{1}{r} \frac{\partial}{\partial r} (r u_\theta) \right) + \frac{1}{r^2} \frac{\partial^2 u_\theta}{\partial \theta^2} + \frac{2}{r^2} \frac{\partial u_r}{\partial \theta} + \frac{\partial^2 u_\theta}{\partial z^2} \right] \quad (2)$$

z - Component

$$\rho \left[u_r \frac{\partial u_z}{\partial r} + \frac{u_\theta}{r} \frac{\partial u_z}{\partial \theta} + u_z \frac{\partial u_z}{\partial z} \right] = -\frac{\partial p}{\partial z} + \mu \left[\frac{1}{r} \frac{\partial}{\partial r} \left(r \frac{\partial u_z}{\partial r} \right) + \frac{1}{r^2} \frac{\partial^2 u_z}{\partial \theta^2} + \frac{\partial^2 u_z}{\partial z^2} \right] + \rho g [\beta_T (T - T_m) - \beta_c (c - c_0)] \quad (3)$$

Where u is defined as velocity and r corresponds to the radial direction, θ the angular direction and z the axial direction. The viscosity is identified as μ , the density as ρ and the pressure as p . T is the temperature, T_m is the melt temperature, c is the concentration and c_0 is the reference concentration. In addition to this β_T and β_c are the thermal and solutal expansion coefficients respectively.

2.2.2 Energy Transfer Equation

The energy transfer equation describes the change in temperature throughout the model.

$$\rho c_p \left[u_r \frac{\partial T}{\partial r} + \frac{u_\theta}{r} \frac{\partial T}{\partial \theta} + u_z \frac{\partial T}{\partial z} \right] = k \left[\frac{1}{r} \frac{\partial}{\partial r} \left(r \frac{\partial T}{\partial r} \right) + \frac{1}{r^2} \frac{\partial^2 T}{\partial \theta^2} + \frac{\partial^2 T}{\partial z^2} \right] \quad (4)$$

Here c_p is the specific heat and k is the thermal conductivity.

2.2.3 Mass Transport Equation

The mass transport equation describes segregation of the dopant throughout the model.

$$u_r \frac{\partial c}{\partial r} + \frac{u_\theta}{r} \frac{\partial c}{\partial \theta} + u_z \frac{\partial c}{\partial z} = -\alpha_c \left[\frac{1}{r} \frac{\partial}{\partial r} \left(r \frac{\partial c}{\partial r} \right) + \frac{1}{r^2} \frac{\partial^2 c}{\partial \theta^2} + \frac{\partial^2 c}{\partial z^2} \right] \quad (5)$$

α_c is the solutal diffusivity.

2.4 Continuity Equation

$$\frac{1}{r} \frac{\partial}{\partial r} (ru_r) + \frac{1}{r} \frac{\partial u_\theta}{\partial \theta} + \frac{\partial u_z}{\partial z} = 0 \quad (6)$$

2.3 Dimensional Analysis

Engineering designs, particularly those involving fluid mechanics, are greatly influenced by empirical results obtained by experimentation. Dimensional analysis provides an approach for choosing relevant data and assists in presenting the data in a suitable way. This leads to a better understanding of results so they may be applied appropriately in upcoming research. The dimensionless variables used to non-dimensionalize the Navier-Stokes, energy transfer, mass transport and continuity equation are:

$$R = \frac{r}{L}, \quad \theta^* = \theta, \quad Z = \frac{z}{L}, \quad U_r = \frac{u_r}{u_0}, \quad U_\theta = \frac{u_\theta}{u_0}, \quad U_z = \frac{u_z}{u_0}, \quad P = \frac{pL}{\mu u_0}, \quad \Theta = \frac{T - T_m}{\Delta T},$$

$$C = \frac{c - c_0}{\Delta c}, \quad \nu = \frac{\mu}{\rho}, \quad u_0 = \sqrt{g \beta_T \Delta T L}, \quad \text{Re} = \frac{\rho u_0 L}{\mu}, \quad \text{Pr} = \frac{c_p \mu}{\kappa}, \quad \text{Sc} = \frac{\nu}{\alpha_c},$$

$$\text{Gr} = \frac{\beta_T \Delta T g L^3 \rho^2}{\mu^2}, \quad N = \frac{\beta_c \Delta c}{\beta_T \Delta T}$$

Where L is the reference length, u_0 is the reference velocity, Re is the Reynolds number Pr is the Prandtl number and Gr is the Grashof number. The Reynolds number is the ratio of inertia to viscous forces, the Prandtl number is the ratio of momentum to thermal diffusivities and the Grashof number is the ratio of buoyancy to viscous forces.

2.4 Dimensionless Governing Equations

The dimensionless Navier-Stokes, energy transfer, mass transport and continuity equations are given as follows:

2.4.1 Navier-Stokes Equations

r – Component

$$\text{Re} \left[U_r \frac{\partial U_r}{\partial R} + \frac{U_\theta}{R} \frac{\partial U_r}{\partial \theta} - \frac{U_\theta^2}{R} + U_z \frac{\partial U_z}{\partial Z} \right] = -\frac{\partial P}{\partial R} + \nabla^2 U_r - \frac{U_r}{R^2} - \frac{2}{R^2} \frac{\partial U_\theta}{\partial \theta} - \text{Re}(\omega^{*2} R + 2\omega^* U_r) \quad (7)$$

θ – Component

$$\text{Re} \left[U_r \frac{\partial U_\theta}{\partial R} + \frac{U_\theta}{R} \frac{\partial U_\theta}{\partial \theta} + \frac{U_r U_\theta}{R} + U_z \frac{\partial U_\theta}{\partial Z} \right] = -\frac{1}{R} \frac{\partial P}{\partial \theta} + \nabla^2 U_\theta + \frac{2}{R^2} \frac{\partial U_r}{\partial \theta} \quad (8)$$

z – Component

$$\text{Re} \left[U_r \frac{\partial U_z}{\partial R} + \frac{U_\theta}{R} \frac{\partial U_z}{\partial \theta} + U_z \frac{\partial U_z}{\partial Z} \right] = -\frac{\partial P}{\partial Z} + \nabla^2 U_z + \frac{Gr}{\text{Re}} [\Theta - NC] \quad (9)$$

2.4.2 Energy transfer Equation

$$\text{RePr} \left[U_r \frac{\partial \Theta}{\partial R} + \frac{U_\theta}{R} \frac{\partial \Theta}{\partial \theta} + U_z \frac{\partial \Theta}{\partial Z} \right] = \nabla^2 \Theta \quad (10)$$

2.4.3 Mass Transport Equation

$$\text{Re} \left[U_r \frac{\partial C}{\partial R} + \frac{U_\theta}{R} \frac{\partial C}{\partial \theta} + U_z \frac{\partial C}{\partial Z} \right] = \frac{1}{Sc} [\nabla^2 C] \quad (11)$$

2.4.4 Continuity Equation

$$\frac{1}{R} \frac{\partial (RU_r)}{\partial R} + \frac{1}{R} \frac{\partial U_\theta}{\partial \theta} + \frac{\partial U_z}{\partial Z} = 0 \quad (12)$$

2.5 Model Boundary Conditions and Heater Profile

2.5.1 Model Dimensions

The simulated model consists of a $\text{Ge}_{0.85}\text{Si}_{0.15}$ source rod with a diameter of 0.8 cm and a length of 3.6 cm. This rod is located on top of a $\text{Ge}_{0.98}\text{Si}_{0.02}$ solvent having the same diameter and a length of 1 cm. Both these zones are positioned above a purely germanium substrate used for the crystal mapping area to grow the crystal. The substrate also has the same diameter but with a length of 1.5cm. Since the silicon has a higher melting temperature than germanium, by having a higher concentration of silicon in the source the solvent can be kept in a liquid state while softening the dissolution interface without any melting. This allows the silicon from the Si-rich source to diffuse through the solvent and deposition itself along the growth interface. Figure 2.3a shows the three-dimensional geometrical model used in the simulation.

2.5.2 Model Boundary Conditions

The zero velocity boundary condition has been applied to the source, the substrate and to the sides of the model as well as on the top and the bottom of the sample as shown in Figure 2.3a. The source and substrate have zero velocity as they are both solid and since this model is simulating crystal growth within an enclosed ampoule, the no slip boundary condition is applied to the outside of the cylinder by applying zero velocity. This model contains 15 percent silicon in the source, 2 percent in the solvent, and 0 percent in the substrate. For this simulation, a boundary condition of 15 percent silicon is applied at the dissolution interface and 2 percent at the growth interface. The application of a concentration value to the growth and dissolution interface is adopted from [27] and the values are obtained from the Si-Ge phase diagram [28] shown in Figure 2.4.

The model uses the latent heat of the material and the continuity of velocities and temperature to be exchanged along the solid liquid interfaces. This is given by:

$$k \frac{\partial T}{\partial z} - k_s \frac{\partial T_s}{\partial z} = \rho_s L_f (u_{zs} - u_{z \text{ interface}}) \quad (13)$$

This simulation also incorporates the quasi steady state model where the transient effect of heat, mass and fluid flow are considered small enough to be negligible. The approximation is justified due to the slow growth rates typical for semiconductor materials as mentioned earlier of about 4 mm/day. Similar approximations have been made by references [29-32].

Velocity = 0
For the circumference of the
cylinder top to bottom

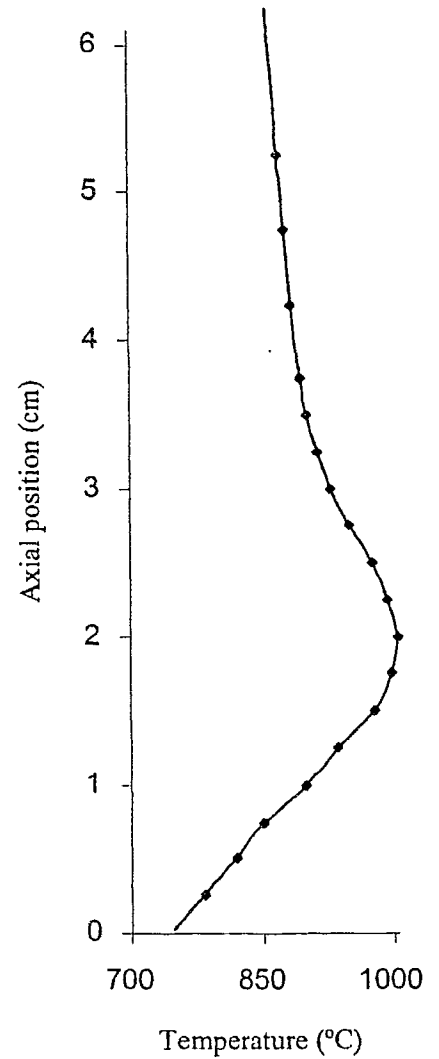
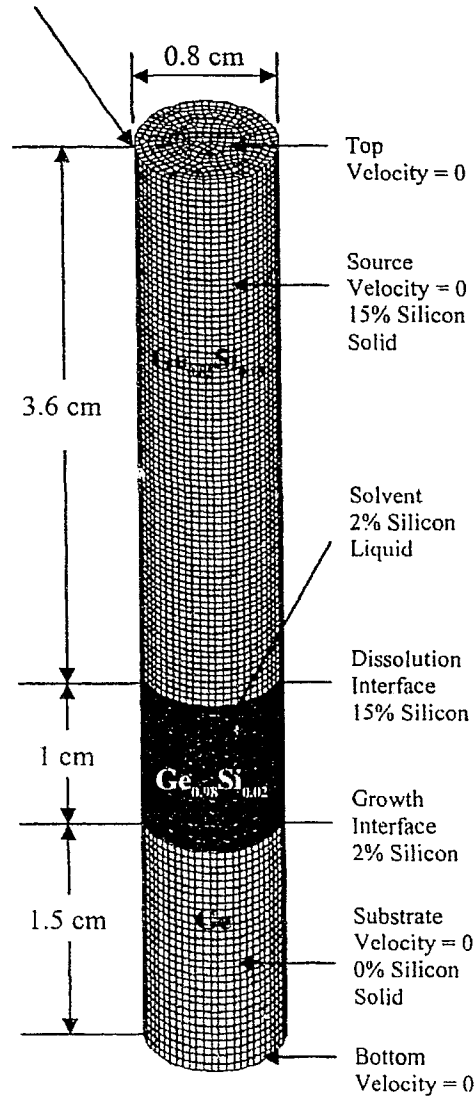


Figure 2.3 Geometrical model and heater profile

- (a) Model dimensions and boundary conditions.
(b) Experimentally measured heater thermal profile.

2.5.3 Heater Profile

The heater thermal profile used for this simulation is measured experimentally at Dalhousie University. The furnace used is illustrated in Figure 2.5 and the experimentally measured temperature profile is shown in Figure 2.3b. This temperature profile was converted to dimensionless units in terms of length and temperature then applied to the model by using a best fit polynomial curve to map it to the input file. The 6th order polynomial curve was found to accurately map this experimentally measured profile. Two heater profile variations were applied to this model, one having symmetric uniform heating around the sample, and another having an unsymmetrical non-uniform heating. Heater furnaces used for crystal growth claim to provide a certain heater profile but in reality this profile will be slightly non-uniform. This non-uniform heater profile therefore simulates the case of a lagging furnace. Experimentally, a lagging heater profile always exists due to the heater coils or convective flow throughout the air between the ampoule and the furnace. This lag may be so slight that throughout the experiment it goes unnoticed, so it is the intention of this simulation to simulate a worst case model to observe how crucible rotation applied to crystal growth may benefit crystal growth and overall improve the grown crystal quality.

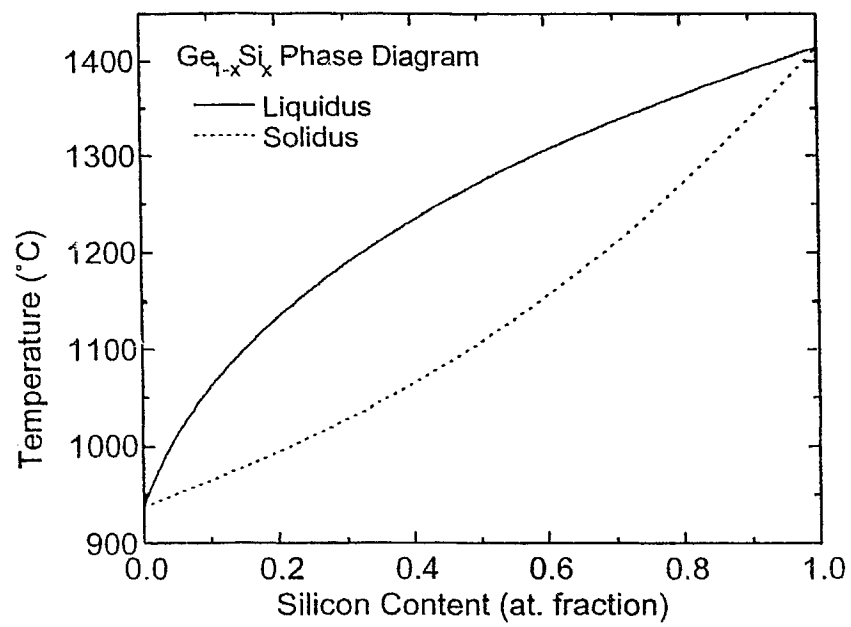


Figure 2.4 Ge-Si phase diagram [28].

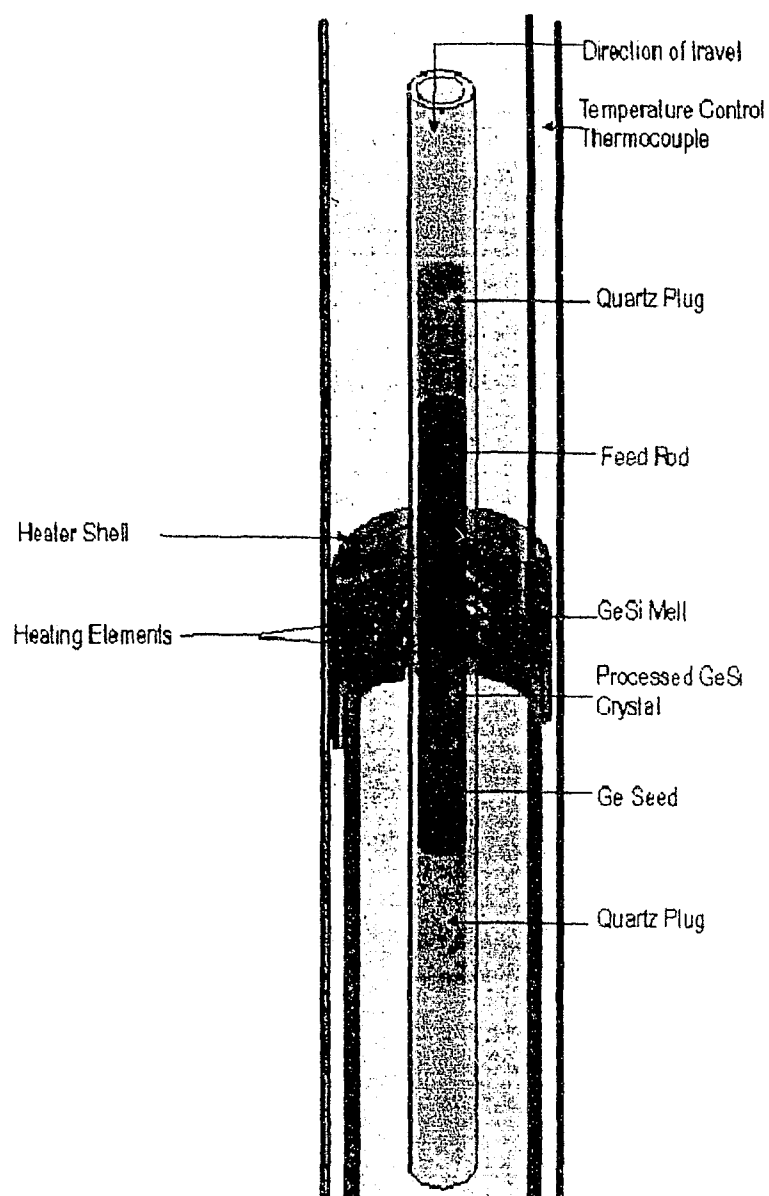


Figure 2.5 TSM Furnace.

2.6 Mesh Sensitivity Analysis

In order to save computational time and to ensure accuracy in results, mesh sensitivity analysis was carried out for this model. The source and the substrate modeled have been kept at a constant mesh of 40 and 30 elements respectively in the axial direction. These zones are kept constant because both of these regions are solid and a finer mesh is not needed in solid regions for improving numerical accuracy as the temperature gradient is less in those areas. Since the full Navier Stokes, energy transfer and mass transport equations were solved in the solvent and this area has a high temperature gradient, the mesh sensitivity is focused on the solvent part only. The solvent was varied from 20 to 120 elements in the axial direction in increments of 20. This was carried out for two models, one containing 40 circumferential elements and the other 60 circumferential elements. Figure 2.6 shows the 12 different solvent meshes considered. For these 12 meshes, the terrestrial case of a uniform heater profile with no rotation was used to calculate and compare the Nusselt number. The Nusselt number is used for mesh sensitivity because it is directly related to the driving force of the simulation. This driving force is the temperature thermal gradient applied to the system. The Nusselt numbers calculated for each case are listed in table 1. Analyzing the results listed, it is seen that the deviation of the Nusselt number starts to decrease at 80 axial elements and almost no change is noticed when reaching 100 and 120 axial elements. From the results listed, 100 axial elements with a circumference of 60 elements was adopted for the numerical model of the solvent region. The mesh for this numerical model is symmetrical and the same mesh is used for all the conditions considered.

The mesh is constructed of tri-linear, eight node, isometric brick elements having temperature, velocities and pressure as unknowns at each node. The iterations of the system continue until an error value of 10^{-4} is found between two consecutive iterations in the temperature, the velocities and the pressures at each node, then the system is considered to have converged. The solution zone is considered to be incompressible and a Newtonian Fluid. In addition this model adopts the Boussinesq approximation where variation in fluid density affects only the buoyancy term; and the fluid density is a function of temperature and silicon concentration.

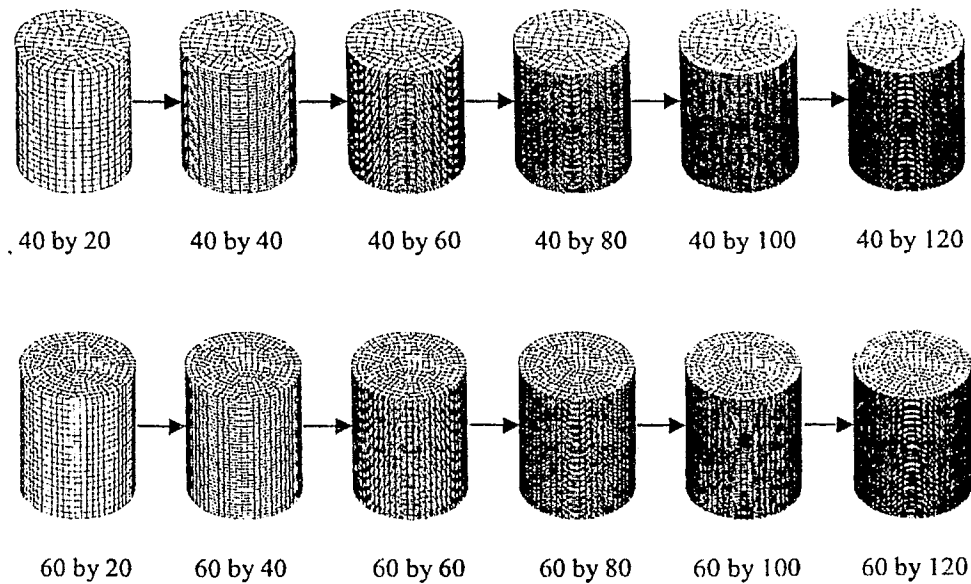


Figure 2.6 Meshes considered for model labeled as circumferential elements by axial elements.

Table 1. Calculated Nusselt numbers for mesh sensitivity

40 Circumferential Elements		60 Circumferential Elements	
Axial Elements	Nusselt Number	Axial Elements	Nusselt Number
20	1.669	20	1.649
40	1.546	40	1.540
60	1.492	60	1.518
80	1.478	80	1.470
100	1.460	100	1.446
120	1.451	120	1.441

CHAPTER 3

Uniform Heating Condition

3.0 Introduction

This chapter presents the results obtained with the uniform heater profile applied to the TSM model under different rotational speeds. The uniform heater profile that was applied is shown in figure 3.1. This chapter is broken down into two sections; the first section discusses the results obtained in the terrestrial condition and the second, the results obtained in the microgravity condition.

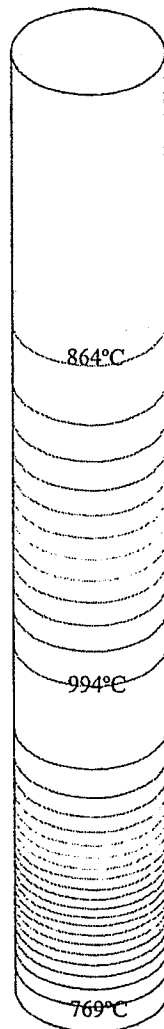


Figure 3.1 Uniform temperature heater thermal profile applied to TSM model (contour lines in increments of 10.8°C).

3.1 Terrestrial Condition

The terrestrial condition simulates the effect of gravity on earth where $g = g_0 = 9.81 \text{ m/s}^2$. In this terrestrial condition the speeds of 0, 2, 5 and 7 rpm were applied to the TSM crystal growth system. The results of the axial velocity contours are shown in Figures 3.2 – 3.5. In these figures, a three-dimensional model is displayed accompanied by two planes cut horizontally and vertically showing the axial velocity contours, two surface graphs displaying the three-dimensional axial velocity variation and an axial velocity variation plot. The horizontal plane is cut 0.25 cm below the dissolution interface where the convective current is relatively unsteady due to the silicon diffusion from the dissolution interface and the vertically cut plane is cut along the r-z plane with unsymmetrical heating. The surface graphs plot the axial velocity at the horizontally cut plane and at 0.03 cm above the growth interface where the velocity variation plot is also graphed.

In examining the results of the speed contours, it can be seen that in Figure 3.2 at 0 rpm, the horizontally cut plane has a slight dissymmetry near the center. This dissymmetry is the result of the three-dimensional characteristic flow within the solution. The horizontal view shows that just below the dissolution interface the two highest velocities occur at the center and close to the wall, here there is an axial velocity of -0.202 cm/s at the center where it is negative because the flow is moving downwards and 0.143 cm/s close to the wall, where it is positive because the flow is moving upwards. Just below the horizontal view, the three-dimensional velocity variation and the vertically cut plane of the solvent can be observed. In the vertical plane it can be seen that three flow cells have been formed. The velocity contours here appear to have a slight dip in the upper portion of the middle contour cell. This dip demonstrates that the velocity has a sudden drop in this region giving a slight unsteadiness to the solvents flow. Similar to this dip, a slight upward groove appears in the lower portion of the center flow cell but it is not shown to be quite as strong. Neither of these velocity drops is desirable for the crystal growth process. Here the maximum velocity also occurs at the center and the sides at -0.458 cm/s and 0.315 cm/s respectively. Below the vertical view of Figure 3.2, the surface graphs show the three-dimensional velocity variation and below the velocity across the solvent at 0.03 cm above the growth interface is graphed. A noticeable variation in axial velocity

can be observed ranging from 0.037 cm/s to -0.06 cm/s, where for good crystal growth quality a minimal amount of velocity variation is desired along this interface.

In Figure 3.3 where a rotational speed of 2 rpm has been applied, looking at the horizontal view, it is observed that the axial velocity at the center and along the sides have slightly decreased from -0.202 cm/s and 0.143 cm/s to -0.199 cm/s and 0.131 cm/s respectively. Here there is a 0.003 cm/s decrease at the center and a 0.012 cm/s decrease along the sides. Moving down to the vertical view it is seen that the dip that had formed in the previous case with 0 rpm has lessened meaning that this region has become less unsteady and the groove that was observed at the bottom of the center flow cell has completely disappeared. In comparing the maximum velocities in the center and at the sides it can be observed that the center velocity has decreased 0.009 cm/s and at the sides by 0.018 cm/s. This decrease in flow velocity means that the application of crucible rotation has weakened the convective flow in the system. The graph at the bottom right of Figure 3.3 also illustrates that the flow velocity at 0.03 cm above the growth interface close to the center has also decreased, being more advantageous for crystal growth.

With the application of 5 rpm (see Figure 3.4) the flow in the horizontal plane has been further suppressed to -0.170 cm/s at the center and to 0.117 cm/s at the sides, having further decreased the velocities from the case of 2 rpm by 0.029 cm/s and 0.014 cm/s. Also it is observed that a new unsteady jagged contour has formed, but this is not a problem as the main concern is to suppress the convective flow and to have steadiness in velocity contours along the growth interface. In the vertical view the dip seen in the previous two cases at the top of the center flow cell has completely disappeared and the flow has become more axi-symmetric. Here the flow at the center and the sides has been reduced to -0.386 cm/s and 0.262 cm/s respectively. This increase in rpm has lessened the flow velocity by 0.063 cm/s and 0.035 cm/s at the center and the sides from the previous case. In analyzing the velocity graph at 0.03 cm above the growth interface it can be seen that close to the center of the inflow the velocity has been reduced to -0.042 cm/s, further improving crystal growth conditions along the growth interface.

At 7 rpm shown in Figure 3.5, the horizontal plane's velocities at the center and at the sides have been further reduced to -0.142 and 0.108 respectively and also it is observed that this unsteady jagged contour is still present but not as abrupt. The vertical view shows almost no change in shape of the three velocity contour cells in comparison to that of Figure 3.4. Here the maximum velocity at the center and the sides has been reduced to - 0.328 cm/s and 0.233 cm/s, having decreased the flow velocity at the center and the sides from the case of 5 rpm by 0.058 cm/s and 0.029 cm/s respectively. The flow graphed at 0.03 cm above the growth interface close to the center has also decreased to -0.03 cm/s. In comparing this velocity to the case of 0 rpm, it is observed that the intensity of the flow along the growth interface has been reduced by 0.173 cm/s which is very beneficial for the improvement of crystal growth quality.

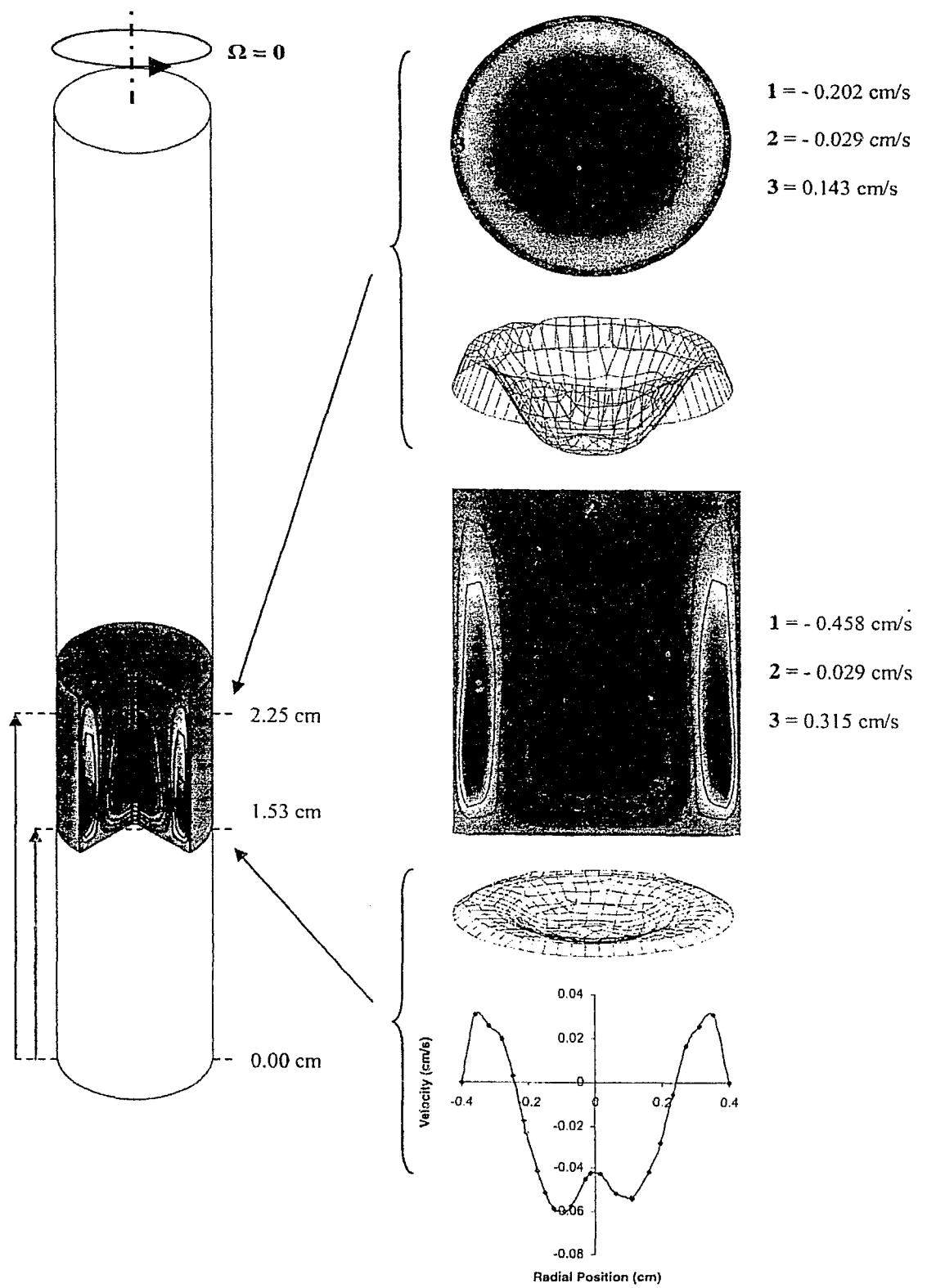


Figure 3.2 Axial direction velocity contours for $\Omega = 0$ (terrestrial condition).

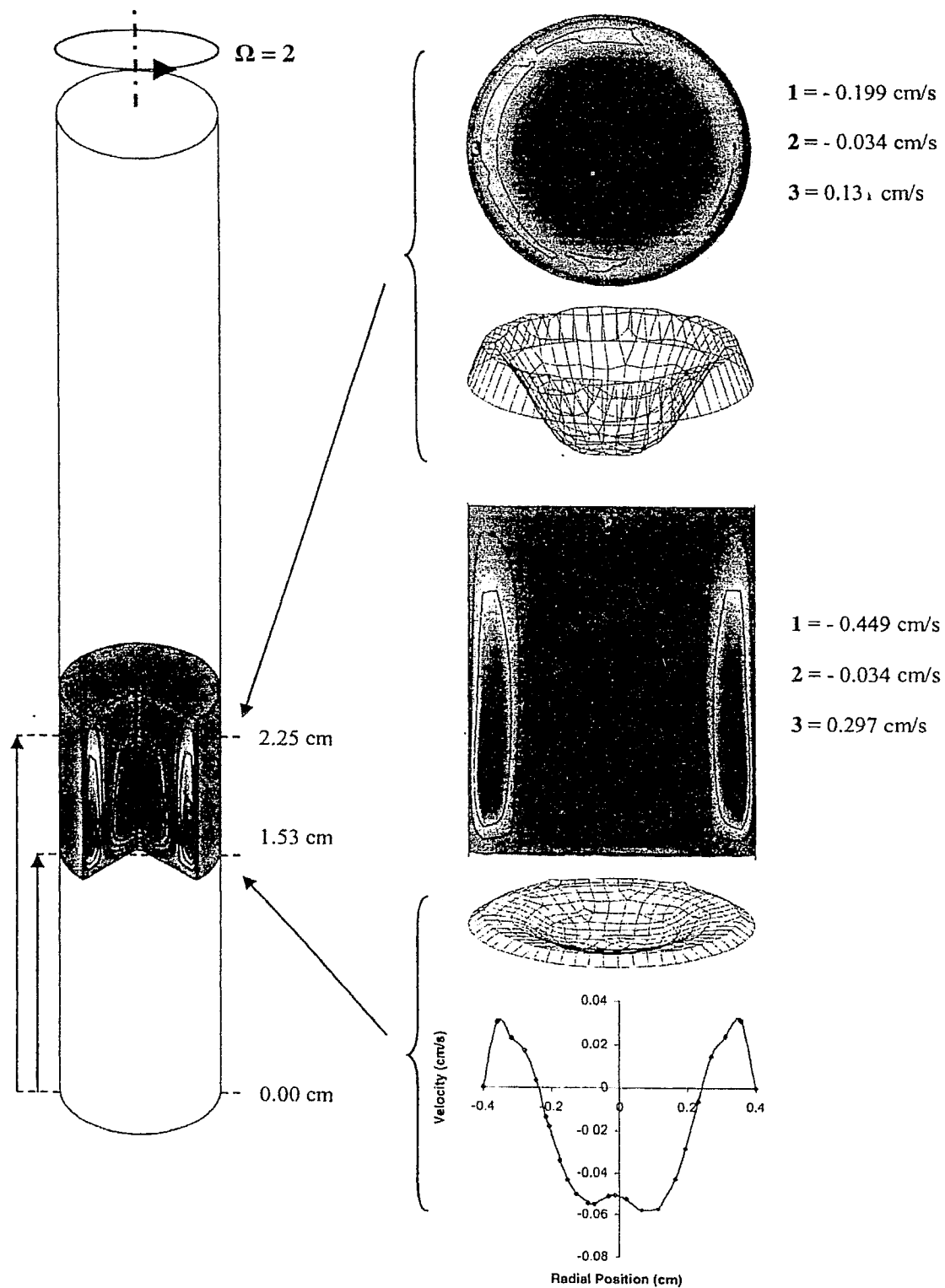


Figure 3.3 Axial direction velocity contours for $\Omega = 2$ (terrestrial condition).

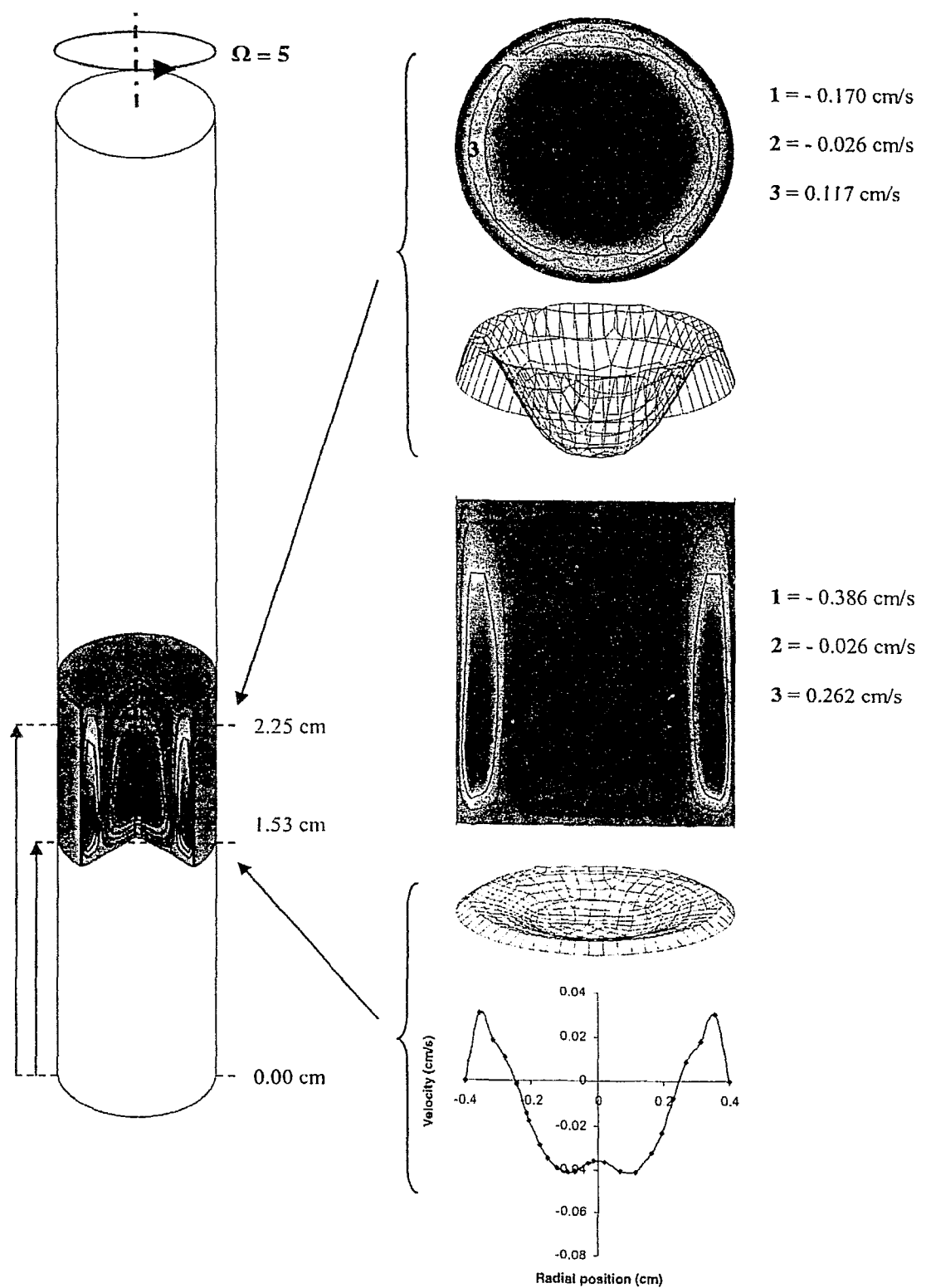


Figure 3.4 Axial direction velocity contours for $\Omega = 5$ (terrestrial condition).

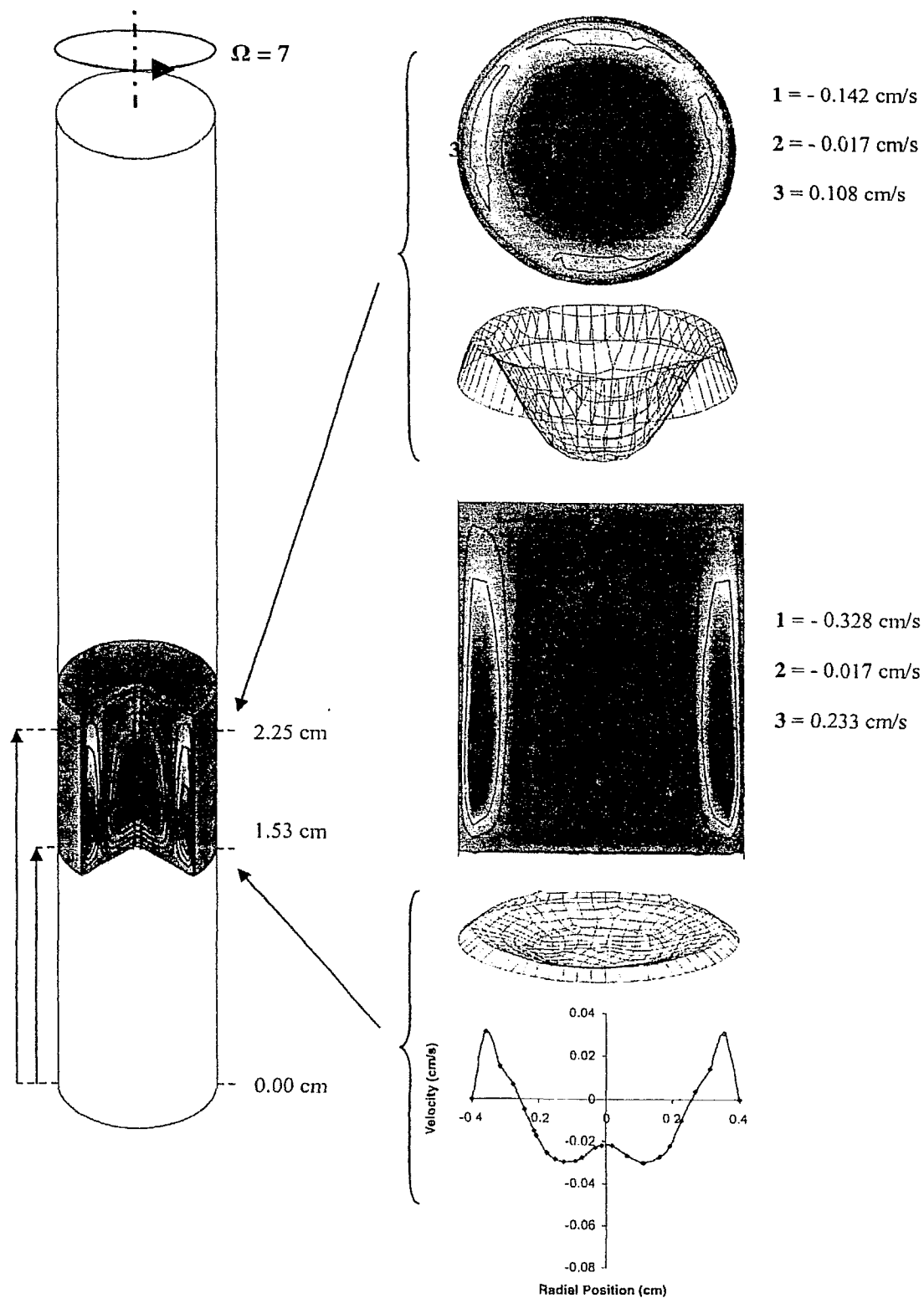


Figure 3.5 Axial direction velocity contours for $\Omega = 7$ (terrestrial condition).

Looking at the graph in Figure 3.6 the maximum speed of flow is graphed as a function of rotation from 0 to 7 rpm. In this graph it can be seen that as the rotational speed is increased the maximum speed in the solvent decreases linearly. This reveals that the application of rotation is successful in helping suppress the convective flow throughout the solution zone.

The concentration contours throughout the solvent are shown for the rotational speeds of 0, 2, 5 and 7 rpm in Figures 3.7 – 3.10. These Figures show a three-dimensional model accompanied to the right by two horizontally cut planes one cut mid-way in the solvent at 0.5cm above the growth interface and the other at 0.03 cm above the growth interface, two three-dimensional silicon concentration surface graphs located at 0.5 and 0.03 cm above the growth interface and a vertically cut plane along the center axis in the r-z plane. The horizontally cut planes mid-way in the solvent were chosen to observe how the silicon is behaving along its descent through the solvent and the horizontally cut planes at 0.03 cm above the growth interface were chosen to see how the silicon is depositing itself along the growth interface and the vertical plane was chosen to show how the silicon is behaving through the solvent. In Figure 3.7 at 0 rpm, it can be seen that concentration contours are quite unsymmetrical. This is due to the three-dimensional flow characteristics of the model. Looking at the horizontal plane cut at 0.5 cm above the growth interface a large jump in silicon concentration exists from 6.5% in the outer contour ring to 10.4% at the center.

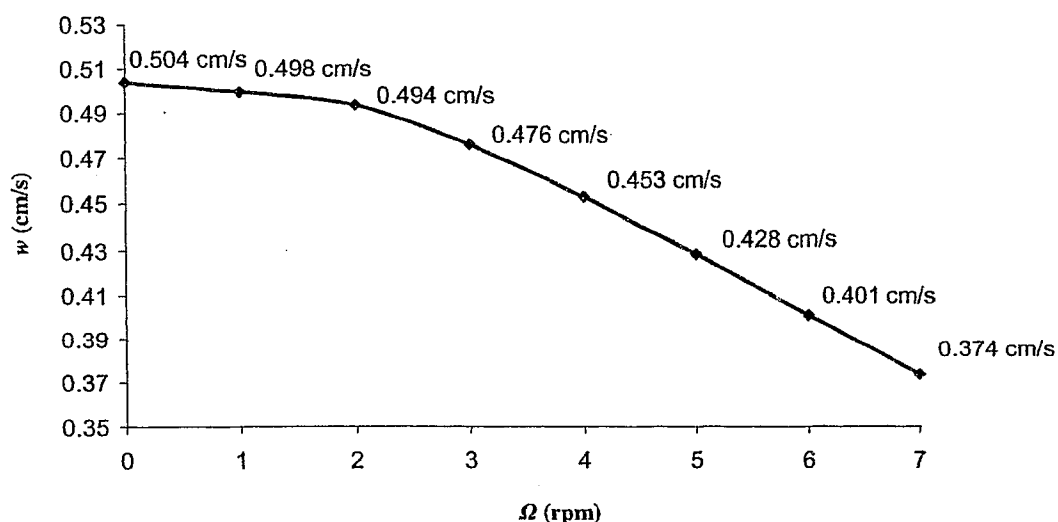


Figure 3.6 Maximum speed as a function of rotation (terrestrial condition).

This can be seen in the three-dimensional graph just below where a sharp peak is shown at the center. At the position of 0.03 cm above the growth interface quite a large variation of concentration is observed which is undesirable for crystal growth where there is 9.1% silicon at the center and 6.5% towards the sides. The shape of how the silicon is depositing itself along the growth interface can be seen in the three-dimensional graph shown just above this plane. Looking at the vertical plane, it is observed that the highest concentration of silicon exists along the central axis of the solvent and closer to the growth interface the silicon concentration lessens. This shows that the silicon is diffusing down through the center of the solution zone then spreading to the sides as it nears the growth interface. This follows the convective flow direction where the hotter less dense liquid is rising at the sides of the sample and the cooler more dense liquid is sinking at the center.

Figure 3.8 shows the concentration distribution for the rotational speed of 2 rpm. Here in the horizontally cut plane at 0.5 cm above the growth interface, a drop down to 7.8% in silicon concentration is observed at the center, which is quite a considerable drop. Also it can be seen that this rotational speed seems to have added some unsymmetrical contours of silicon towards the sides of this plane. Looking at the vertical plane, the silicon distribution has become much more symmetrical and the center concentration has dropped to 9.1% silicon from 10.4%. This is due to the decrease of flow velocity slowing the diffusion of silicon. The horizontal plane at 0.03 cm above the growth interface has become much smoother where the highest concentration of silicon is 6.5% and the concentration close to the sides is 3.9%.

With application of the rotational speed of 5 rpm (Figure 3.9) more symmetry is added along the sides of the lower portion in the solvent. The horizontally cut plane at 0.5 cm above the growth interface has not changed in concentration at the center but the unsymmetrical concentration contours that were seen at 2 rpm have almost disappeared. In the vertical plane this is observed to have added symmetry and it is also seen that one of the concentration contours has been shortened where it is no longer along the growth interface. The horizontal plane cut at 0.03 cm above the growth interface shows almost no change at all except that the diameter of the 6.5% contour has lessened slightly.

At 7 rpm (Figure 3.10) the concentration results appear to be the same as 5 rpm except for the plane located 0.5 cm above the growth interface where almost perfect symmetry can now be observed.

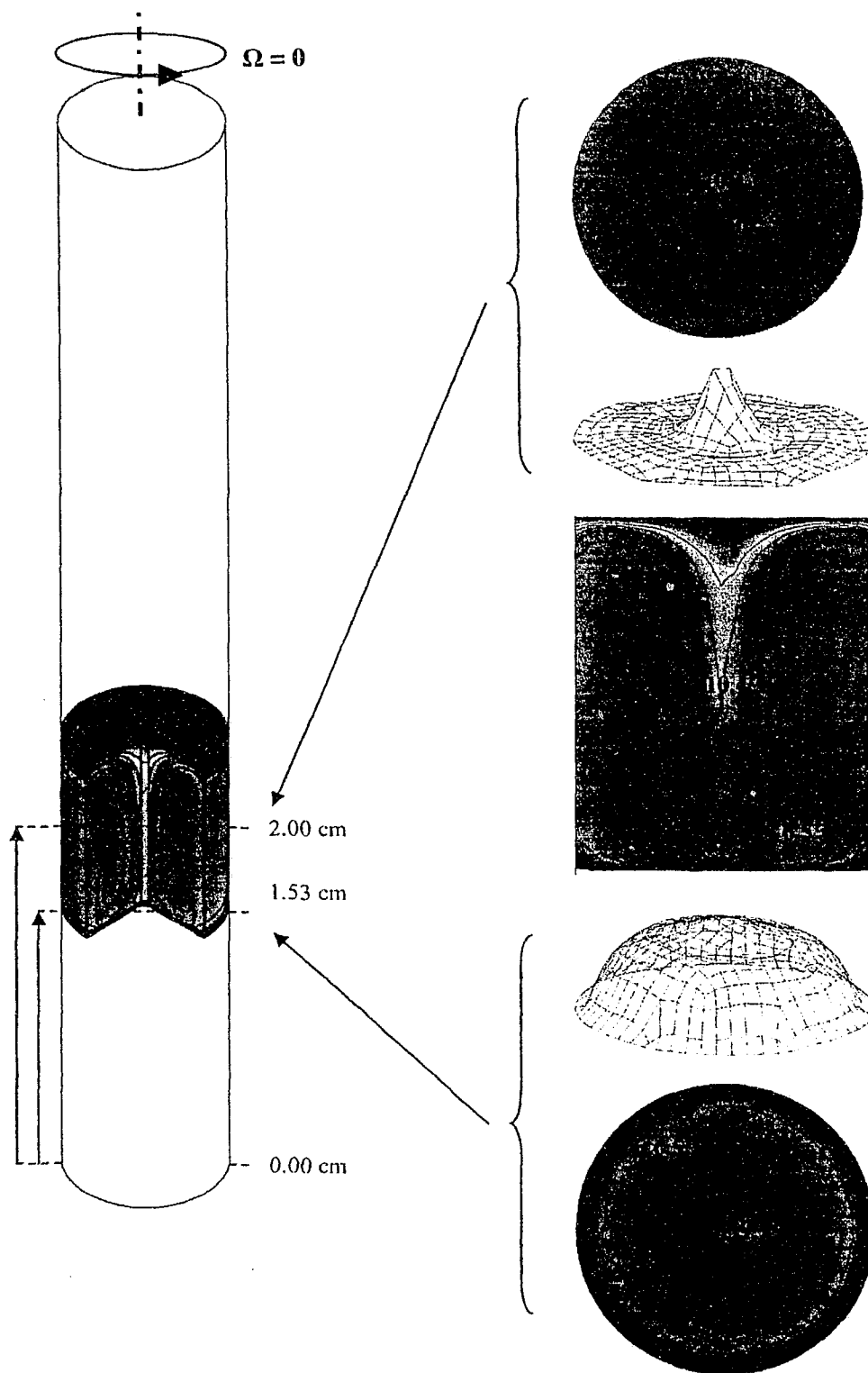


Figure 3.7 Silicon distribution contours for $\Omega = 0$ (terrestrial condition).

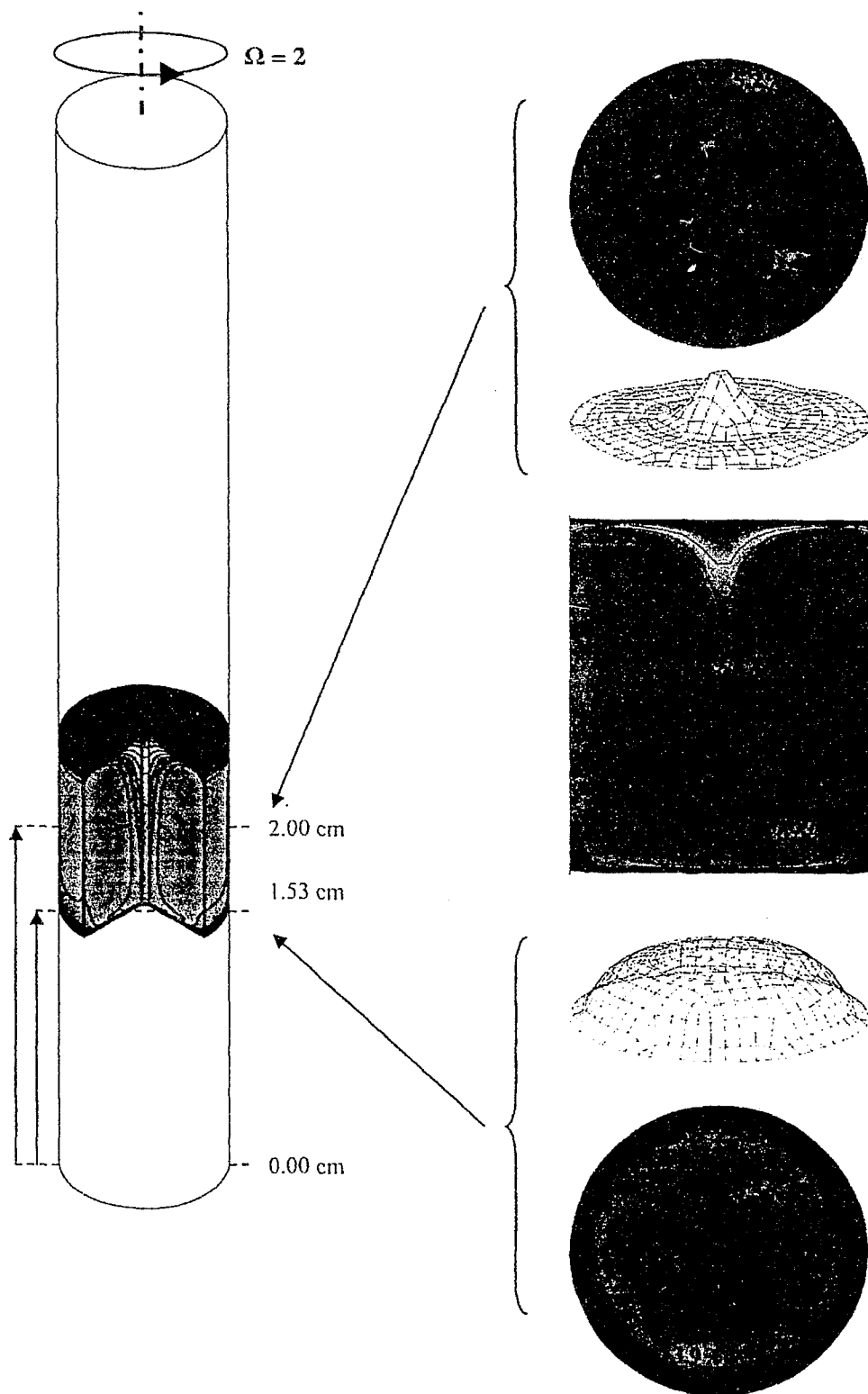


Figure 3.8 Silicon distribution contours for $\Omega = 2$ (terrestrial condition).

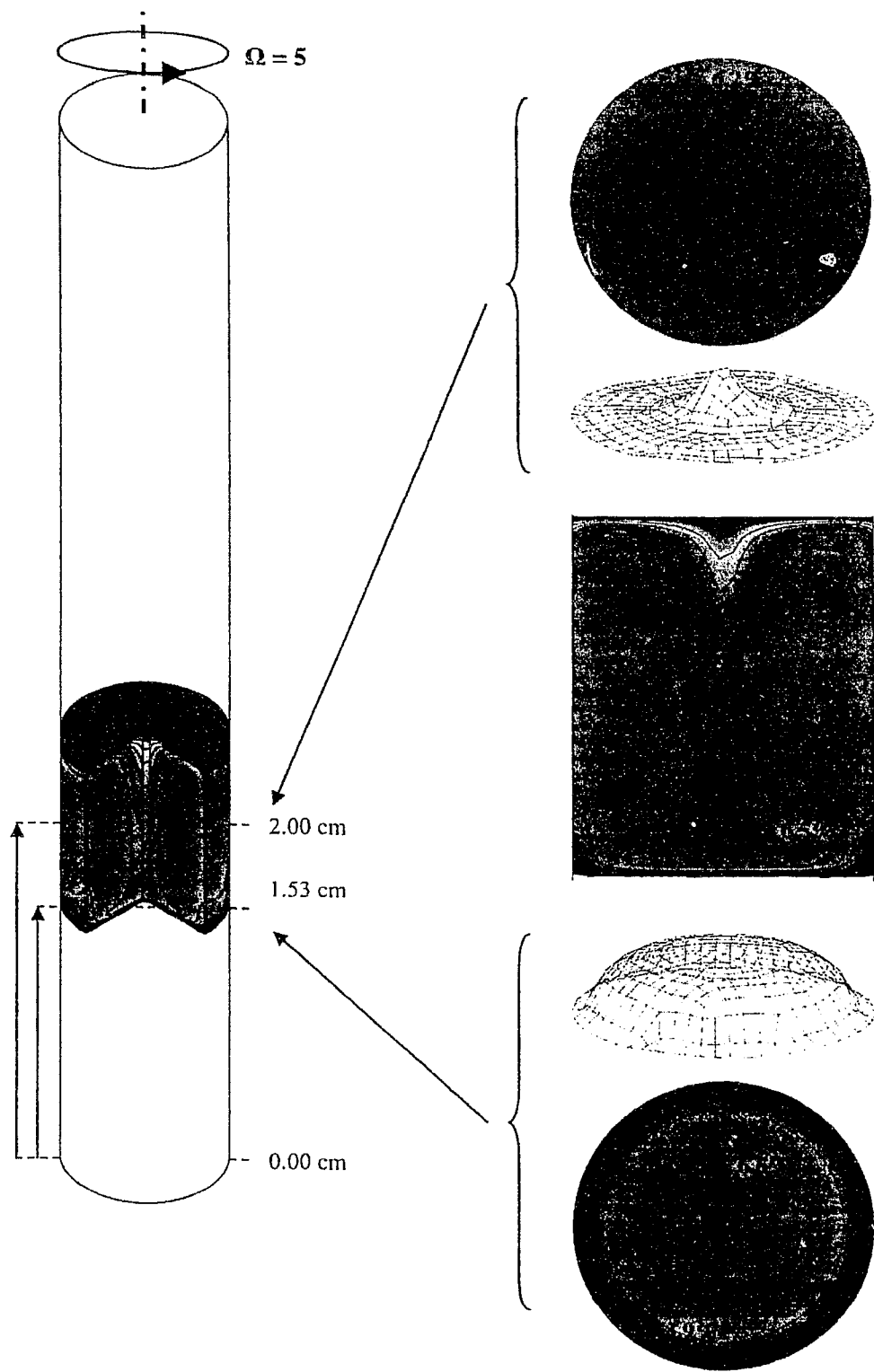


Figure 3.9 Silicon distribution contours for $\Omega = 5$ (terrestrial condition).

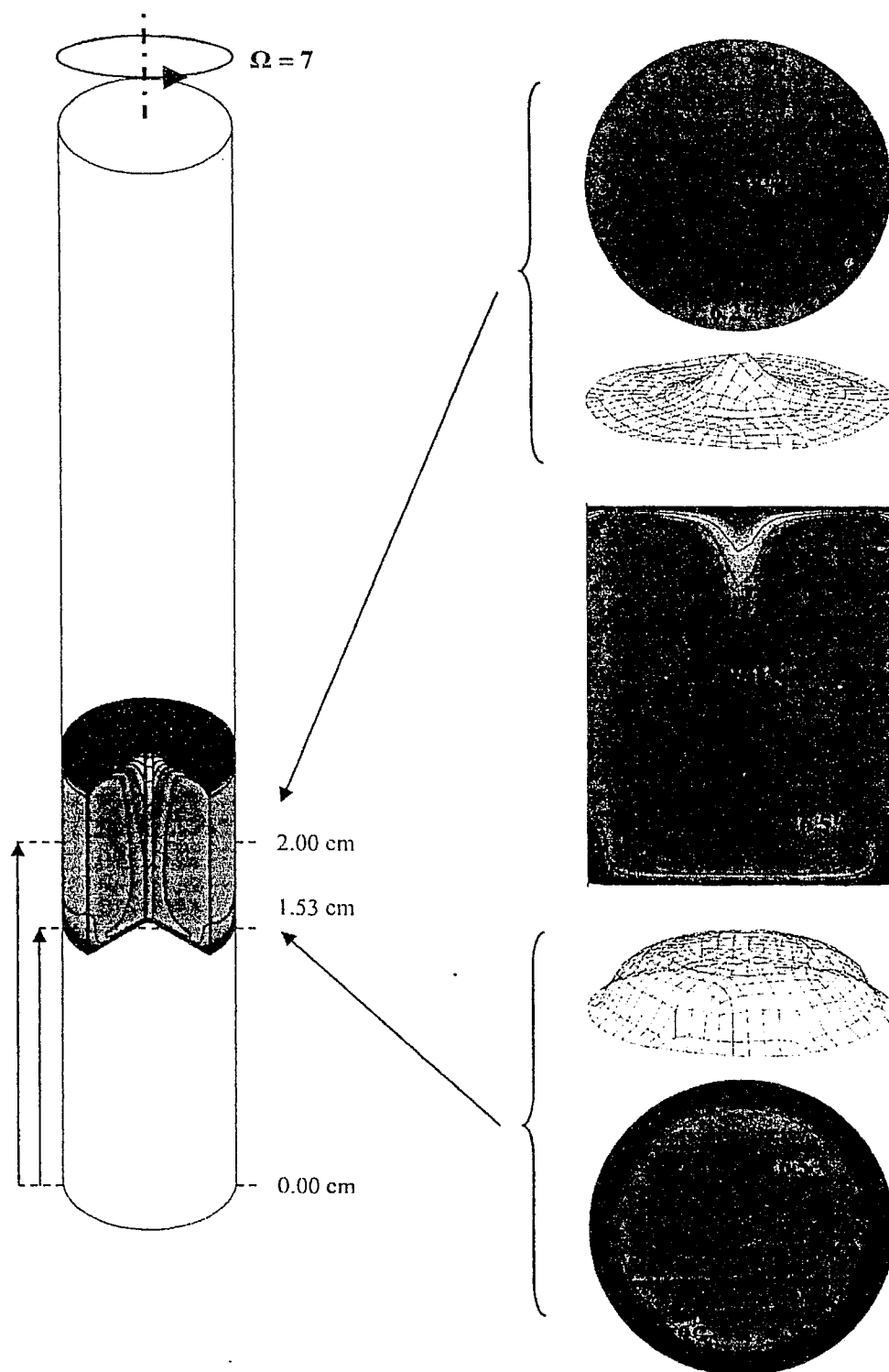


Figure 3.10 Silicon distribution contours for $\Omega = 7$ (terrestrial condition).

The silicon concentration distribution at 0.03 cm above the growth interface for the rotational speeds of 0, 2, 5, 7 and 10 rpm can be seen in Figure 3.11. The additional speed of 10 rpm has been added in this Figure to show that with any rotational speed higher than 7 rpm results being undesirable for crystal growth begin to occur. Numerically results were calculated for 8, 9 rpm but for clarity only 10 rpm was plotted. With the speed of 0 rpm a convex concentration shape is formed along this plane and as the rotational speed is increased this convex shape flattens out and becomes smoother, until 7 rpm is reached. In the case of 10 rpm it can be observed how rotational speeds larger than 7 rpm start to form a concave shape which is undesirable for crystal growth. For crystal growth it is desired to have a smooth and as flat as possible concentration distribution along the growth interface, so from this figure it is seen that for the optimum crystal growth of GeSi in the terrestrial condition, a rotational speed of 7 rpm is desired.

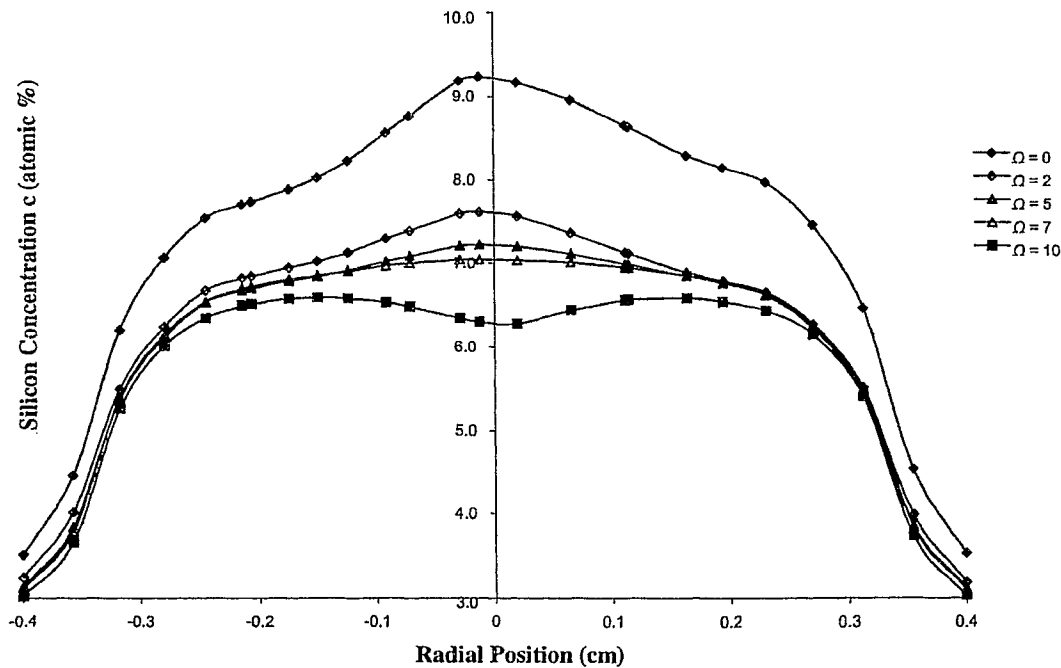


Figure 3.11 Silicon distribution at 0.03 cm above the growth interface (terrestrial condition).

3.2 Microgravity Condition

The microgravity condition simulates the effect of gravity in space where $g = 10^{-4}g_0$. This is studied due to the fact that the effect of buoyancy is weak, and can be used to help better understand the flow phenomenon within the crystal's solution zone as this can be considered a pure diffusion model. In the microgravity condition, the rotational speeds of 0, 2 and 5 rpm were applied to the TSM crystal growth configuration. The velocity contours in the axial-direction for these rotational speeds are shown in Figures 3.12 – 3.14. These Figures show the three-dimensional model, a horizontally cut plane at 0.25 cm below the dissolution interface, two three-dimensional axial velocity surface graphs, a vertical view of the solvent cut in the r-z plane, and a graph of the axial velocity at 0.03 cm above the growth interface. The horizontally cut plane and the r-z plane were chosen for the same reasoning mentioned earlier. Figure 3.12 at 0 rpm in the horizontally cut plane shows very little flow on the order of 10^{-5} cm/s. The vertical plane shows three velocity contour cells, here a velocity of -1.62×10^{-4} cm/s is found at the center of the middle cell and a velocity of 5.26×10^{-5} cm/s is found at the center of the cell located on the right side which is symmetrical to the cell on the left. In the velocity graph below it can be seen that flow at 0.03 cm above the growth interface is almost nonexistent. This can be seen in the three-dimensional graph just above this graph where an almost perfectly flat velocity plane is observed.

The application of 2 rpm to the sample is shown in Figure 3.13. In the horizontally cut plane, the flow shows an increase in velocity with the flow velocity having been reversed at the side and speed contour lines having become fewer. Looking at the vertical plane, it can be noticed that the application of 2 rpm has created breaking of the three flow cells seen at 0 rpm into six flow cells within the solvent region. This added rotation has increased the speed throughout the system. The speed at the center of the lower middle cell is increased to -4.46×10^{-4} cm/s and the speed at the center of the cell located at the lower right side is increased to 1.89×10^{-4} cm/s. With the formation of the three new flow cells to the system, the three strong ones have been pushed closer to the growth interface and the three weaker ones have taken form in the top quarter of the solvent close to the dissolution region. Since the three strong flow cells have been pushed closer to the growth

interface, a slight increase in flow velocity to $\pm 5 \times 10^{-5}$ cm/s is observed in the velocity graph at 0.03cm above the growth interface.

At 5 rpm, shown in Figure 3.14, a much more complex formation of velocity flow cells are formed in the solvent where there is a total of seven cells. In the horizontal plane it can be seen that the flow has become quite abrupt compared to that of 2 rpm where there is a much larger variation in flow from -1.09×10^{-4} cm/s to 1.76×10^{-4} cm/s. The speeds in the vertical plane are further increased to -6.82×10^{-4} cm/s at the center of the middle flow cell and to 6.05×10^{-4} cm/s at the center of the cell located at the lower right. This vertical plane shows further compression of the flow cells towards the growth interface which gives rise to the higher axial velocities graphed 0.03 cm above the growth interface. The velocity in the graph varies from -1.5×10^{-4} cm/s to 2.5×10^{-4} cm/s. For crystal growth this is undesirable, as a steady constant velocity preferably close to zero is best for growth quality.

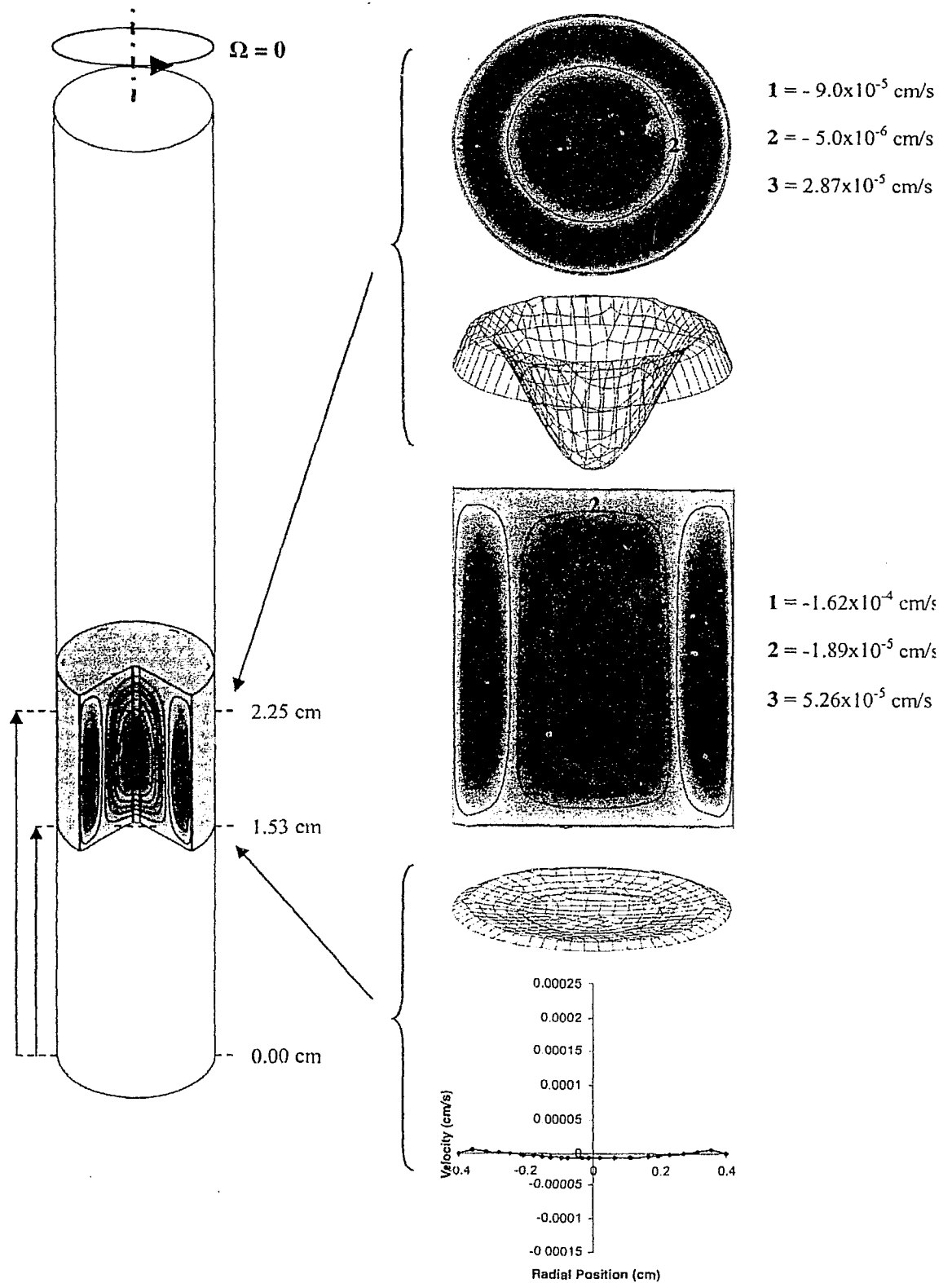


Figure 3.12 Axial direction velocity contours for $\Omega = 0$ (microgravity condition).

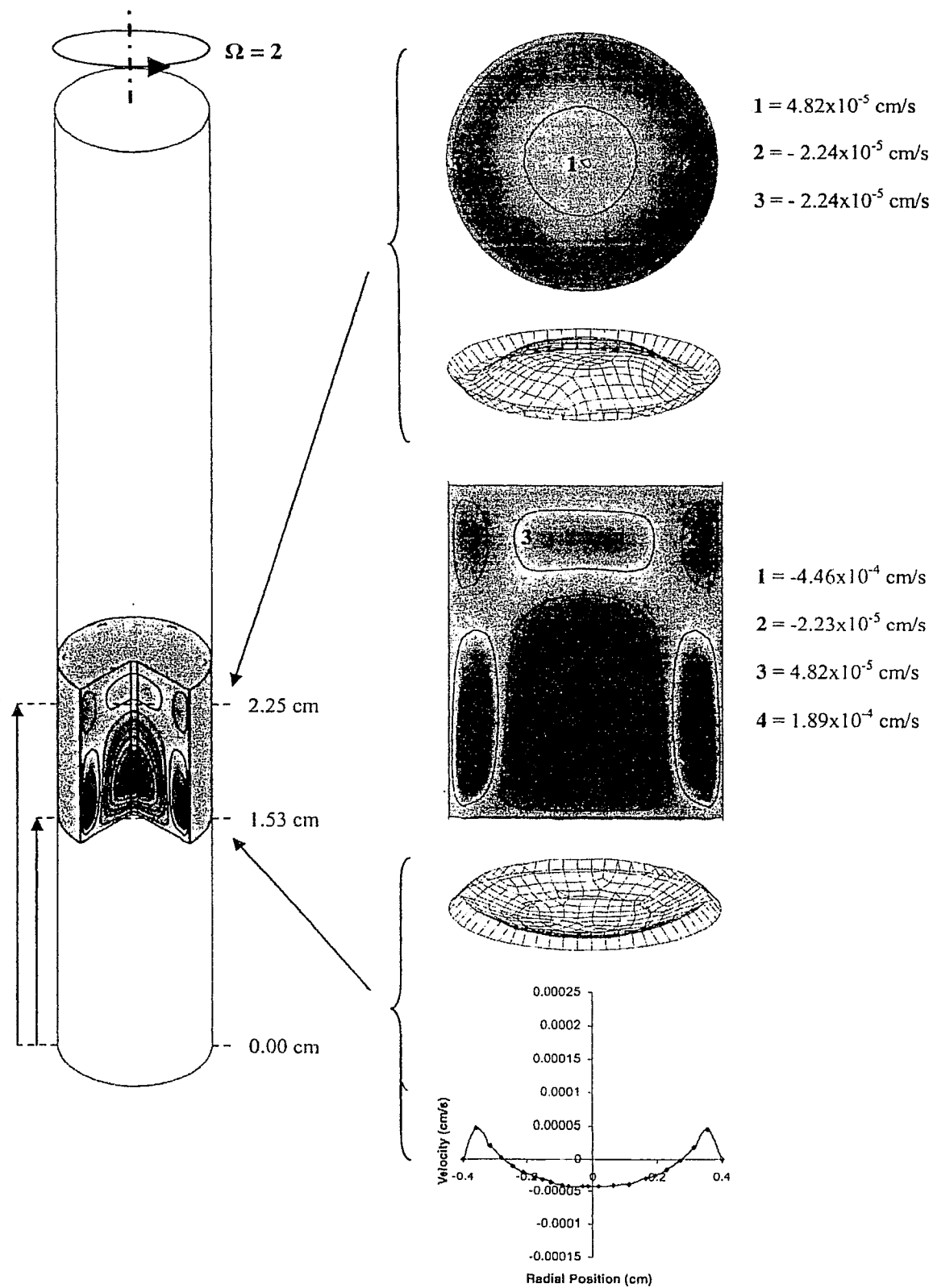


Figure 3.13 Axial direction velocity contours for $\Omega = 2$ (microgravity condition).

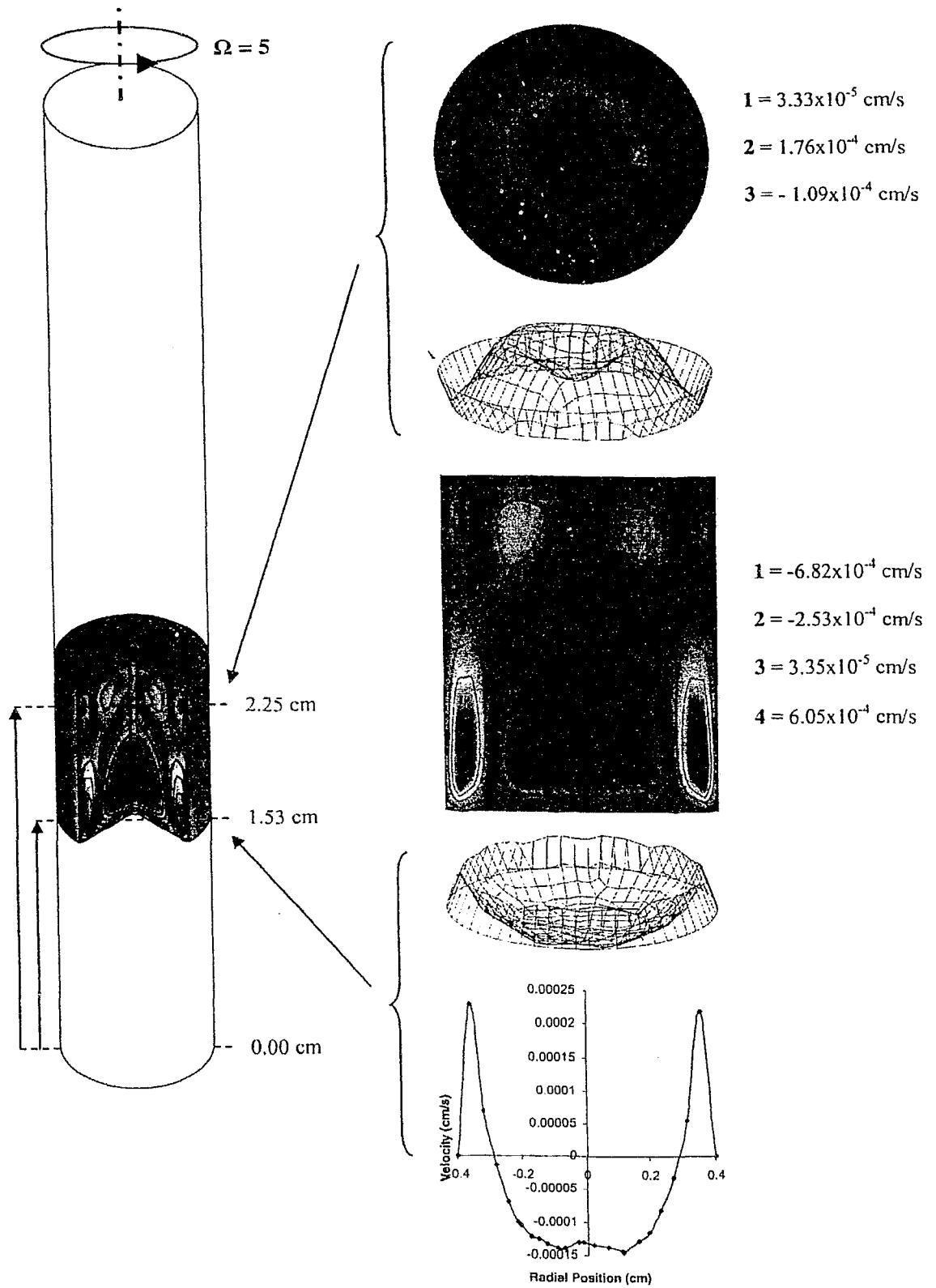


Figure 3.14 Axial direction velocity contours for $\Omega = 5$ (microgravity condition).

Figure 3.15 shows the maximum speed of flow as a function of rotation in the solvent for the cases of 0, 2 and 5 rpm. The maximum speed of flow with the application of crucible rotation increases from 1.68×10^{-4} cm/s at 0 rpm to 1.89×10^{-3} cm/s at 5 rpm. It is seen that in the microgravity case, the application of rotation is not suitable in helping achieve uniform silicon deposition along the growth interface as it does not help in suppressing the flow, but instead increases the speed of the flow throughout the solution, complicates the flow and also gives unsteady flow conditions along the growth interface.

Figures 3.16 – 3.18 display the concentration contours obtained from the microgravity cases of 0, 2 and 5 rpm. Looking at Figure 3.16, it can be seen that with no rotation, smooth and almost perfectly straight concentration contours are formed being evenly spaced throughout the solvent. In Figure 3.17, where a rotational speed of 2 rpm has been added, a slight dip in the concentration contours appear due to the added velocity and centripetal force to the system. This concentration contour deformation further increases with the rotational speed of 5 rpm as shown in Figure 3.18. From the rotational speeds studied in the microgravity condition the most desirable case for crystal growth is that of no rotation as this provides the most uniform and flat concentration distribution along the growth interface. The concentration distribution located at 0.03 cm above the growth interface is presented in Figure 3.19. Here it can easily be seen that the concentration distribution is the smoothest and most uniform with the application of 0 rpm and the most disturbed with the rotational speed of 5 rpm.

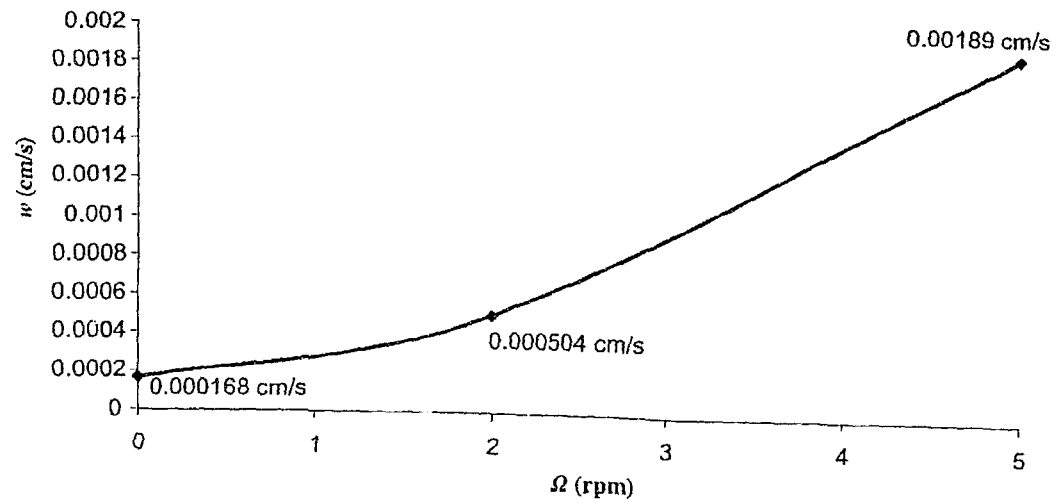


Figure 3.15 Maximum speed as a function of rotation (microgravity condition).

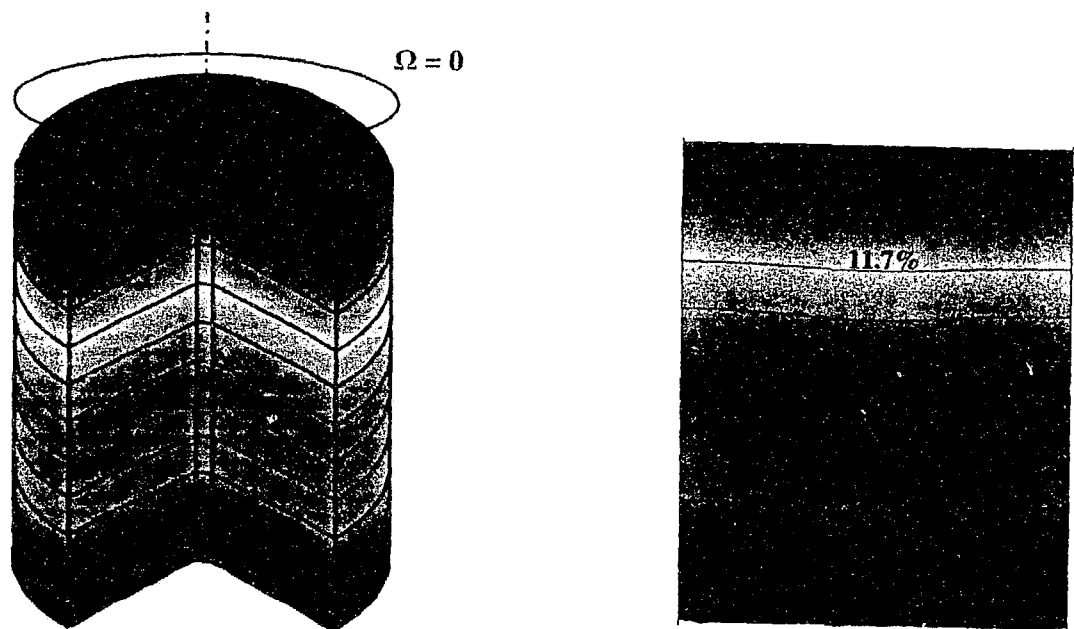


Figure 3.16 Silicon distribution contours for $\Omega = 0$ (microgravity condition).

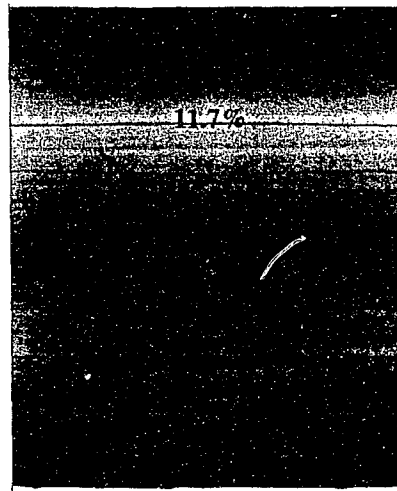
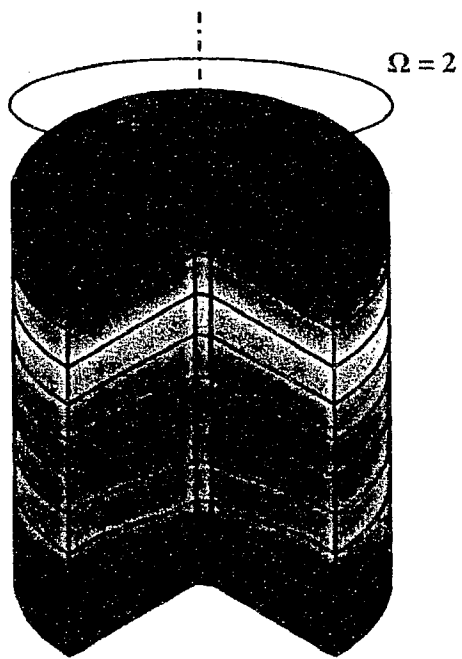


Figure 3.17 Silicon distribution contours for $\Omega = 2$ (microgravity condition).

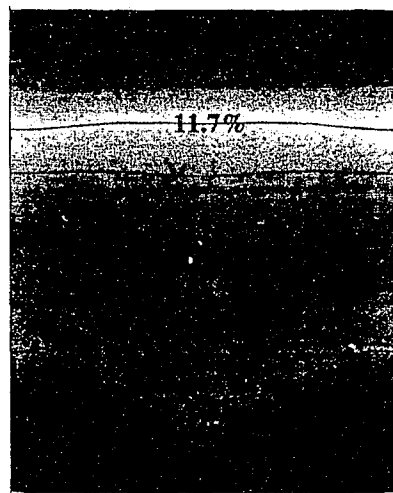
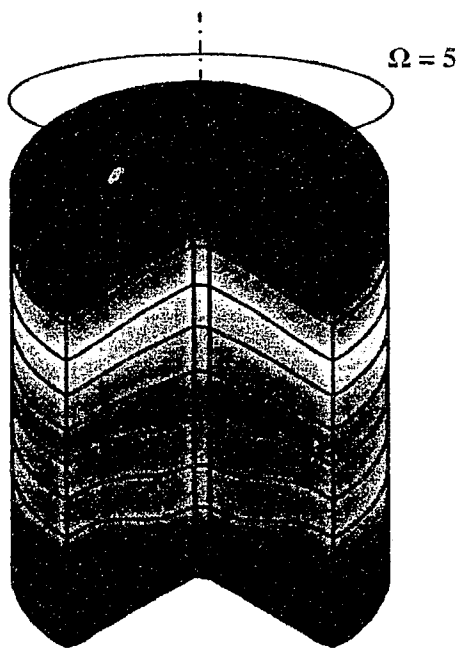


Figure 3.18 Silicon distribution contours for $\Omega = 5$ (microgravity condition).

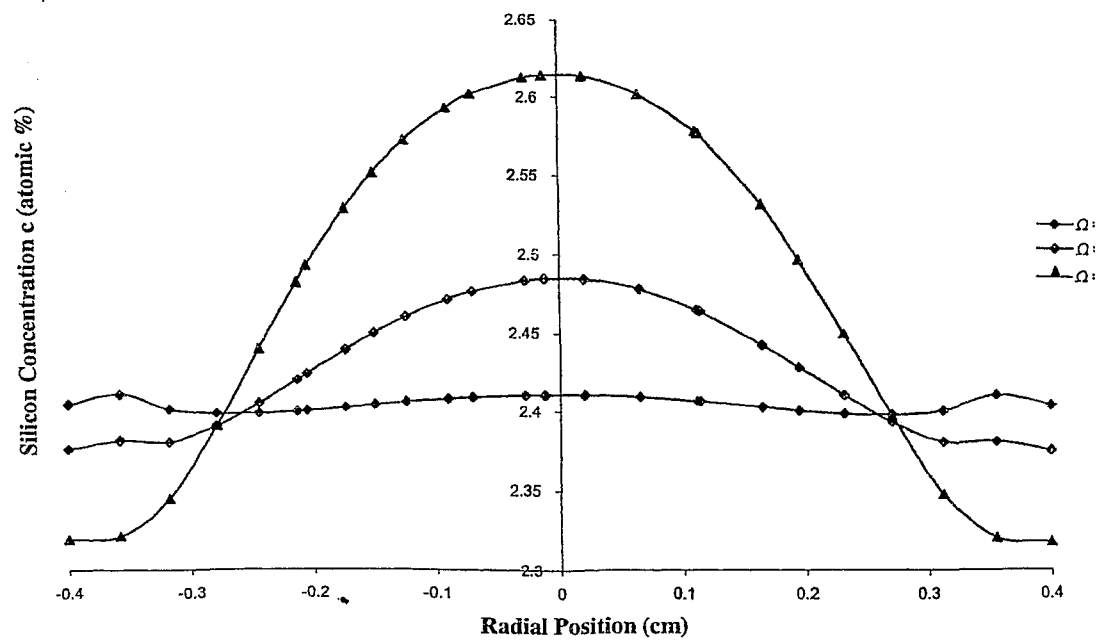


Figure 3.19 Silicon distribution at 0.03 cm above the growth interface (microgravity condition).

CHAPTER 4

Non-Uniform Heating Condition

4.0 Introduction

This chapter presents the results obtained with the non-uniform heater profile applied to the TSM model under different rotational speeds. The non-uniform heating condition has been studied due to the fact that in reality there is no such thing as a perfectly uniform heater profile. Every heater profile lags whether it is noticeable or not. Here it will be observed if rotation can help reduce the effect of heater lag on the growing crystal. The non-uniform heater profile applied was obtained by adding a polynomial temperature variation in the x and y directions to the temperature profile applied in the uniform heating condition. This allows the temperature to change gradually around the circumference of the sample. Figure 4.1 shows how the temperature profile was varied around the sample with zero being the original temperature profile unchanged. Figure 4.2 shows the non-uniform temperature distribution around the model as a result of the temperature variation. This chapter is broken down into two sections; the first section discusses the results obtained in the terrestrial condition and the second the results obtained in the microgravity condition.

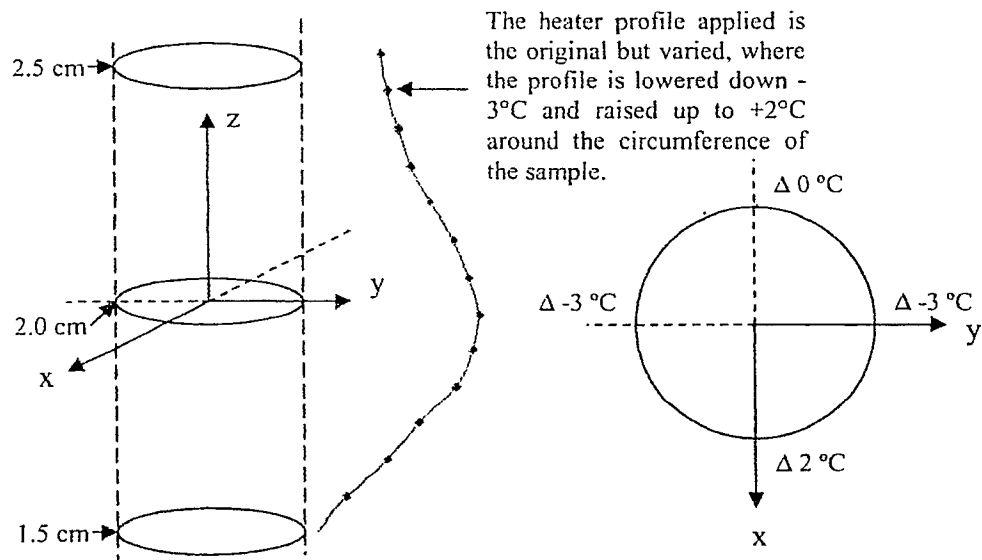


Figure 4.1 Temperature profile variation around model.

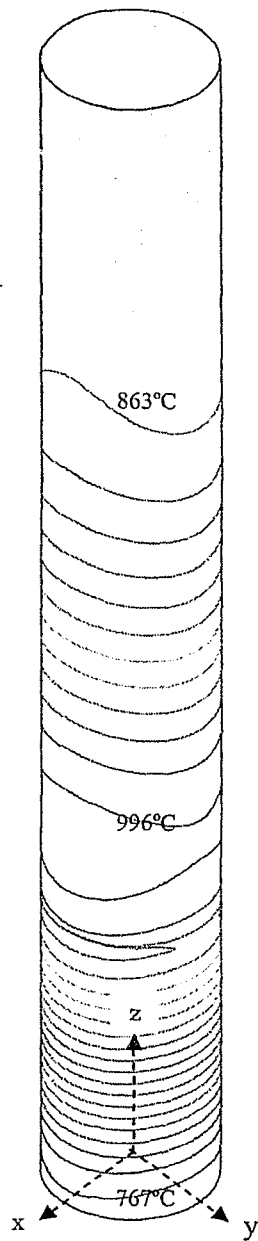


Figure 4.2 Non-uniform temperature heater thermal profile applied to TSM model (contour lines in increments of 10.8°C).

4.1 Terrestrial Condition

In the terrestrial condition, as was done in chapter 3, the rotational speeds of 0, 2, 5, and 7 rpm were applied to the crystal growth model. The results of the axial velocity contours are shown in Figures 4.3 – 4.6. In these figures, the three-dimensional model is accompanied by two planes cut horizontally and vertically showing the axial velocity contours, two surface graphs displaying the axial velocity variation and an axial velocity variation plot. The horizontally cut plane is cut 0.25 cm below the dissolution interface where the flow will be relatively unsteady due to the silicon diffusion from the dissolution interface and the vertically cut plane is cut along the r-z plane with unsymmetrical heating. The surface graphs, graph the axial flow at the horizontally cut plane and at 0.03 cm above the growth interface and the velocity variation plot, is at 0.03 cm above the growth interface as well.

Examining the rotational speed of 0 rpm in Figure 4.3, it can be seen from the three-dimensional view how the non-uniform heating has affected the flow by disrupting the shape of the flow cells that were present in chapter 3. The horizontal view shows three flow cells which appear to have a line of symmetry. This line of symmetry is in agreement with the heater profile applied, see Figure 4.1. In comparing this horizontal plane to Figure 4.1 there should be a higher velocity along the walls of higher temperature. This would be where the 2 degree increase occurs where the velocity is 0.454 cm/s. Where there is no increase, a velocity of 0.249 cm/s is obtained. So the line of symmetry, when observing figure 4.1, is located along the x-axis passing through the origin of the z plane. Just as in the uniform heating case a negative velocity has occurred at the center of the plane indicating that the direction of the flow is downwards at the center. Below the horizontal plane, the plane's axial velocity is depicted in a surface graph, this gives a three-dimensional perspective of how the velocity is varying along this plane. Looking at the vertically cut plane, it can be seen that the symmetry of the flow cells that was present in chapter 3 has been destroyed. In the left contour cell there is an axial velocity of 0.454 cm/s and in the right contour cell an axial velocity of 0.249 cm/s, again indicating that highest temperatures are on the left side where the velocity is the greatest. At the center, the flow is directed downwards having a max velocity of -0.469 cm/s. The axial velocity plot shows a large variation in flow velocity 0.03 cm

above the growth interface ranging from 0.033 cm/s to -0.087 cm/s. The surface graph above the velocity plot indicates that this plane is quite symmetrical all around with a dip in the center where the velocity is moving downwards.

At 2 rpm (Figure 4.4) observing the horizontal velocity contour plane, it can be seen that this line of symmetry that existed at 0 rpm has vanished. The left flow cell still has the highest velocity being 0.456 cm/s which has increased by 0.002 cm/s and the right flow cell has a velocity of 0.257 cm/s having increased 0.08 cm/s. The flow at the center has slowed down to -0.234 cm/s which has decreased by 0.03 cm/s. Looking at the vertical velocity contour plane the flow cells have kept the same shape. The velocity has increased in both the left and right flow cells to 0.456 cm/s and to 0.257 cm/s, giving an increase of 0.002 cm/s and 0.008 cm/s respectively. The center flow cell velocity has been lessened to -0.442 cm/s, having been decreased by 0.027 cm/s. At the bottom of Figure 4.4 it can be seen that from the axial velocity plot, the maximum negative velocity has been decreased to 0.066 cm/s, a 0.021 cm/s decrease. This decrease in speed is beneficial for the crystal growth process which will help the concentration to be more evenly distributed along the growth interface.

With the application of 5 rpm (Figure 4.5) the horizontal contour plane shows that the flow cells have been even further disrupted, with increased dissymmetry. The maximum speed in the left flow cell has decreased to 0.431 cm/s and in the right flow cell to 0.248 cm/s giving a decrease of 0.025 cm/s and 0.009 cm/s respectively. The speed at the center has been increased to -0.277 cm/s having an increase of 0.045 cm/s. Looking at the vertical plane, the flow cells have become more symmetrical and the flow cell at the center has spread its contours out. This explains the increase in velocity in the center flow cell of the horizontal plane. The velocity in the left flow cell of the vertical plane has decreased to 0.431 cm/s and the velocity in the right flow cell has increased to 0.343 cm/s giving a decrease of 0.025 cm/s and an increase of 0.086 cm/s respectively. The increase in velocity in the right cell has improved the symmetry of flow cells and seems to have started pushing the center flow cell more towards the center of the system. The maximum negative velocity has been decreased to -0.366 cm/s giving a 0.086 cm/s decrease. The velocity variation at 0.03 cm above the growth interface has been lessened having a

maximum positive velocity of 0.0264 cm/s and a maximum negative velocity of – 0.0415 cm/s. This decrease in velocity variation further assists in production of a more uniform crystal.

At 7 rpm shown in Figure 4.6, the horizontal plane shows no change in shape of the flow cells; the only change shown is some of the contours have stretched to cover a larger area. The velocity in the left flow cell of the horizontal plane has decreased to 0.411 cm/s and has increased in the right flow cell to 0.253 cm/s giving a decrease of 0.02 cm/s and an increase of 0.005 cm/s respectively. The center flow cell has increased its velocity to – 0.301 cm/s, having a 0.034 cm/s increase. The vertical plane has become almost symmetric where the left flow cell has decreased to a velocity of 0.411 cm/s and the right flow cell has decreased to 0.332 cm/s giving a change of 0.02 cm/s and 0.011 cm/s respectively. The center flow cell has also lowered its velocity to – 0.301 cm/s giving a 0.064 cm/s decrease. At 0.03 cm above the inflow, the maximum positive and negative velocities have become 0.0284 cm/s and - 0.0254 cm/s. The maximum positive velocity has slightly increased by 0.002 cm/s and the maximum negative velocity has decreased by 0.0161 cm/s. This change in velocity has even further reduced the magnitude of velocity variation being best for crystal growth out of the rotational speeds observed.

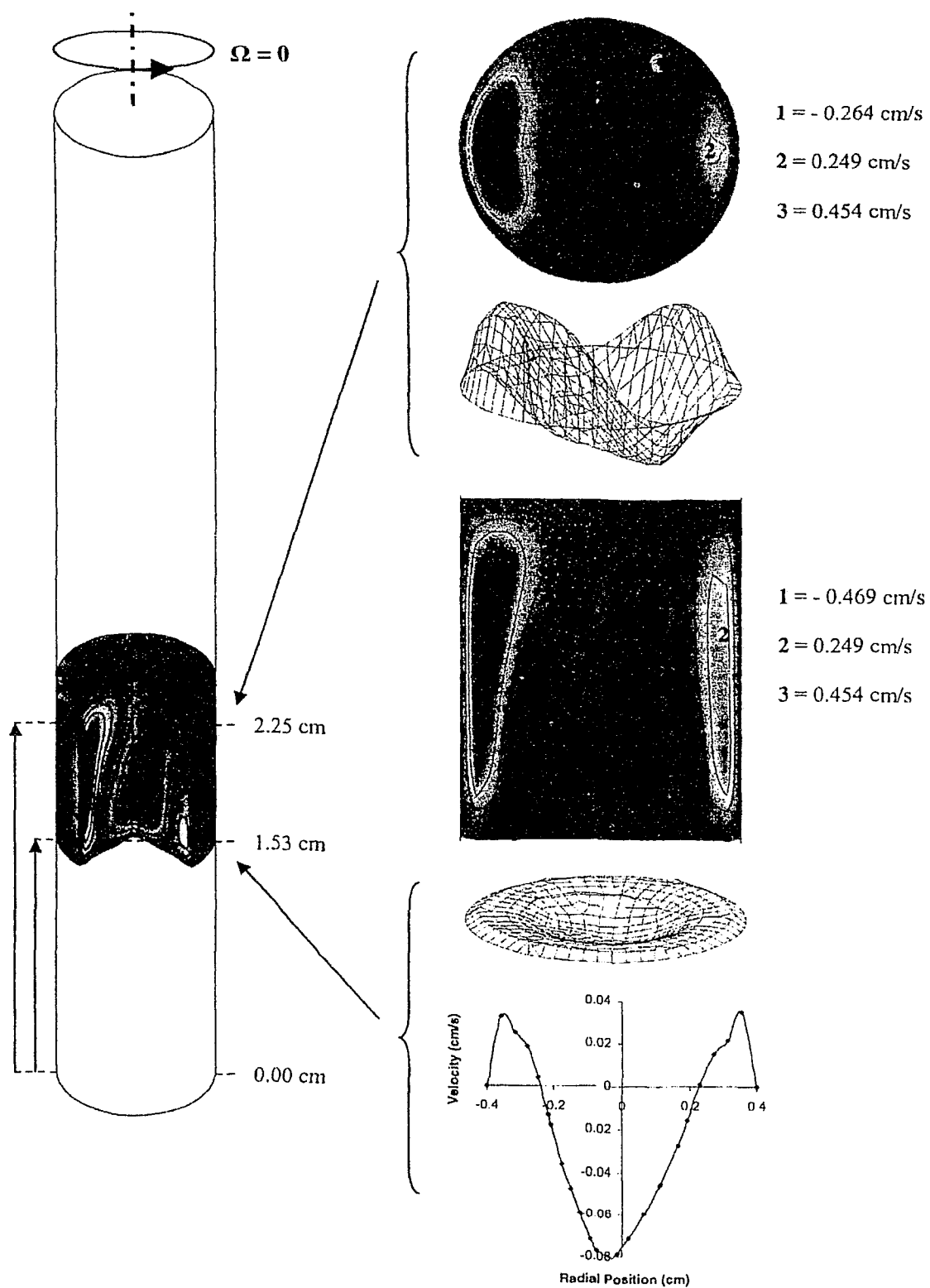


Figure 4.3 Axial direction velocity contours for $\Omega = 0$ (terrestrial condition).

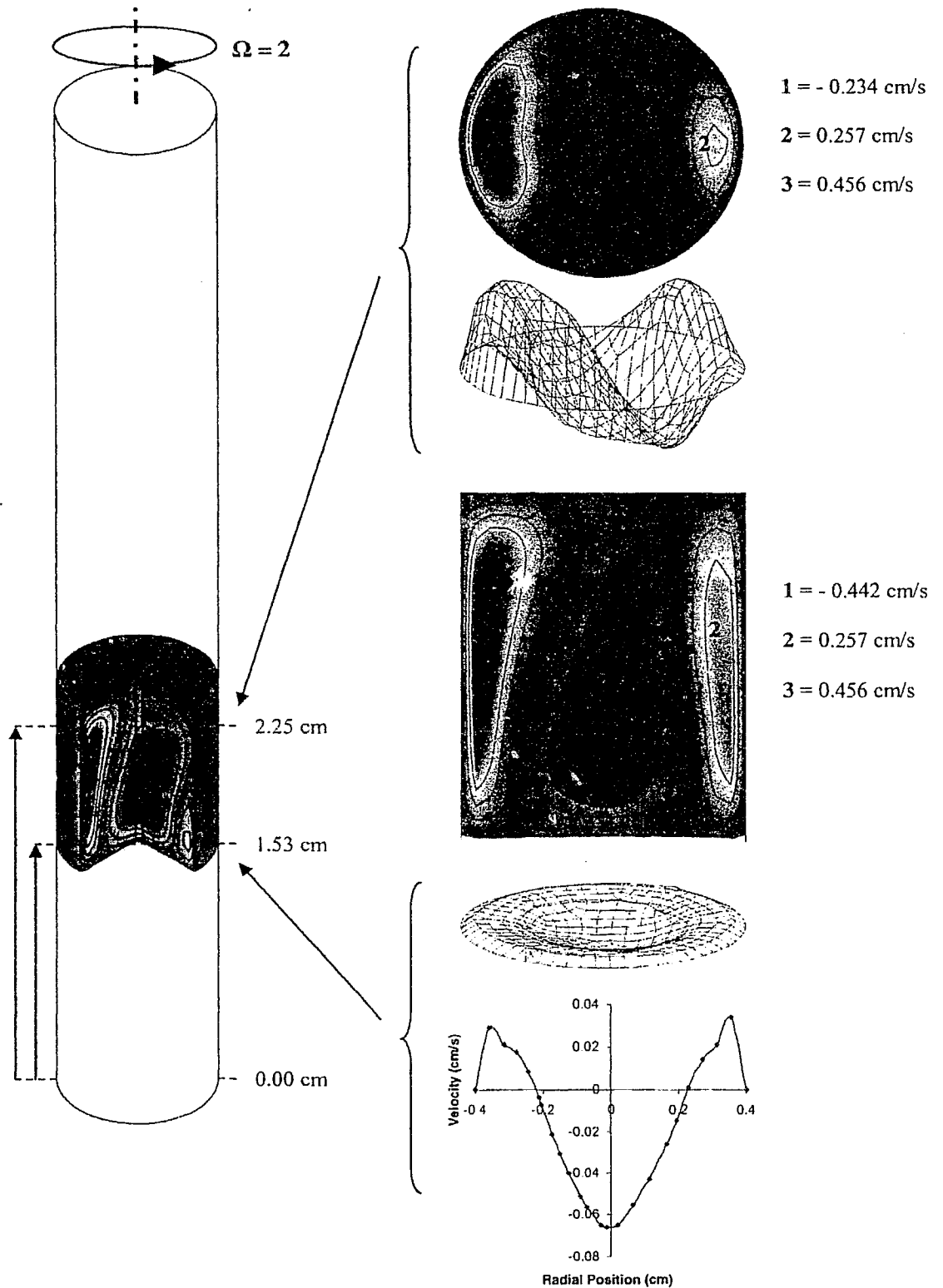


Figure 4.4 Axial direction velocity contours for $\Omega = 2$ (terrestrial condition).

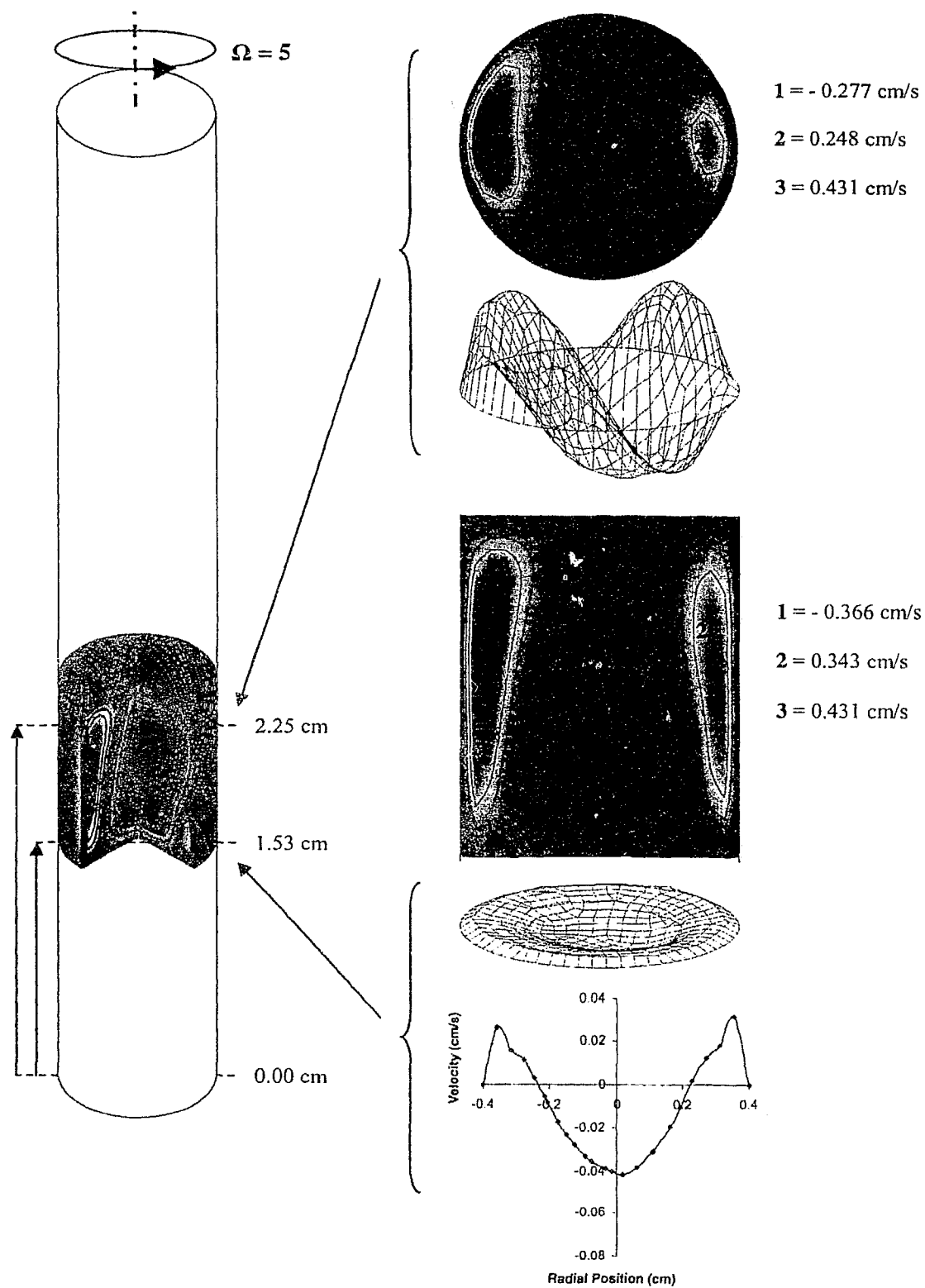


Figure 4.5 Axial direction velocity contours for $\Omega = 5$ (terrestrial condition).

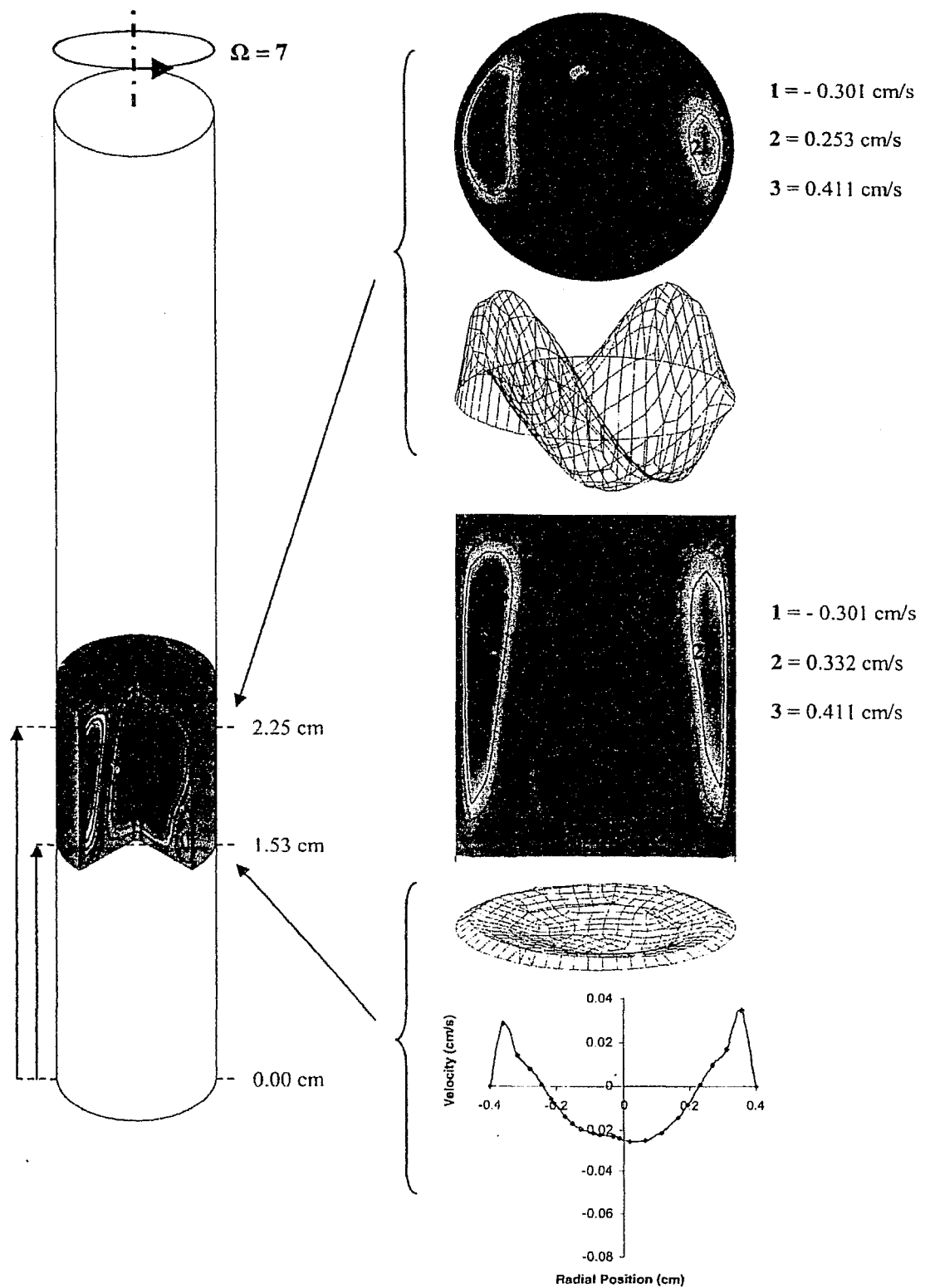


Figure 4.6 Axial direction velocity contours for $\Omega = 7$ (terrestrial condition).

Looking at the graph in Figure 4.7, the maximum speed of flow is graphed as a function of the rotational speeds ranging from 0 -7 rpm. Some unsteadiness can be seen ranging from 0 rpm to 3 rpm where the speed is decreasing non-linearly. From 3 rpm to 7 rpm the maximum speed starts to decrease linearly, indicating that the rotation seems to have gained control over the unsteady speed throughout the system. As mentioned in chapter 3, since the maximum speed is decreasing with increasing rotational speed, the application of rotation is successful in helping suppress the convective flow within the system.

The concentration contours throughout the solvent are shown for the rotational speeds of 0, 2, 5, and 7 rpm in Figures 4.8 – 4.11. These Figures include a three-dimensional model accompanied by two horizontally cut planes, one vertically cut plane and two horizontal three-dimensional surface plots. The horizontally cut planes are located mid-way in the solvent at 0.5 cm above the growth interface and at 0.03 cm above the growth interface. The vertically cut plane of the solvent is cut along the plane of unsymmetrical heating and the two surface plots are the same two planes of the horizontal cut depicting a three-dimensional view of the concentration distribution.

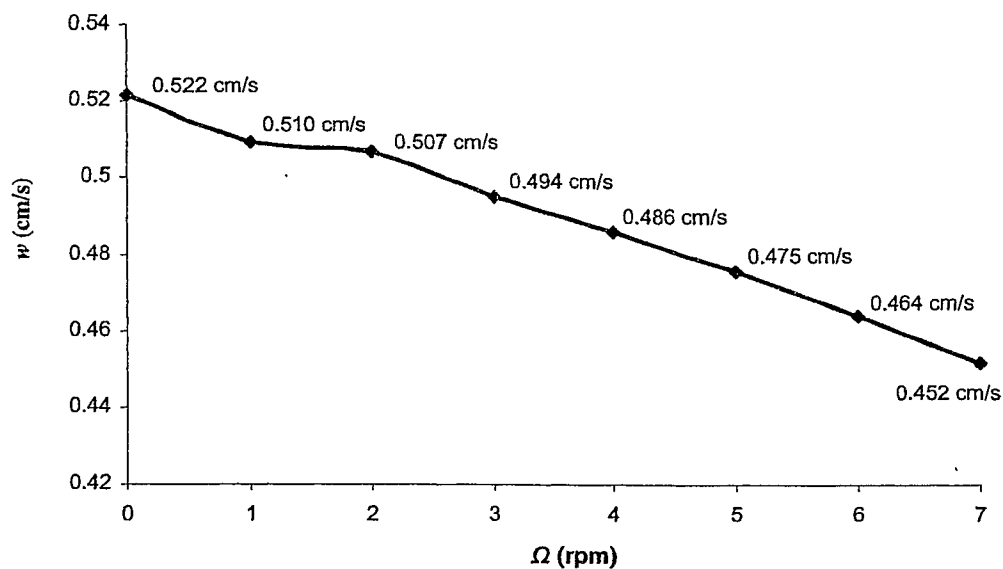


Figure 4.7 Maximum speed as a function of rotation (terrestrial condition).

In Figure 4.8 with 0 rpm being applied, it can be seen that from the three-dimensional model that the concentration distribution has been disrupted significantly due to the non-uniform heating. Looking at the mid-way horizontally cut plane, it is seen that the nice uniformity observed earlier in the uniform heating case is no longer present, but a line of symmetry does exist similar to that which was mentioned in the velocity distribution of the non-uniform heating at 0 rpm. Here the concentration varies between 7.9% and 5.3%. Below, the surface graph depicts the uneven distribution of the silicon in this plane. Looking at the vertically cut plane, it is seen that the silicon diffusion that was occurring at the center in the uniform heating case has now been pushed over to the right and no symmetry can be seen. Again the silicon concentration lessens as it reaches the bottom of the solvent. This indicates that the silicon is diffusing downwards. The horizontally cut plane at 0.03 cm above the growth interface shows a silicon variation of 6.6% at the center to 4% at the sides. It can also be seen that the inner most concentration contour is unsymmetrical.

At 2 rpm shown in Figure 4.9, the three-dimensional model contours have changed shape but are still very disturbed. In analyzing the mid-way horizontally cut plane, it is observed that all symmetry that was present at 0 rpm has been destroyed and the silicon concentration variation has changed to 9.2% - 6.6%. The vertically cut plane shows that a larger amount of silicon has begun to diffuse down towards the growth interface. This increase in concentration is shown to take effect in the horizontal plane at 0.03 cm above the growth interface where the inner most contour that was present before has spread out, increasing the concentration towards the side of the growth interface. It can also be observed that this contour has now become symmetrical which is what is required for better crystal growth conditions.

Figure 4.10 shows the concentration distribution for 5 rpm. The mid-way horizontally cut plane has become less disturbed with the same silicon concentration variation to that of the 2 rpm case. Looking at the vertically cut plane, it can be seen that where the largest concentration of silicon is diffusing from the top, it has shifted towards the center and that the concentration reaching the bottom of the solvent has further increased to 9.2%. The horizontally cut plane at the bottom has introduced a new contour line with an increased concentration of 7.9%. This new contour is not quite symmetrical which is undesirable for the growth of the crystal.

At 7 rpm shown in Figure 4.11, the mid-way horizontal plane has become even steadier in terms of the silicon distribution to that of 5 rpm and the silicon concentrations remain the same as that of the 2 and 5 rpm contours. Looking at the vertically cut plane it can be seen that where this largest concentration of silicon is diffusing downwards, it has been positioned almost perfectly in the center and the contour distribution has become more symmetrical. The horizontal plane just above the growth interface shows the same contours to that of the 5 rpm case but with middle contour being less symmetric to that at 5 rpm.

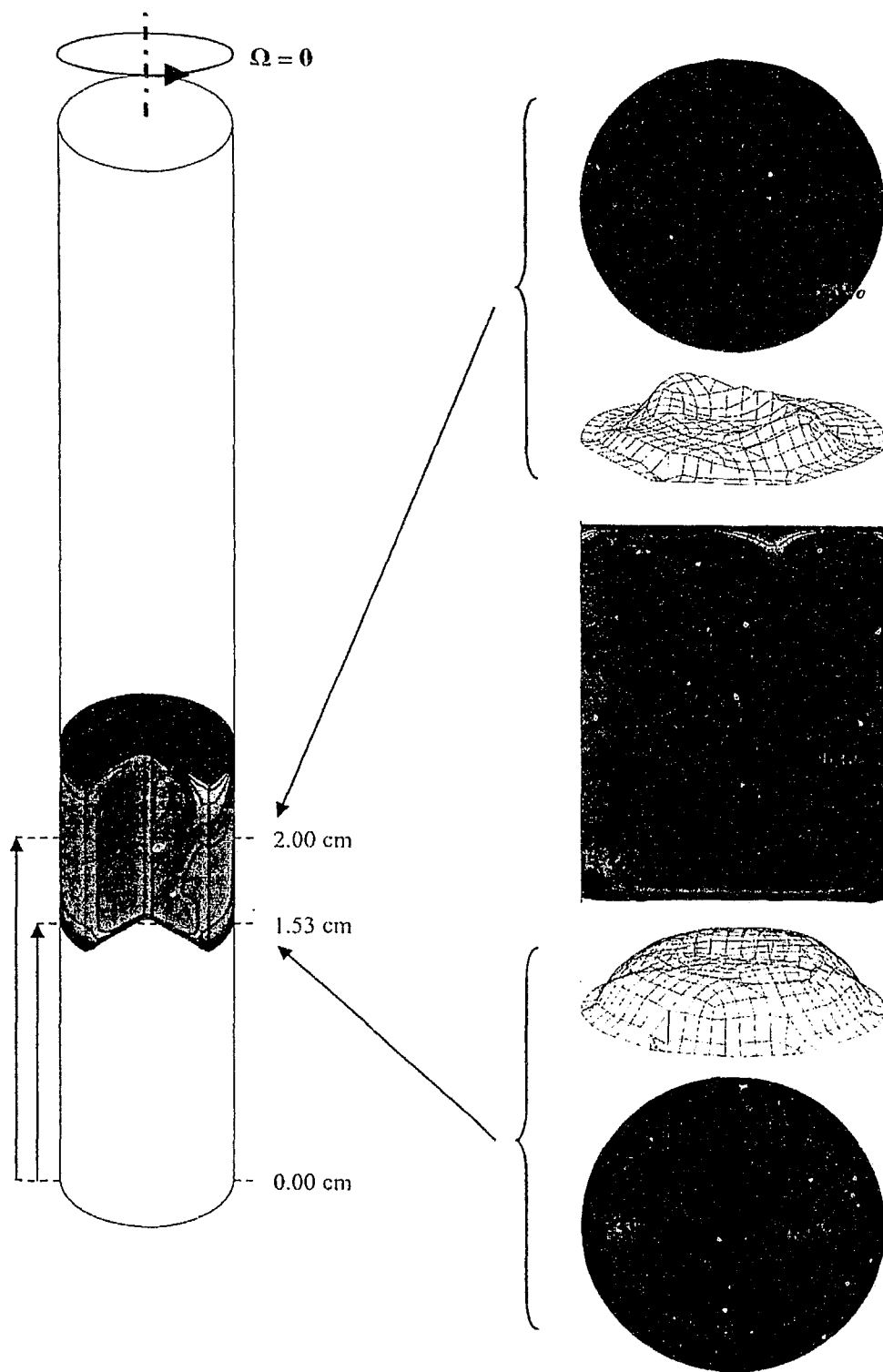


Figure 4.8 Silicon distribution contours for $\Omega = 0$ (terrestrial condition).

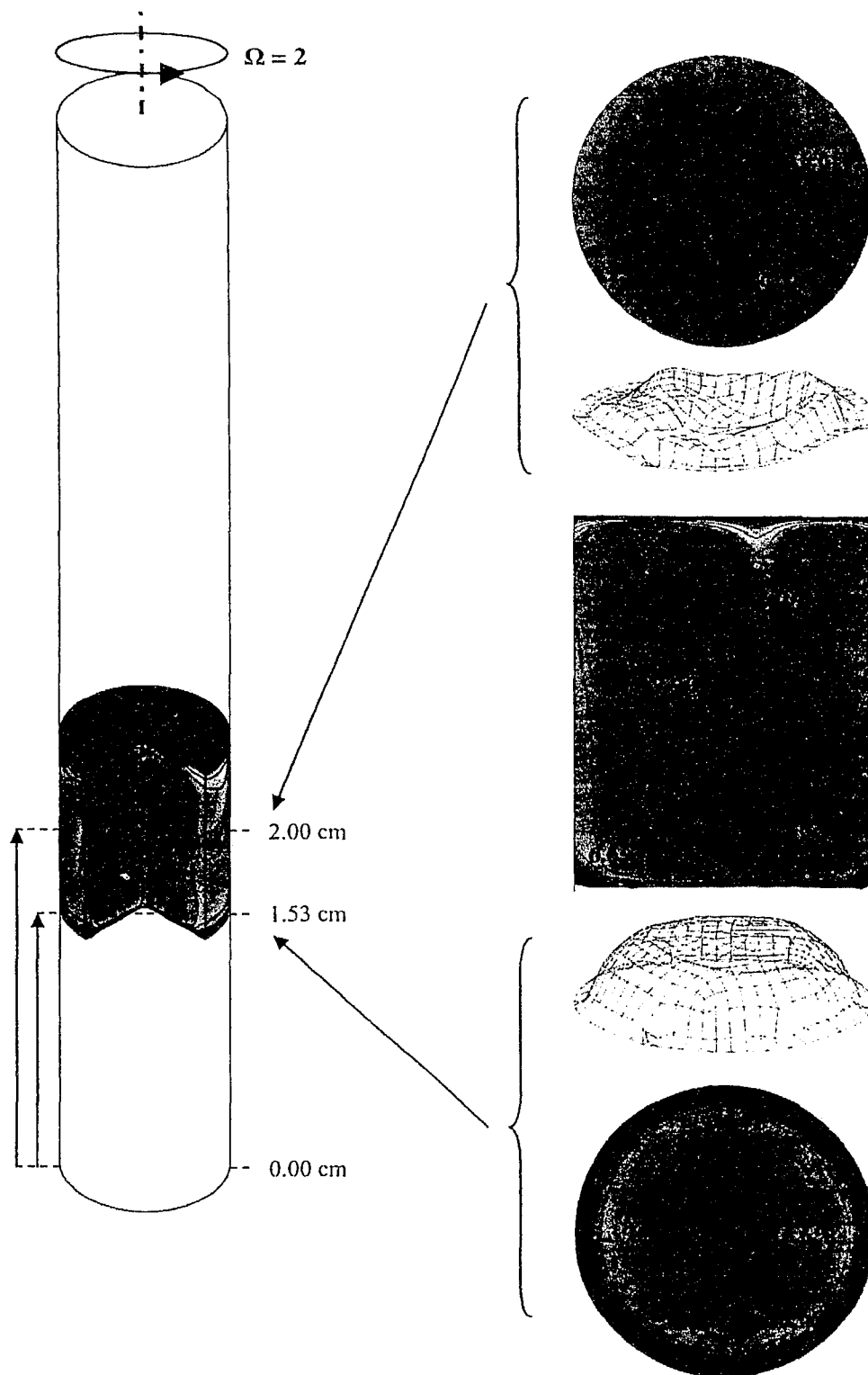


Figure 4.9 Silicon distribution contours for $\Omega = 2$ (terrestrial condition).

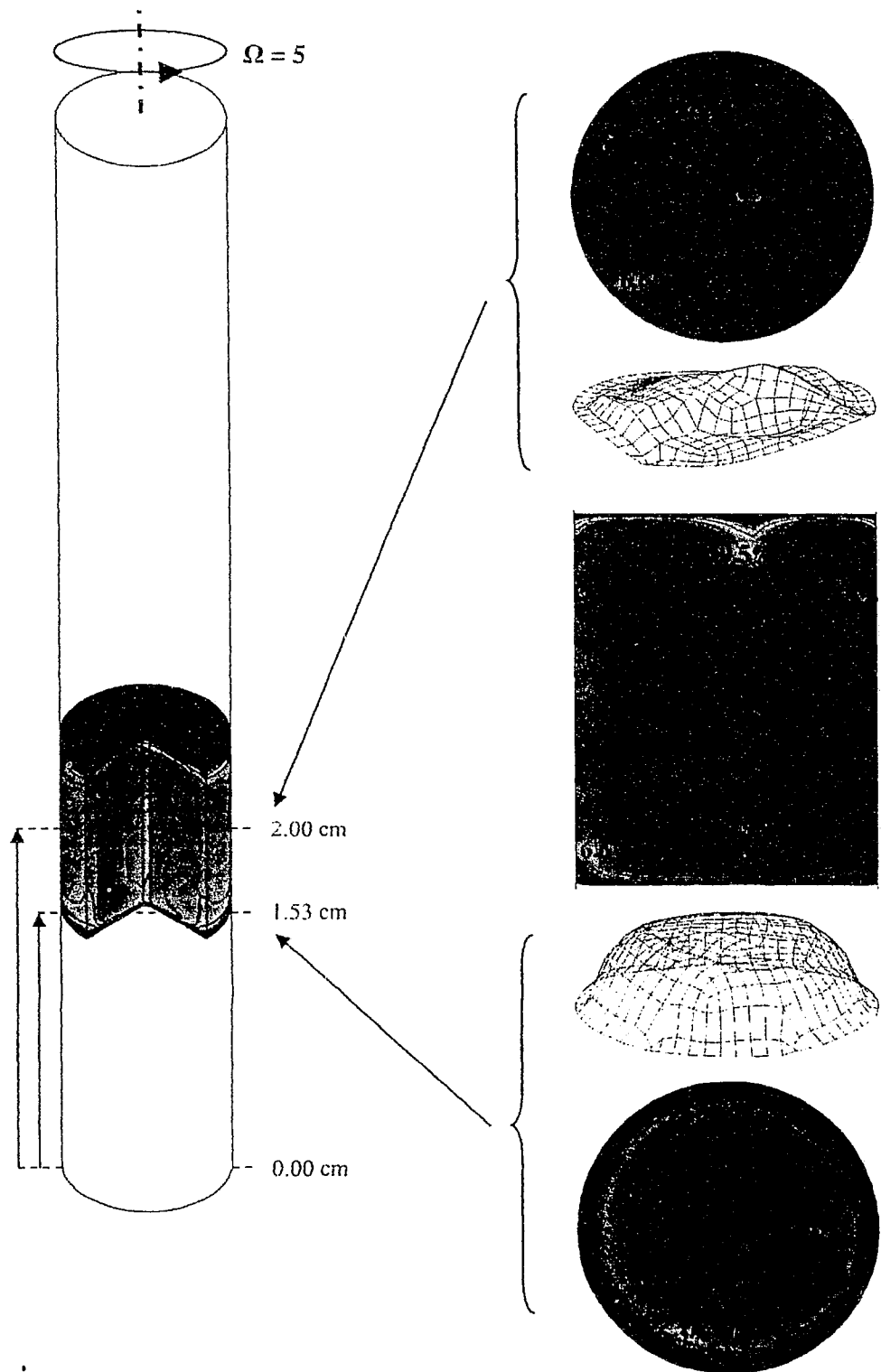


Figure 4.10 Silicon distribution contours for $\Omega = 5$ (terrestrial condition).

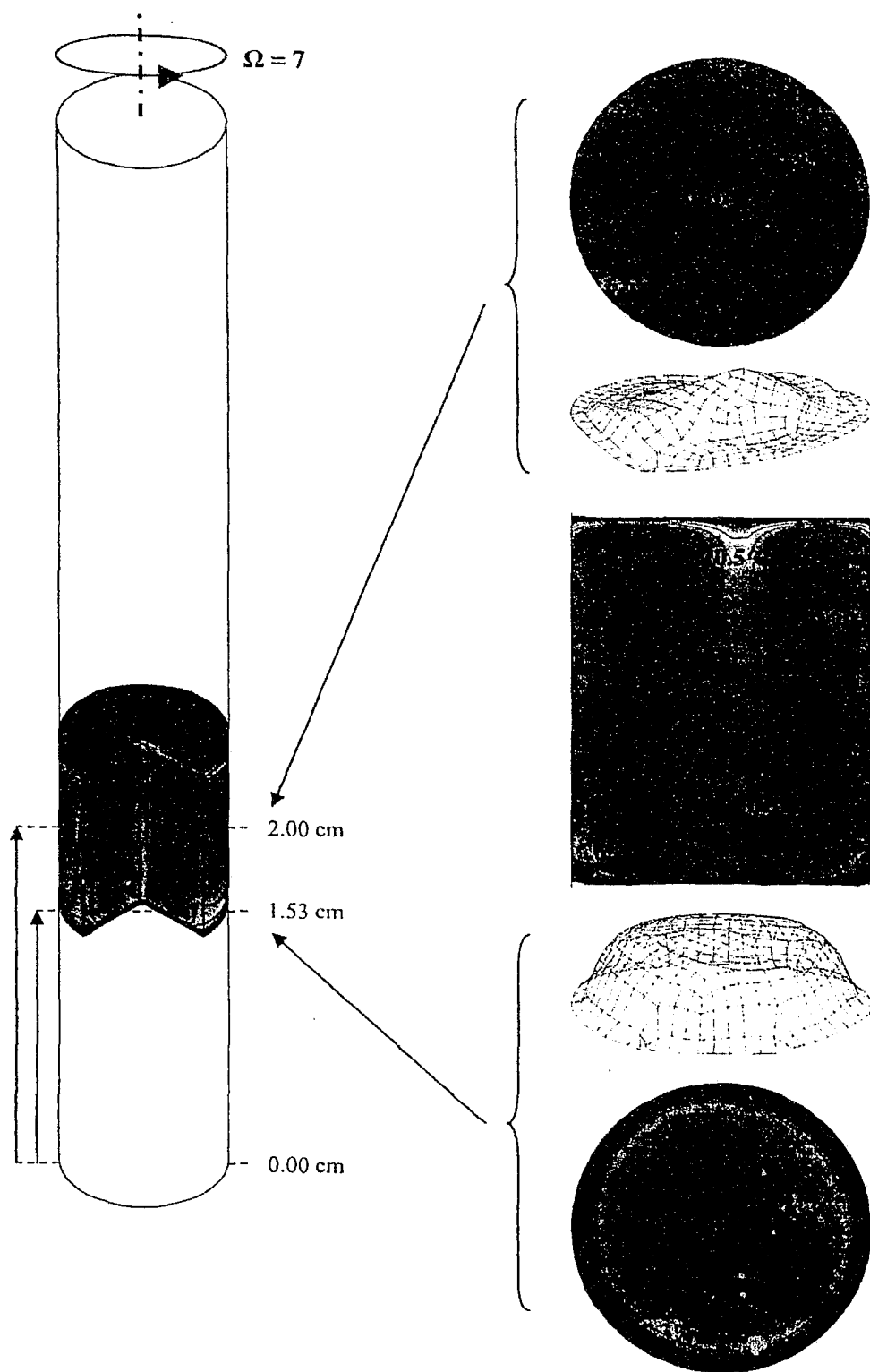


Figure 4.11 Silicon distribution contours for $\Omega \approx 7$ (terrestrial condition).

The silicon concentration distribution at 0.03 cm above the growth interface for the rotational speeds of 0, 2, 5, 7 and 10 rpm can be seen in Figure 4.12. This graph is plotted along the radial line of unsymmetrical heating as was done with the axial velocity previously. With the speed of 0 rpm, a concave shape is observed as well as no symmetry being present. At 2 rpm, concentration distribution keeps the same shape but is increased. Moving to 5 and 7 rpm, the concentration is further increased and the distribution has become flat and symmetric which is ideal for crystal growth. Out of the 5 and 7 rpm cases, the 5 rpm condition is more desirable as it is at a higher concentration while also having its uniformity slightly more stretched out along the growth interface than that of 7 rpm. The rotational speed of 10 rpm has been plotted just as in chapter 3 to show how any larger rotational speed produces undesirable results. Here it can be seen that at 10 rpm the concentration distribution is lowered, taking a concave shape and has become unsymmetrical, all of which are undesirable for crystal growth.

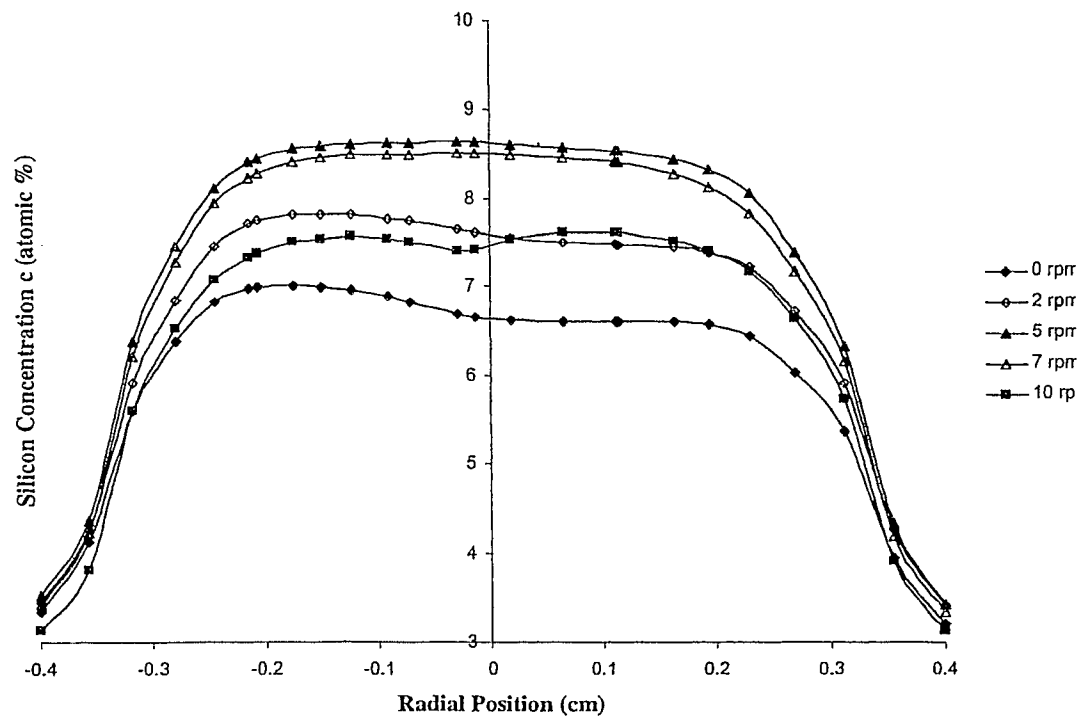


Figure 4.12 Silicon distribution at 0.03 cm above the growth interface (terrestrial condition).

4.2 Microgravity Condition

The microgravity condition is studied with the non-uniform heating condition to better understand the flow phenomenon within the solution zone as was done in chapter 3 where this can be considered a pure diffusion experiment where $g = 10^{-4}g_0$. In the microgravity condition the rotational speeds of 0, 2 and 5 rpm have been applied to the non-uniform heating crystal growth model. The axial-direction velocity contours for these rotational speeds are shown in Figures 4.13 – 4.15. The figures show a three-dimensional model, a horizontally cut plane 0.25 cm below the dissolution interface, a vertically cut plane along the plane of unsymmetrical heating, an axial velocity variation plot at 0.03 cm above the growth interface and two horizontal surface graphs showing the three-dimensional axial velocity variation at 0.25 cm below the dissolution interface and at 0.03 cm above the growth interface.

At 0 rpm shown in Figure 4.13, the three-dimensional model shows that vertically an unsymmetrical flow has resulted in the system. In the horizontally cut plane, it can be seen that three flow cells have formed and a line symmetry exists. In this plane there is very little flow on the order of 10^{-5} cm/s. Below the horizontal plane the three-dimensional velocity graph shows this velocity variation. The vertically cut plane shows the three flows just as in the uniform heating case but now these flow cells have become unsymmetrical. At the center of the middle flow cell there is a velocity of -1.6×10^{-4} cm/s and at the center of the left and right flow cells velocities of 1.3×10^{-4} cm/s and 6.4×10^{-5} cm/s respectively. Looking at the velocity variation plot and the three-dimensional horizontal surface graph, it is observed that the flow at 0.03 cm above the growth interface is just as in chapter 3 almost nonexistent.

Figure 4.14 shows the application of 2 rpm to the sample. In the horizontal view, this line of symmetry that was present has now been lost and the velocity has increased throughout the whole plane. In the vertical plane, there is a formation of four flow cells where the three that were present at 0 rpm have been compressed towards the growth interface and a new one has formed above them. The velocity at the center of the middle flow cell has increased to -4.3×10^{-4} cm/s and the velocities at the center of the left and right flow cells have increased to 2.2×10^{-4} cm/s and

1.5×10^{-4} cm/s respectively. The velocity in the newly formed flow cell above the others is much less being 7.9×10^{-5} cm/s. Looking at the velocity variation plot and the three-dimensional horizontal surface graph at 0.03 cm above the growth interface, the velocity has increased throughout this plane to $\pm 5 \times 10^{-5}$ cm/s. This increase in velocity is due to the fact the three flow cells observed at 0 rpm have been pushed closer to the growth interface.

At 5 rpm shown in Figure 4.15, the same complex formation of flow cells has occurred that where present with the uniform heating condition in chapter 3. In the horizontal plane, it can be seen that the flow contours have been more evenly distributed and two small abrupt contour regions have formed. The flow at the center has decreased from 7.8×10^{-5} cm/s in the 2 rpm case to 4.4×10^{-5} cm/s and the velocity in the abrupt regions is 1.9×10^{-4} cm/s. This decrease in velocity in the center can be seen in the three-dimensional surface graph. Looking at the horizontal plane, the exact same pattern of contour cells has formed to that of the uniform heating condition. In examining the flow velocities, it is observed that all the contours are very close to that of the uniform heating condition indicating that in the microgravity condition the application of 5 rpm takes control over the flow in the system. The velocity variation plot here also varies in the same magnitude as in chapter 3 from -1.5×10^{-4} to 2.5×10^{-4} and the same undesirable shape of velocity distribution is shown in the three-dimensional surface graph at 0.03 cm above the growth interface.

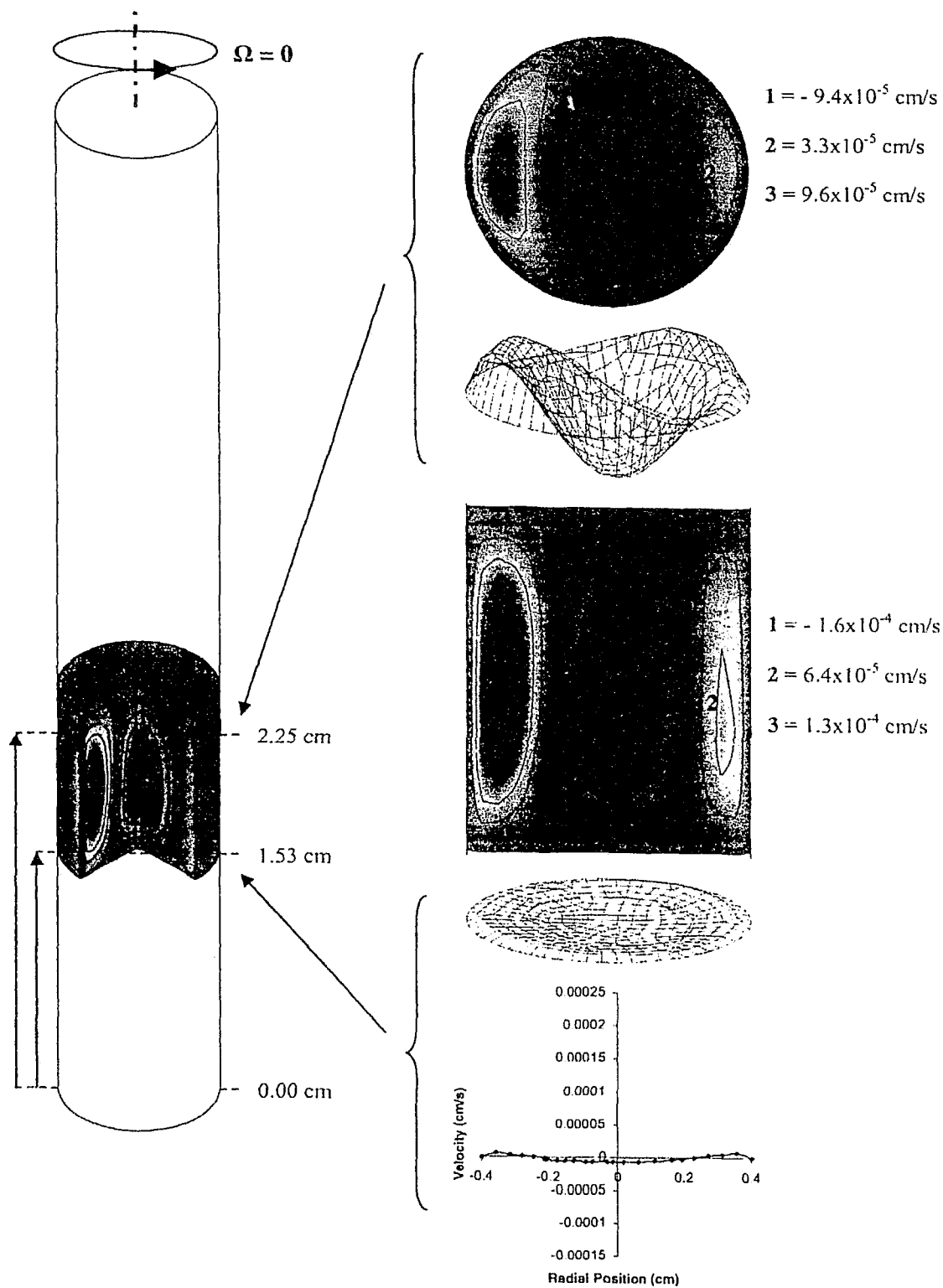


Figure 4.13 Axial direction velocity contours for $\Omega = 0$ (microgravity condition).

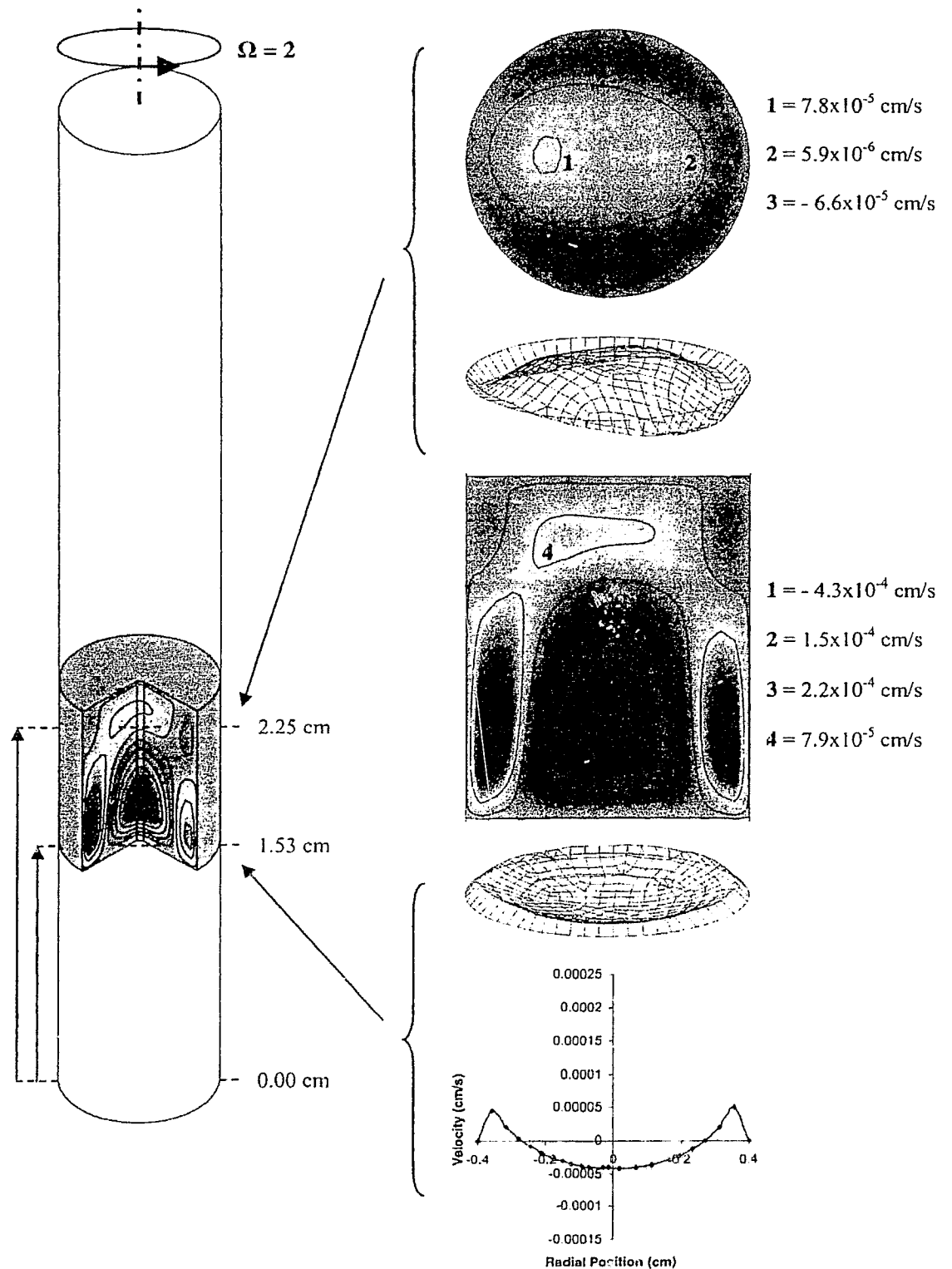


Figure 4.14 Axial direction velocity contours for $\Omega = 2$ (microgravity condition).

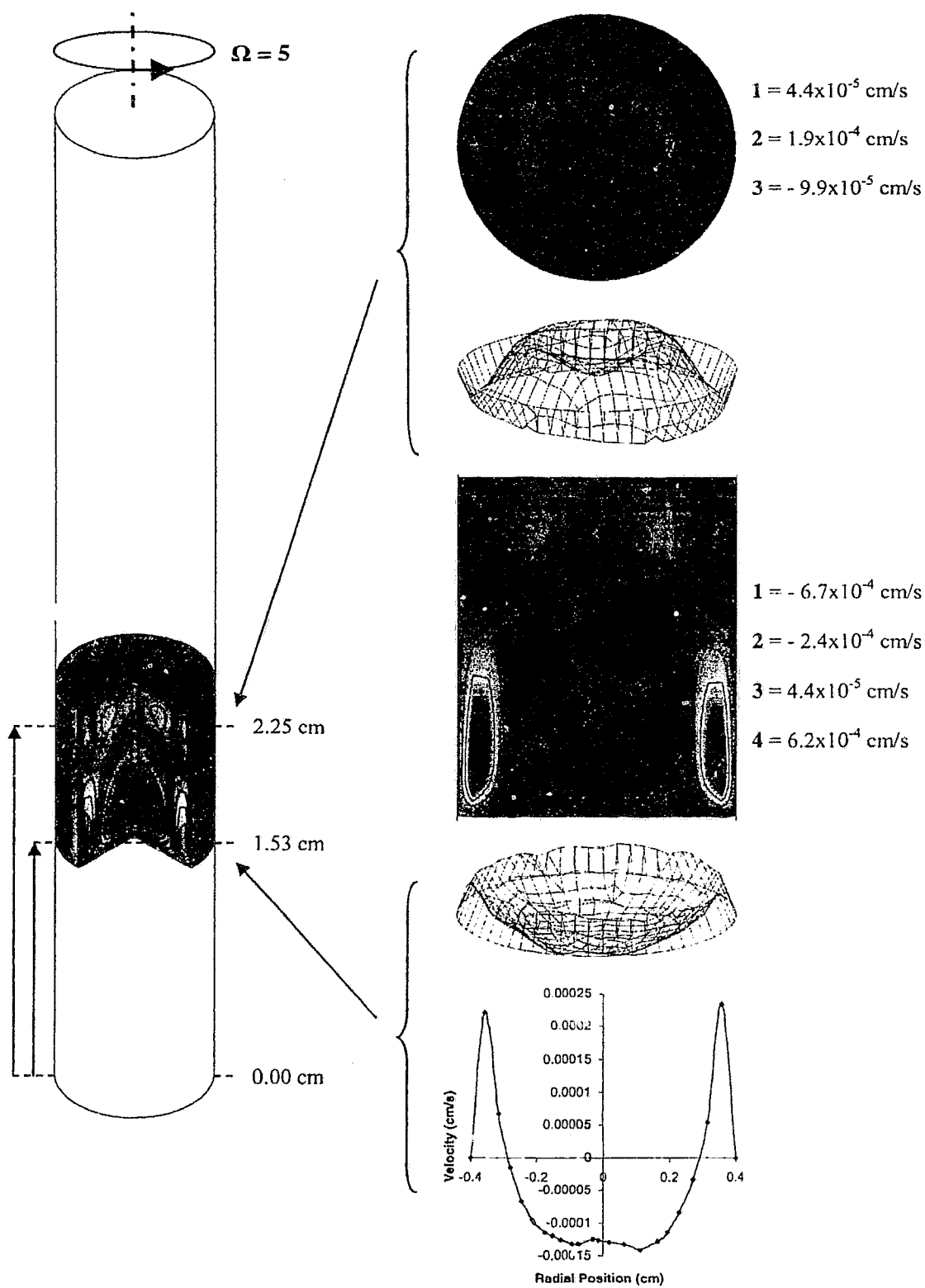


Figure 4.15 Axial direction velocity contours for $\Omega = 5$ (microgravity condition).

Figure 4.16 shows the maximum speed of flow graphed as a function of the rotational speeds of 0, 2 and 5 rpm. The maximum speed of flow increases from 1.72×10^{-4} cm/s at 0 rpm to 1.79×10^{-3} cm/s at 5 rpm. This again shows that just as in chapter 3 the application of crucible rotation does not help in suppressing the flow in the microgravity condition, but increases the speed of the flow throughout the system, and gives complex unsteady flow conditions along the growth interface.

Figures 4.17 – 4.19 display the concentration contours obtained from the rotational speeds of 0, 2 and 5 rpm. The application of 0 rpm is shown in Figure 4.17. Here it can be seen that with no rotation there is almost perfectly smooth concentration contours and that the non-uniform heating has slightly raised these contours on the left side. At 2 rpm Figure 4.18 just as in the uniform heating condition, a slight dip has been added to the silicon concentration contours in the system due to the increased velocity of flow and the added centripetal force. This dip is further increased with the application of 5 rpm shown in Figure 4.19. From the rotational speeds shown, rotational speed of 0 rpm is the most desired as it provides the most uniform and flat concentration along the growth interface as is observed in Figure 4.20 where the concentration at 0.03 cm above the growth interface has been plotted for the three rotational speeds.

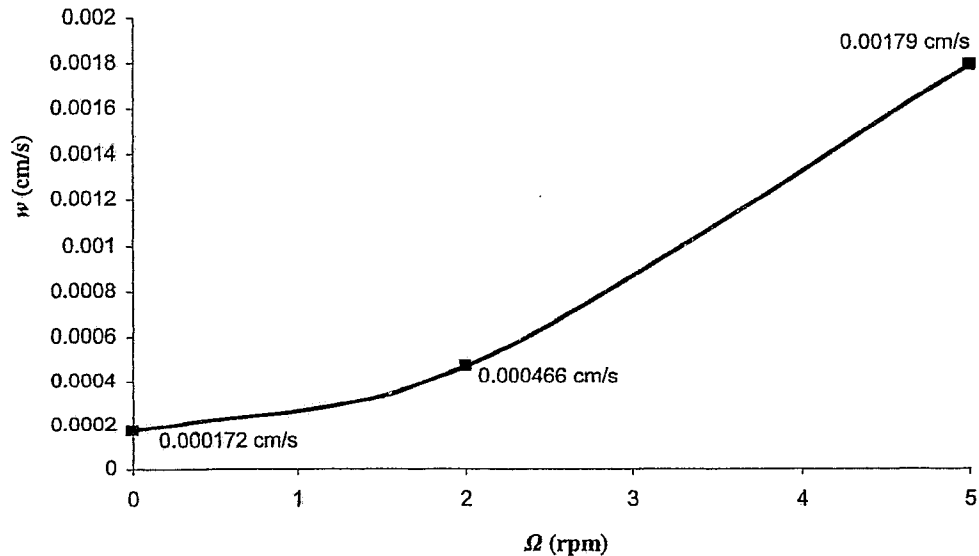


Figure 4.16 Maximum speed as a function of rotation (microgravity condition).

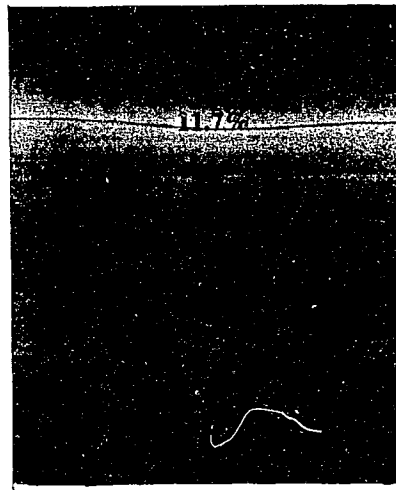
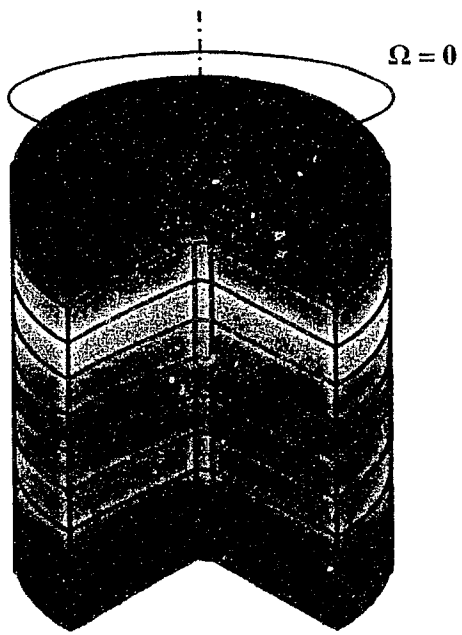


Figure 4.17 Silicon distribution contours for $\Omega = 0$ (microgravity condition).

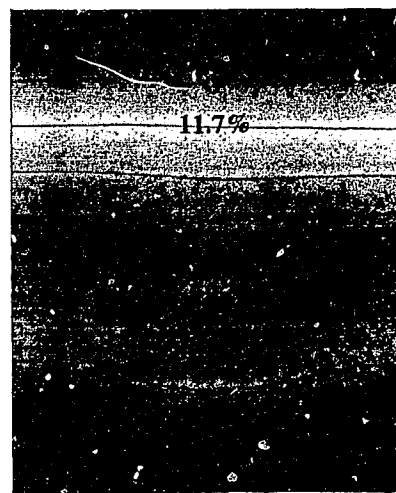
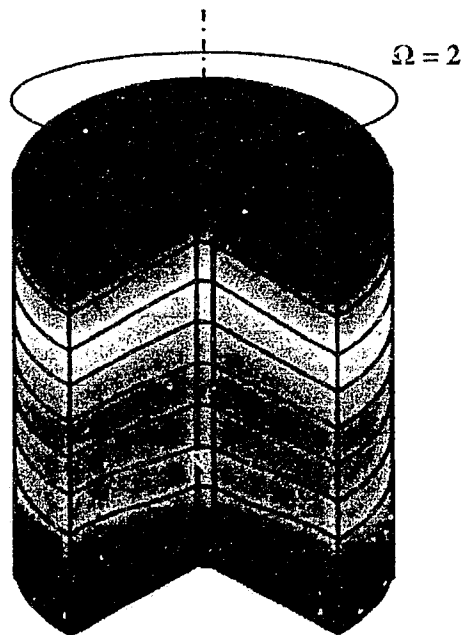


Figure 4.18 Silicon distribution contours for $\Omega = 2$ (microgravity condition).

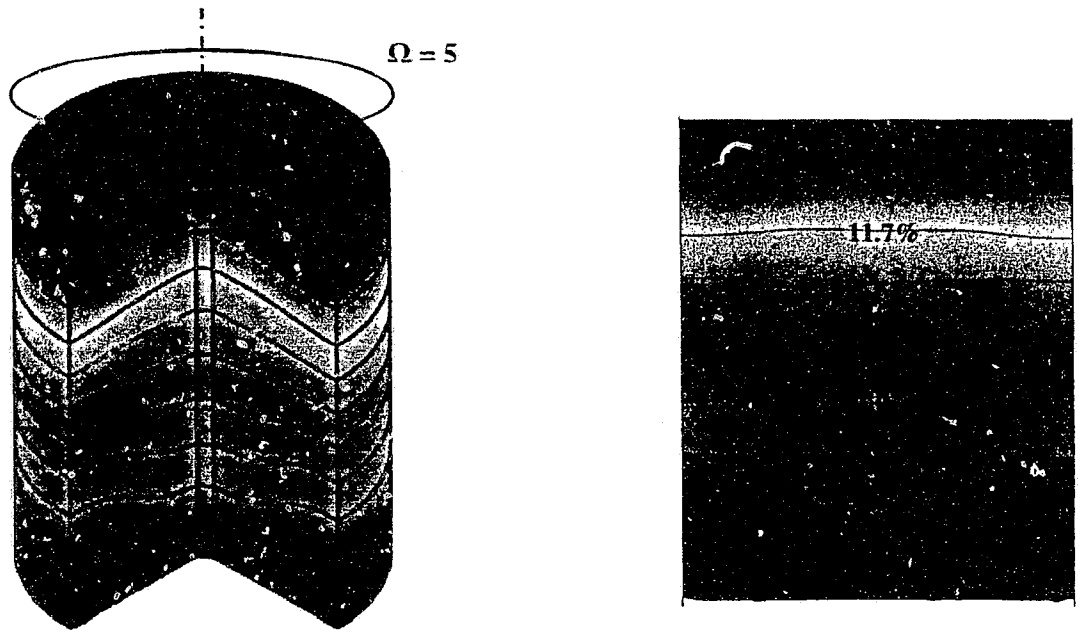


Figure 4.19 Silicon distribution contours for $\Omega = 5$ (microgravity condition).

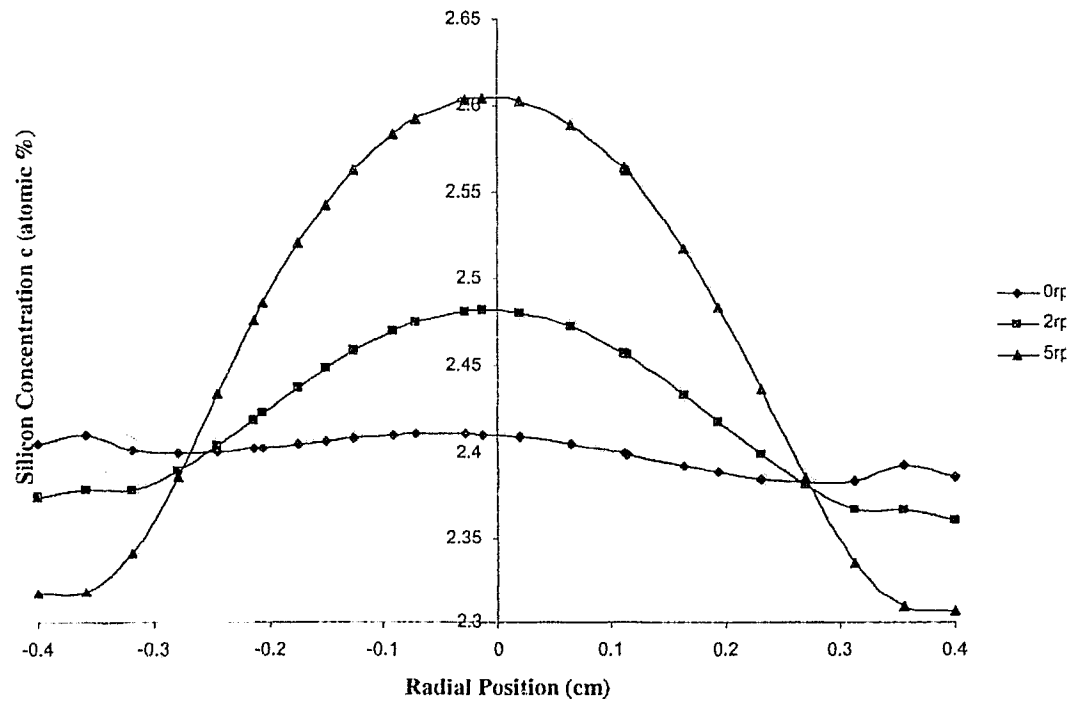


Figure 4.20 Silicon distribution at 0.03 cm above the growth interface (microgravity condition).

CHAPTER 5

Conclusion

A study of buoyancy driven convection in the $\text{Ge}_{0.98}\text{Si}_{0.02}$ solution has been conducted in order to study the effect of added crucible rotation on the crystal growth of $\text{Ge}_{1-x}\text{Si}_x$ by the traveling solvent method. This has been carried out by developing a three-dimensional thermal-solutal model, which accounts for the influence of both the thermal and solutal convections in the heat and mass transfer of the system. The three-dimensional model incorporates the use of the quasi-steady state condition of temperature, concentration and convective flow fields throughout the system. In addition, mesh sensitivity analysis has been carried out to ensure accuracy in results while saving computational time.

The application of crucible rotation has been applied to two cases, the uniform heating condition and the non-uniform heating condition. In each of the cases, both the terrestrial and the microgravity condition have been analyzed. In the terrestrial condition, the rotational speeds of 0, 2, 5 and 7 rpm have been applied and in the microgravity condition, the rotational speeds of 0, 2 and 5 rpm have been applied. With uniform heating under the terrestrial condition, it was found that crucible rotation was successful in suppressing the buoyancy induced flow throughout the system and provided a much flatter, smoother and more uniform silicon concentration along the growth interface. It was also noticed that the rotational effect minimized the three-dimensional flow characteristics throughout the solution zone. For this condition an optimal speed of 7 rpm was found to be the most suitable for crystal growth; any rotational speed higher than this lead to a concave silicon concentration distribution along the growth interface being undesirable for crystal growth.

In the case of non-uniform heating under terrestrial conditions, it was observed that crucible rotation was again successful in suppressing the buoyancy induced flow throughout the system giving a more uniform velocity distribution across the growth interface. The rotation in this case did not add much symmetry to the flow as it did in the uniform heating condition. The rotation of the system

increased the smoothness and uniformity of the silicon concentration along the growth interface up until 7 rpm where any higher rotational speeds lead to non-uniform silicon distribution along the growth interface. For this condition, the rotational speeds of 5 and 7 rpm were considered the best for crystal growth. Out of the two, the optimal speed of 5 rpm was chosen as it provided a higher concentration along the growth interface while having a slightly wider uniform concentration distribution to that of 7 rpm along the growth interface.

The microgravity condition in both cases showed that with increasing rotational speeds, more complex flows were formed resulting in a very complex flow along the growth interface as well as increasing the non-uniformity of silicon distribution, neither being desirable for crystal growth. An interesting result was observed in the 5 rpm case where the non-uniform heating condition flow matched that of the uniform heating condition. This result is thought to be due to the fact that the effect of rotation overcame the force of unsteady flow caused by non-uniform heating in the system, thereby giving the same result to that of the uniform heating condition. From these results it is highly recommended not to add rotation to the system in microgravity even if non-uniform heating is present.

Ultimately for crystal growth, the most desired condition is to have a solvent region which consists of pure diffusion. This is accomplished by having zero velocity. To obtain zero velocity, the convective flow due to buoyancy must be eliminated; the best way of achieving this is to apply the microgravity condition where the growth process would have to occur in space. It is also required to have a flat smooth and uniform silicon concentration distribution along the growth interface. This will allow for a much larger crystal to be grown with less stress being applied to the crystal lattice.

In conclusion, under terrestrial conditions, the application of rotation to the crystal growth system will improve the grown crystal quality but under *microgravity* conditions, the crystal growth process is best left undisturbed with no rotation added. The results of this numerical simulation will be helpful in future experimental studies where rotation will be applied for crystal growth.

For further study, it would be interesting to see the effect crucible rotation would have on the model if the system underwent crucible misalignment where gravity would no longer be acting directly downwards, but at a slight angle. Also it would be interesting to observe the effect of rotation with crucible misalignment being combined to that of the non-uniform heating condition.

APPENDIX A

Table A.1. Source Material Properties

Physical Properties of $\text{Ge}_{0.8}\text{Si}_{0.15}$		
Parameter	Symbol	Values
Density	ρ	5.06 g/cm ³
Thermal conductivity	κ	0.2905 W/cmK
Specific heat	c_p	0.0471 J/gK
Kinematic viscosity	ν	2.7x10 ⁻³ cm ² /s
Solutal expansion coefficient	β_c	0.005 c ⁻¹
Thermal expansion coefficient	β_T	1.2x10 ⁻⁴ K ⁻¹
Solutal diffusivity	α_c	2.6x10 ⁻⁴ cm ² /s
Thermal diffusivity	α_T	1.2x10 ⁻¹ cm ² /s
Melt temperature	T_m	1100 °C
Latent heat of fusion	L_f	39 cal/g

Table A.2. Solvent Material Properties

Physical Properties of $\text{Ge}_{0.98}\text{Si}_{0.02}$		
Parameter	Symbol	Values
Density	ρ	5.45 g/cm ³
Thermal conductivity	κ	0.2559 W/cmK
Specific heat	c_p	0.0401 J/gK
Viscosity	μ	7.35x10 ⁻³ g/cm.s
Kinematic viscosity	ν	1.4011x10 ⁻³ cm ² /s
Solutal expansion coefficient	β_c	0.005 c ⁻¹
Thermal expansion coefficient	β_T	1.2x10 ⁻⁴ K ⁻¹
Solutal diffusivity	α_c	1.0x10 ⁻⁴ cm ² /s
Melt temperature	T_m	971 °C
Solidification rate	V_g	1.16x10 ⁻⁵ mm/s

Table A.3. Crystal Material Properties

Physical Properties of Ge		
Parameter	Symbol	Values
Density	ρ	5.51 g/cm ³
Thermal conductivity	κ	0.2500 W/cm·K
Specific heat	c_p	0.0390 J/g·K
Kinematic viscosity	ν	1.54x10 ⁻³ cm ² /s
Solutal expansion coefficient	β_c	0.005 c ⁻¹
Thermal expansion coefficient	β_T	1.0x10 ⁻⁴ K ⁻¹
Solutal diffusivity	α_c	1.0x10 ⁻⁴ cm ² /s
Thermal diffusivity	α_T	1.2x10 ⁻¹ cm ² /s
Melt temperature	T_m	935 °C

APPENDIX B

Non-Dimensionalization

Navier-Stokes Equations

r – Component:

$$\begin{aligned} \rho \left[u_r \frac{\partial u_r}{r} + \frac{u_\theta}{r} \frac{\partial u_r}{\partial \theta} - \frac{u_\theta^2}{r} + u_z \frac{\partial u_z}{\partial z} \right] = - \frac{\partial p}{\partial r} \\ + \mu \left[\frac{1}{r} \frac{\partial}{\partial r} \left(r \frac{\partial u_r}{\partial r} \right) + \frac{1}{r^2} \frac{\partial u_r^2}{\partial \theta^2} + \frac{\partial^2 u_r}{\partial z^2} - \frac{u_r}{r^2} - \frac{2}{r^2} \frac{\partial u_\theta}{\partial \theta} \right] - \rho \omega^2 r - \rho 2 \alpha u_r \end{aligned} \quad (B.1)$$

The following dimensionless variables are introduced into the equation:

$$r = RL, \quad \theta = \theta, \quad z = ZL, \quad u_r = U_r u_0, \quad u_\theta = U_\theta u_0, \quad u_z = U_z u_0, \quad p = \frac{P \mu u_0}{L}, \quad \omega = \frac{\omega^* u_0}{L}$$

L.S.

$$\rho \left[U_r u_0 \frac{\partial U_r u_0}{\partial RL} + \frac{U_\theta u_0}{RL} \frac{\partial U_r u_0}{\partial \theta} - \frac{(U_\theta u_0)^2}{RL} + U_z u_0 \frac{\partial U_r u_0}{\partial ZL} \right]$$

Simplifying gives:

$$\rho \frac{u_0^2}{L} \left[U_r \frac{\partial U_r}{\partial R} + \frac{U_\theta}{R} \frac{\partial U_r}{\partial \theta} - \frac{U_\theta^2}{R} + U_z \frac{\partial U_r}{\partial Z} \right]$$

R.S.

$$\begin{aligned} - \frac{\partial \left(\frac{P \mu u_0}{L} \right)}{\partial RL} + \mu \left[\frac{1}{RL} \frac{\partial}{\partial RL} \left(RL \frac{\partial U_r u_0}{\partial RL} \right) + \frac{1}{(RL)^2} \frac{\partial^2 (U_r u_0)^2}{\partial \theta^2} \right. \\ \left. + \frac{\partial^2 (U_r u_0)}{\partial (ZL)^2} - \frac{U_r u_0}{(RL)^2} - \frac{2}{(RL)^2} \frac{\partial U_\theta u_0}{\partial \theta} \right] \\ - \rho \left(\frac{\omega^* u_0}{L} \right)^2 RL - \rho 2 \frac{\omega^* u_0}{L} U_r u_0 \end{aligned}$$

Simplifying gives:

$$\mu \frac{u_0}{L^2} \left[-\frac{\partial P}{\partial R} + \frac{1}{R} \frac{\partial}{\partial R} \left(R \frac{\partial U_r}{\partial R} \right) + \frac{1}{(R)^2} \frac{\partial^2 U_r}{\partial \theta^2} + \frac{\partial^2 (U_r)}{\partial Z^2} - \frac{U_r}{R^2} - \frac{2}{R^2} \frac{\partial U_\theta}{\partial \theta} \right] - \rho \left(\frac{\omega^* u_0}{L} \right)^2 RL - \rho 2 \frac{\omega^* u_0}{L} U_r u_0$$

Multiplying through both sides by $\frac{L^2}{\mu u_0}$, a factor chosen to further simplify the

equation gives:

$$\rho \frac{u_0 L}{\mu} \left[U_r \frac{\partial U_r}{\partial R} + \frac{U_\theta}{R} \frac{\partial U_r}{\partial \theta} - \frac{U_\theta^2}{R} + U_z \frac{\partial U_r}{\partial Z} \right] = \left[-\frac{\partial P}{\partial R} + \frac{1}{R} \frac{\partial}{\partial R} \left(R \frac{\partial U_r}{\partial R} \right) + \frac{1}{(R)^2} \frac{\partial^2 U_r}{\partial \theta^2} + \frac{\partial^2 U_r}{\partial (Z)^2} - \frac{U_r}{R^2} - \frac{2}{R^2} \frac{\partial U_\theta}{\partial \theta} \right] - \rho \frac{u_0 L}{\mu} (\omega^* R + 2\omega^* U_r)$$

This further simplifies to:

$$\text{Re} \left[U_r \frac{\partial U_r}{\partial R} + \frac{U_\theta}{R} \frac{\partial U_r}{\partial \theta} - \frac{U_\theta^2}{R} + U_z \frac{\partial U_r}{\partial Z} \right] = \left[-\frac{\partial P}{\partial R} + \nabla^2 U_r - \frac{U_r}{R^2} - \frac{2}{R^2} \frac{\partial U_\theta}{\partial \theta} \right] - \text{Re}(\omega^* R + 2\omega^* U_r) \quad (\text{B.2})$$

θ - Component

$$\rho \left[u_r \frac{\partial u_\theta}{\partial r} + \frac{u_\theta}{r} \frac{\partial u_\theta}{\partial \theta} + \frac{u_r u_\theta}{r} + u_z \frac{\partial u_\theta}{\partial z} \right] = -\frac{1}{r} \frac{\partial p}{\partial \theta} + \mu \left[\frac{\partial}{\partial r} \left(\frac{1}{r} \frac{\partial}{\partial r} (r u_\theta) \right) + \frac{1}{r^2} \frac{\partial^2 u_\theta}{\partial \theta^2} + \frac{2}{r^2} \frac{\partial u_r}{\partial \theta} + \frac{\partial^2 u_\theta}{\partial z^2} \right] \quad (\text{B.3})$$

The following dimensionless variables are introduced into the equation:

$$r = RL, \quad \theta = \theta, \quad z = ZL, \quad u_r = U_r u_0, \quad u_\theta = U_\theta u_0, \quad u_z = U_z u_0, \quad p = \frac{P \mu u_0}{L}$$

L.S.

$$\rho \left[U_r u_0 \frac{\partial (U_\theta u_0)}{\partial RL} + \frac{U_\theta u_0}{RL} \frac{\partial (U_\theta u_0)}{\partial \theta} + \frac{U_r u_0 U_\theta u_0}{RL} + U_z u_0 \frac{\partial (U_\theta u_0)}{\partial ZL} \right]$$

Simplifying gives:

$$\rho \frac{u_0^2}{L} \left[U_r \frac{\partial U_\theta}{\partial R} + \frac{U_\theta}{R} \frac{\partial U_\theta}{\partial \theta} + \frac{U_r U_\theta}{R} + U_z \frac{\partial U_\theta}{\partial Z} \right]$$

R.S.

$$-\frac{1}{RL} \frac{\partial \left(\frac{P\mu u_0}{L} \right)}{\partial \theta} + \mu \left[\frac{\partial}{\partial RL} \left(\frac{1}{RL} \frac{\partial (RL U_\theta u_0)}{\partial RL} \right) + \frac{1}{(RL)^2} \frac{\partial^2 (U_\theta u_0)}{\partial \theta^2} \right]$$

$$+ \frac{2}{(RL)^2} \frac{\partial (U_r u_0)}{\partial \theta} + \frac{\partial^2 (U_\theta u_0)}{\partial (ZL)^2}$$

Simplifying gives:

$$\mu \frac{u_0}{L^2} \left[-\frac{1}{R} \frac{\partial P}{\partial \theta} + \nabla^2 U_\theta + \frac{2}{R^2} \frac{\partial U_r}{\partial \theta} \right]$$

Multiplying through both sides by $\frac{L^2}{\mu u_0}$, a factor chosen to further simplify the equation gives:

$$\rho \frac{u_0 L}{\mu} \left[U_r \frac{\partial U_\theta}{\partial R} + \frac{U_\theta}{R} \frac{\partial U_\theta}{\partial \theta} - \frac{U_r U_\theta}{R} + U_z \frac{\partial U_\theta}{\partial Z} \right] = \left[-\frac{1}{R} \frac{\partial P}{\partial \theta} + \nabla^2 U_\theta + \frac{2}{R^2} \frac{\partial U_r}{\partial \theta} \right]$$

This further simplifies to:

$$\text{Re} \left[U_r \frac{\partial U_\theta}{\partial R} + \frac{U_\theta}{R} \frac{\partial U_\theta}{\partial \theta} - \frac{U_r U_\theta}{R} + U_z \frac{\partial U_\theta}{\partial Z} \right] = \left[-\frac{1}{R} \frac{\partial P}{\partial \theta} + \nabla^2 U_\theta + \frac{2}{R^2} \frac{\partial U_r}{\partial \theta} \right] \quad (\text{B.4})$$

z - Component:

$$\rho \left[u_r \frac{\partial u_z}{\partial r} + \frac{u_\theta}{r} \frac{\partial u_z}{\partial \theta} + u_z \frac{\partial u_z}{\partial z} \right] = -\frac{\partial p}{\partial z} + \mu \left[\frac{1}{r} \frac{\partial}{\partial r} \left(r \frac{\partial u_z}{\partial r} \right) + \frac{1}{r^2} \frac{\partial^2 u_z}{\partial \theta^2} + \frac{\partial^2 u_z}{\partial z^2} \right] \quad (\text{B.5})$$

$$+ \rho g [\beta_T (T - T_m) - \beta_c (c - c_0)]$$

The following dimensionless variables are introduced into the equation:

$$r = RL, \quad \theta = \theta, \quad z = ZL, \quad u_r = U_r u_0, \quad u_\theta = U_\theta u_0, \quad u_z = U_z u_0, \quad p = \frac{P\mu u_0}{L},$$

$$c - c_0 = \Delta c C, \quad T - T_m = \Delta T \Theta$$

L.S.

$$\rho \left[U_r u_0 \frac{\partial U_z u_0}{\partial RL} + \frac{U_\theta u_0}{RL} \frac{\partial U_z u_0}{\partial \theta} + U_z u_0 \frac{\partial U_z u_0}{\partial ZL} \right]$$

Simplifying gives:

$$\rho \frac{u_0^2}{L} \left[U_r \frac{\partial U_z}{\partial R} + \frac{U_\theta}{R} \frac{\partial U_z}{\partial \theta} + U_z \frac{\partial U_z}{\partial Z} \right]$$

R.S.

$$-\frac{\partial \left(\frac{P \mu u_0}{L} \right)}{\partial ZL} + \mu \left[\frac{1}{RL} \frac{\partial}{\partial RL} \left(RL \frac{\partial U_z u_0}{\partial RL} \right) + \frac{1}{(RL)^2} \frac{\partial^2 U_z u_0}{\partial \theta^2} + \frac{\partial^2 U_z u_0}{\partial (ZL)^2} \right] + \rho g [\beta_T \Delta T \Theta - \beta_c \Delta c C]$$

Simplifying gives:

$$\mu \frac{u_0}{L^2} \left[-\frac{\partial P}{\partial Z} + \frac{1}{R} \frac{\partial}{\partial R} \left(R \frac{\partial U_z}{\partial R} \right) + \frac{1}{(R)^2} \frac{\partial^2 U_z}{\partial \theta^2} + \frac{\partial^2 U_z}{\partial (Z)^2} \right] + \rho g [\beta_T \Delta T \Theta - \beta_c \Delta c C]$$

Multiplying through both sides by $\frac{L^2}{\mu u_0}$, a factor chosen to further simplify the

equation gives:

$$\rho \frac{u_0 L}{\mu} \left[U_r \frac{\partial U_z}{\partial R} + \frac{U_\theta}{R} \frac{\partial U_z}{\partial \theta} + U_z \frac{\partial U_z}{\partial Z} \right] = \left[-\frac{\partial P}{\partial Z} + \frac{1}{R} \frac{\partial}{\partial R} \left(R \frac{\partial U_z}{\partial R} \right) + \frac{1}{(R)^2} \frac{\partial^2 U_z}{\partial \theta^2} + \frac{\partial^2 U_z}{\partial (Z)^2} \right] + \rho g \frac{L^2}{\mu u_0} [\beta_T \Delta T \Theta - \beta_c \Delta c C]$$

This further simplifies to:

$$\text{Re} \left[U_r \frac{\partial U_z}{\partial R} + \frac{U_\theta}{R} \frac{\partial U_z}{\partial \theta} + U_z \frac{\partial U_z}{\partial Z} \right] = \left[-\frac{\partial P}{\partial Z} + \nabla^2 U_z \right] + \frac{Gr}{\text{Re}} [\Theta - NC] \quad (\text{B.6})$$

Energy Transfer Equation

$$\rho c_p \left[u_r \frac{\partial T}{\partial r} + \frac{u_\theta}{r} \frac{\partial T}{\partial \theta} + u_z \frac{\partial T}{\partial z} \right] = k \left[\frac{1}{r} \frac{\partial}{\partial r} \left(r \frac{\partial T}{\partial r} \right) + \frac{1}{r^2} \frac{\partial^2 T}{\partial \theta^2} + \frac{\partial^2 T}{\partial z^2} \right] \quad (\text{B.7})$$

The following dimensionless variables are introduced into the equation:

$$r = RL, \quad \theta = \theta, \quad z = ZL, \quad u_r = U_r u_0, \quad u_\theta = U_\theta u_0, \quad u_z = U_z u_0, \quad T - T_m = \Delta T \Theta$$

This gives:

$$\text{Re Pr} \left[U_r \frac{\partial \Theta}{\partial R} + \frac{U_\theta}{R} \frac{\partial \Theta}{\partial \theta} + U_z \frac{\partial \Theta}{\partial Z} \right] = \nabla^2 \Theta \quad (\text{B.8})$$

Mass Transport Equation

$$u_r \frac{\partial c}{\partial r} + \frac{u_\theta}{r} \frac{\partial c}{\partial \theta} + u_z \frac{\partial c}{\partial z} = -\alpha_c \left[\frac{1}{r} \frac{\partial}{\partial r} \left(r \frac{\partial c}{\partial r} \right) + \frac{1}{r^2} \frac{\partial^2 c}{\partial \theta^2} + \frac{\partial^2 c}{\partial z^2} \right] \quad (\text{B.9})$$

The following dimensionless variables are introduced into the equation:

$$r = RL, \quad \theta = \theta, \quad z = ZL, \quad u_r = U_r u_0, \quad u_\theta = U_\theta u_0, \quad u_z = U_z u_0, \quad c - c_0 = \Delta c C$$

This gives:

$$\text{Re} \left[U_r \frac{\partial C}{\partial R} + \frac{U_\theta}{R} \frac{\partial C}{\partial \theta} + U_z \frac{\partial C}{\partial Z} \right] = \frac{1}{Sc} \left[\nabla^2 C \right] \quad (\text{B.10})$$

Continuity Equation

$$\frac{1}{r} \frac{\partial}{\partial r} (r u_r) + \frac{1}{r} \frac{\partial u_\theta}{\partial \theta} + \frac{\partial u_z}{\partial z} = 0 \quad (\text{B.11})$$

The following dimensionless variables are introduced into the equation:

$$r = RL, \quad \theta = \theta, \quad z = ZL, \quad u_r = U_r u_0, \quad u_\theta = U_\theta u_0, \quad u_z = U_z u_0$$

This gives:

$$\frac{1}{R} \frac{\partial (R U_r)}{\partial R} + \frac{1}{R} \frac{\partial U_\theta}{\partial \theta} + \frac{\partial U_z}{\partial Z} = 0 \quad (\text{B.12})$$

APPENDIX C

Dimensionless Rotational Speed

The FIDAP input file takes the rotational speed in terms of angular velocity. In order to apply the angular velocity to the model the dimensionless angular velocity must be found. Dimensionless angular velocity is defined as follows:

$$v^* = \omega^* r^* \quad (C.1)$$

Where:

$$v^* = \frac{v}{u_0} = \frac{\omega r}{u_0} \text{ and } \omega^* r^* = \omega^* \frac{r}{L}$$

Combining these relations:

$$\frac{\omega r}{u_0} = \omega^* \frac{r}{L}$$

Simplifies to:

$$\omega^* = \frac{\omega L}{u_0} \quad (C.2)$$

Where ω is the angular velocity and ω^* is the dimensionless angular velocity and rpm is related to angular velocity by:

$$rpm = \frac{2\pi}{60} rad / s = 0.1047 rad / s \quad (C.3)$$

Table C.3. Dimensionless Rotational Values

RPM	Dimensionless Value
1	0.374
2	0.748
3	1.122
4	1.496
5	1.870
6	2.244
7	2.618
8	2.990
9	3.365
10	3.740

APPENDIX D

FIPREP Input File

```
FICONV( NEUTRAL )
/(Name of file being called upon for the FEM mesh)
INPUT( FILE="6r7g1n.FDNEUT" )
OUTPUT( DELETE )
END
/
TITLE
/(File title)
6r7g1n
/
FIPREP
/
/      PROBLEM SETUP
/
PROBLEM (3-D, LAMINAR, NONLINEAR, BUOYANCY, FREE, BUOYANCY = 1 )
EXECUTION( NEWJOB )
PRINTOUT( NONE )
DATAPRINT( CONTROL )
/
RENUMBER( PROFILE )
LIQUIDUS( SET = "solvent", CONSTANT = 12.56, TEMPERATURE )
/
/      CONTINUUM ENTITIES
/
ENTITY ( NAME = "source", SOLID, PROPERTY = "source" )
ENTITY ( NAME = "solvent", FLUID, PROPERTY = "solvent", SPECIES = 1, MDIFF = 3,
MEXP = 3 )
ENTITY ( NAME = "substrate", FLUID, PROPERTY = "substrate", SPECIES = 1, MDIFF =
3 )
/
/      BOUNDARY ENTITIES
/
ENTITY ( NAME = "top", PLOT, ATTACH = "source" )
ENTITY ( NAME = "outflow", PLOT, ATTACH = "solvent" )
ENTITY ( NAME = "inflow", MELT, MSPHT = "solvent", DEPTH = -1, ATTACH =
"solvent", NATTACH = "substrate", SPECIES = 1, M1LIQU = "solvent" )
ENTITY ( NAME = "bottom", SURFACE, SPINE, STRAIGHT, DEPTH = 0, CONTINUE,
ATTACH = "substrate" )
ENTITY ( NAME = "profile1", PLOT )
ENTITY ( NAME = "profile2", PLOT )
ENTITY ( NAME = "profile3", PLOT )
ENTITY ( NAME = "interface_edge", PLOT )
/
/      SOLUTION PARAMETERS
/
SOLUTION( SEGREGATED = 450 )
PRESSURE( MIXED = 1.E-8, DISCONTINUOUS )
OPTIONS( UPWINDING )
UPWIND( 1STO )
```

```

/ MATERIAL PROPERTIES
/
/ Partial list of Material Properties data
/
DENSITY( SET = "source", CONSTANT = 233, TYP2, TEMPERATURE, SPECIES = 1 )
VISCOSITY( SET = "source", CONSTANT = 1 )
CONDUCTIVITY( SET = "source", CONSTANT = 1 )
SPECIFICHEAT( SET = "source", CONSTANT = 2.25E-2 )
VOLUMEXPANSION( SET = "source", CONSTANT = 1, TEMPERATURE )
/
DENSITY( SET = "solvent", CONSTANT = 450, TYP2, TEMPERATURE, SPECIES = 1 )
VISCOSITY( SET = "solvent", CONSTANT = 1 )
CONDUCTIVITY( SET = "solvent", CONSTANT = 1 )
SPECIFICHEAT( SET = "solvent", CONSTANT = 7E-3, LATENT = 2.23, TMELT = 36 )
VOLUMEXPANSION( SET = "solvent", CONSTANT = 1, TEMPERATURE )
/(Dimensionless gravity definition, defined as 1 for terrestrial /conditions and as 10-4 for
microgravity conditions)
GRAVITY( MAGNITUDE = 1 )
/
VOLUMEXPANSION( SET = 3, CONSTANT = 42, SPECIES = 1 )
DIFFUSIVITY( SET = 3, CONSTANT = 1.587E-4, SPECIES = 1 )
/
/DENSITY( SET = "substrate", CONSTANT = 409, TYP2, TEMPERATURE, SPECIES = 1
)
VISCOSITY( SET = "substrate", CONSTANT = 1 )
CONDUCTIVITY( SET = "substrate", CONSTANT = 1 )
SPECIFICHEAT( SET = "substrate", CONSTANT = 7E-3 )
VOLUMEXPANSION( SET = "substrate", CONSTANT = 1, TEMPERATURE )
/
/ INITIAL AND BOUNDARY CONDITIONS
/
/(Rotational command controlling rpm, omega is the dimensionless /rotational speed)
ROTATING( CENTRIFUGAL, CORIOLIS, OMEGA = 0.374, X = 0, Y = 0, Z = 1 )
/
BCNODE( COORDINATE, ENTITY = "interface_edge" )
BCSYSTEM( SET = 1, EDGE )
/
BCNODE( SURFACE, ZERO, ENTITY = "interface_edge" )
BCNODE( SURFACE, ZERO, ENTITY = "bottom" )
/
BCNODE( SPECIES = 1, CONSTANT = 0.15, ENTITY = "source" )
BCNODE( SPECIES = 1, CONSTANT = 0.02, ENTITY = "inflow" )
BCNODE( SPECIES = 1, CONSTANT = 0.15, ENTITY = "outflow" )
/
BCNODE( VELOCITY, CONSTANT = 0, ENTITY = "source" )
BCNODE( VELOCITY, CONSTANT = 0, ENTITY = "substrate" )
/
BCNODE( VELOCITY, CONSTANT = 0, ENTITY = "top" )
BCNODE( VELOCITY, CONSTANT = 0, ENTITY = "bottom" )
BCNODE( VELOCITY, CONSTANT = 0, ENTITY = "profile1" )
BCNODE( VELOCITY, CONSTANT = 0, ENTITY = "profile2" )
BCNODE( VELOCITY, CONSTANT = 0, ENTITY = "profile3" )
/
/(Three-dimensional heater thermal profile for source)
BCNODE( TEMPERATURE, POLYNOMIAL = 10, ENTITY = "profile1" )

```



```

-171.491674619836000 3.75234521575985 1 0 0 -0.0000000000000028217 0 1 0 -
23.468172284192400 0 0 1 14.0800946182358 2 0 0 -42.240284 0 2 0
784.323802803643000 0 0 2 -825.939526461064000 0 0 3 338.295844875043000 0 0 4 -
62.326428754429800 0 0 5 4.325223592473780 0 0 6
/
/(Three-diemsnional heater thermal profile for solvent)
BCNODE( TEMPERATURE, POLYNOMIAL = 10, ENTITY = "profile2" )
-171.491674619836000 3.75234521575985 1 0 0 -0.0000000000000028217 0 1 0 -
23.468172284192400 0 0 1 14.0800946182358 2 0 0 -42.240284 0 2 0
784.323802803643000 0 0 2 -825.939526461064000 0 0 3 338.295844875043000 0 0 4 -
62.326428754429800 0 0 5 4.325223592473780 0 0 6
/
/(Three-diemsnional heater thermal profile for crystal)
BCNODE( TEMPERATURE, POLYNOMIAL = 10, ENTITY = "profile3" )
-171.491674619836000 3.75234521575985 1 0 0 -0.0000000000000028217 0 1 0 -
23.468172284192400 0 0 1 14.0800946182358 2 0 0 -42.240284 0 2 0
784.323802803643000 0 0 2 -825.939526461064000 0 0 3 338.295844875043000 0 0 4 -
62.326428754429800 0 0 5 4.325223592473780 0 0 6
/
END
/
CREATE( FIPREP,DELETE )
PARAMETER( LIST )
CREATE( FISOLV )
/RUN( FISOLV, FOREGROUND )

```

APPENDIX E

3-D Heater Profiles used for Input File

Uniform Heating Condition

Polynomial = 6

-171.491674619836000 -23.468172284192400 0 0 1 784.323802803643000 0 0 2 -
825.939526461064000 0 0 3 338.295844875043000 0 0 4 -62.326428754429800 0 0 5
4.325223592473780 0 0 6

Non-Uniform Heating Condition

Polynomial = 10

-171.491674619836000 3.75234521575985 1 0 0 -0.0000000000000028217 0 1 0 -
23.468172284192400 0 0 1 14.0800946182358 2 0 0 -42.240284 0 2 0
784.323802803643000 0 0 2 -825.939526461064000 0 0 3 338.295844875043000 0 0 4 -
62.326428754429800 0 0 5 4.325223592473780 0 0 6

REFERENCES

- [1] G. Muller, A. Ostrogorsky. "Convection in the Melt" *Handbook of Crystal Growth*, 1994 Elsevier Science pp 711-819.
- [2] Hong Ouyang, Wei Shyy. "Numerical Simulation of CdTe Vertical Bridgman Growth" *Journal of Crystal Growth*, **173** (1997) pp 352-366.
- [3] C. Martinez-Tomas, V. Munoz. "CdTe Crystal Growth Process by the Bridgman Method: Numerical Simulation" *Journal of Crystal Growth*, **222** (2001) pp 435-451.
- [4] C. W. Lan, I.F. Lee, B.C. Yeh. "Three-Dimensional Analysis of Flow and Segregation in Vertical Bridgman Crystal Growth under Axial and Transversal Magnetic Fields" *Journal of Crystal Growth*, **254** (2003) pp 503-515.
- [5] "Czochralski Growth" Internet.
<http://www.csc.fi/staff/ville.savolainen/cz/thesis/node10.html>
- [6] Qiang Xiao. "Numerical Simulations of Transport Processes During Czochralski Growth of Semiconductor Compounds" *Journal of Crystal Growth*, **174** (1997) pp 7-12.
- [7] M. Tanaka, M. Hasebe, N. Saito. "Pattern Transition of Temperature Distribution at Czochralski Silicon Melt Surface" *Journal of Crystal Growth*, **180** (1997) pp 487-496.
- [8] D. Vizman, O. Grabner, G. Muller. "Three-Dimensional Numerical Simulation of Thermal Convection in an Industrial Czochralski Melt: Comparison to Experimental Results" *Journal of Crystal Growth*, **233** (2001) pp 687-698.
- [9] "Crystal Growth Descriptions and Definitions" Internet.
<http://www.geocites.com/shajan89/melt.html>
- [10] M. Z. Saghir, M. R. Islam, N. Maffei, D H. H. Quon. "Three-Dimensional Modeling of $\text{Bi}_{12}\text{GeO}_{20}$ using the Float Zone Technique" *Journal of Crystal Growth*, **193** (1998) pp 623-635.
- [11] T. A. Campbell, M. Schweizer, P. Dold, A. Croll, K. W. Benz. "Float Zone Growth and Characterization of $\text{Ge}_{1-x}\text{Si}_x$ ($x \leq 10$ at %) single crystals" *Journal of Crystal Growth*, **226** (2001) pp 231-239.
- [12] P. Dold, M. Schweizer, A. Croll, K. W. Benz. "Measurement of microscopic growth rates in float zone silicon crystals" *Journal of Crystal Growth*, **237-239** (2002) pp 1671-1677.

- [13] Satoshi Matsumoto, Toru Maekawa, katsumi Takahashi. "Numerical Analysis of InP Solution Growth by the Traveling Heater Method: Transient Response in the Case of no Heater Movement" *International Journal of Heat and Mass Transfer*, **40** (1997) pp 3237-3245.
- [14] B. Lent, S. Dost, R.F. Redden, Y. Liu. "Mathematical simulation of the Traveling Heater Method Growth of Ternary Semiconductor Materials Under Suppressed Gravity Conditions" *Journal of Crystal Growth*, **237-239** (2002) pp 1876-1880.
- [15] M. C. Martinez-Tomas, V. Munoz-Sanjose, C. Reig. "A Numerical Study of Thermal Conditions in the THM Growth of HgTe" *Journal of Crystal Growth*, **243** (2002) pp 463-475.
- [16] Chahid K. Ghaddar, Cheo K. Lee, Shariar Motakef, Donald C. Gillies. "Numerical Simulation of THM Growth of CdTe in Presence of Rotating Magnetic Fields (RMF)" *Journal of Crystal Growth*, **205** (1999) pp 97-111.
- [17] C. W. Lan. "Effects of Ampoule Rotation on Flows and Dopant Segregation in Vertical Bridgman Crystal Growth" *Journal of Crystal Growth*, **197** (1999) pp 983-991.
- [18] Yasunori Okano, Shin-saku Nishino, Shun-suke Ohkubo, Sadik Dost. "Numerical Study of Transport Phenomena in the THM Growth of Compound Semiconductor Crystals" *Journal of Crystal Growth*, **237-239** (2002) pp 1779-1784.
- [19] C. W. Lan. "Suppressing Three-Dimensional Unsteady Flows in Vertical Zone-Melting by Steady Ampoule Rotation" *Journal of Crystal Growth*, **213** (2000) pp 395-407.
- [20] C. W. Lan. "Effects of Ampoule Rotation on Vertical Zone-Melting Crystal Growth: Steady Rotation Versus Accelerated Crucible Rotation Technique (ACRT)" *Journal of Crystal Growth*, **203** (1999) pp 286-296.
- [21] R. U. Barz, P. Sabhapathy, M. Salcudean. "A Numerical Study of Convection during THM Growth of CdTe with ACRT" *Journal of Crystal Growth*, **180** (1997) pp 566-577.
- [22] C. W. Lan, D. T. Yang. "Dynamic Simulation of the Vertical Zone-Melting Crystal Growth" *International Journal of Heat and Mass Transfer*, **41** (1998) pp 4351-4373.
- [23] W. Seifert, P. Reinshaus, A. Bachran. "Thermosolutal Convection during Vertical Bridgman Growth of Semiconductor Melts" *Journal of Crystal Research and Technology*, **33** (1998) pp 899-910.
- [24] K. Lin, P. Dold, K. W. Benz. "Optimization of Thermal Conditions during Crystal Growth in a Multi-Zone Resistance Furnace" *Journal of Crystal Research and Technology*, **38** (2003) pp 419-428.

- [25] H. Weimann, J. Amon, Th. Jung, G. Muller. "Numerical Simulation of the Growth of 2" Diameter GaAs Crystals by the Vertical Gradient Freeze Technique" *Journal of Crystal Growth*, **180** (1997) pp 550-565.
- [26] Catherine Barat, Thierry Duffar, Jean-Paul Garandet. "Estimation of the Curvature of the Solid-Liquid Interface during Bridgman Crystal Growth" *Journal of Crystal Growth*, **194** (1998) pp 149-155.
- [27] Yongcai Liu, Sadik Dost, Brian Lent, Robert F. Redden. "A Three-Dimensional Numerical Simulation Model for the Growth of CdTe Single Crystals by the Traveling Heater Method Under Magnetic Field" *Journal of Crystal Growth*, **254** (2003) pp 285-297.
- [28] R. W. Olesinski, and G. J. Abbaschian, Bull. Alloy Phase Diagrams 5, **180** (1984).
- [29] S. Kuppurao, S. Brandon, J. Derby. "Modeling the Vertical Bridgman Growth of Cadmium Zinc Telluride I. Quasi Steady Analysis of Heat Transfer and Convection" *Journal of Crystal Growth*, **155** (1995) pp 93-102.
- [30] K. Edwards, S. Brandon, J. Derby. "Transient Effects during the Horizontal Bridgman Growth of Cadmium Zinc Telluride" *Journal of Crystal Growth*, **206** (1999) pp 37-50.
- [31] X. Ye, B. Tabarrok, D. Walsh. "Influence of Thermal Solutal Convection on CdTe Growth by the Traveling Heater Method" *Journal of Crystal Growth*, **169** (1996) pp 704-714.
- [32] M. C. Martinez-Tomas, V. Munoz-Sanjose, C. Reig. "A Numerical Study of Thermal Conditions in the THM Growth of HgTe" *Journal of Crystal Growth*, **243** (2002) pp 463-475.